Title	Theory of lattice relaxation in non-periodic moiré systems
Author(s)	中辻, 直斗
Citation	大阪大学, 2024, 博士論文
Version Type	VoR
URL	https://doi.org/10.18910/96385
rights	
Note	

Doctoral Thesis

Theory of lattice relaxation in non-periodic moiré systems

Department of Physics, Osaka University

Naoto Nakatsuji

2024

Table of Contents

Chapter 1

Introduction

1.1 Purpose of study

Moiré materials, created by stacking two-dimensional materials with lattice mismatch, have attracted attention as a platform of the novel physical phenomena. Twisted bilayer graphene (TBG), a fundamental example of moiré materials composed of two grahene layers [Fig. 1.1(a) and (b)], exhibits diverse physical phenomena that vary dramatically depending on the twisting angle. Particularly, at the magic angle ($\theta \sim 1.05°$), the emergent flat band [1] leads to various quantum phases including superconductivity, anomalous quantum Hall effect and correlated insulating phases [2, 3, 4, 5, 6, 7, 8, 9, 10, 11, 12, 13, 14, 15, 16, 17, 18, 19, 20]. In addition to TBG, moiré systems constructed from a range of two-dimensional materials — such as graphene, hexagonal boron nitride (hBN), and transition metal dichalcogenides (TMDs) — have been extensively studied and also remain subjects of ongoing investigation.

Research on moiré materials extends beyond bilayer systems to encompass multi-layer systems as well. Generally, twisted multilayer systems composed of more than two layers are characterized by multiple moiré patterns which generally mismatch with each other. As a consequence, the system exhibits a quasi-periodic nature which cannot be treated by the Bloch formalism. The twisted trilayer graphene (TTG) is a representative example of such a multilayer moiré system [21, 22, 23, 24, 25, 26]. A recent experimental study found superconductivity [27] in the quasi-periodic TTG.

Generally, twisted moiré systems are under a strong influence of lattice relax-

ation. In TBG, for instance, an in-plane lattice relaxation forms commensurate AB (Bernal)-stacking domains [28, 29, 30, 31, 32, 33, 34, 35, 36, 37, 38, 39, 40, 41, 42], and it significantly modifies the electronic band structure.[37, 38, 42]. Lattice relaxation occurs also in others moiré materials such as twisted TMDs [38] and graphene/hBN [43], and plays essential roles in the electronic properties. [35, 44, 45, 46] Previous theoretical studies concerning lattice relaxation effects have predominantly focused on moiré bilayer systems. However, the moiré trilayers and multilayers are unexplored in this regard, mainly due to the difficulty to treat the interference of multiple moiré patterns with vast length scale. In the first part of this thesis, we develop an effective continuum theory to analyze the lattice relaxation and its effect on twisted trilayer graphene with various rotation angle combinations. We will show that the relaxed lattice structure generally forms a patchwork of moiré domains where two moiré patterns are distorted to become locally commensurate, giving rise to topological electronic states.

In the second part of the thesis, we address another important question about non-periodic moiré pattern, which originates from random disorder. In most theoretical analyses on twisted 2D materials, the moiré pattern is usually supposed to be a perfectly regular and periodic. However, in the real sample, it is randomly distorted due to the lattice disorder giving rise to non-periodicity. Here we consider TBG with disordrered moiré pattern as the simplest example, and study the moiré disorder effect on the electronic structure.

The thesis is organized as follows. In the rest of this chapter, we will review the previous works on the moiré materials and and the lattice relaxation effects. Chapter 2 provides a theoretical basis to describe the electronic band structure and the lattice relaxation on TBG. In Chapter 3, we extend the theoretical methods to TTG, and study the lattice relaxation and its effect on the electronic properties. In Chapter 4, we study TBG with moiré disorder, and we show the effect on the flat band of magic-angle TBG. We conclude the thesis in Chapter 5.
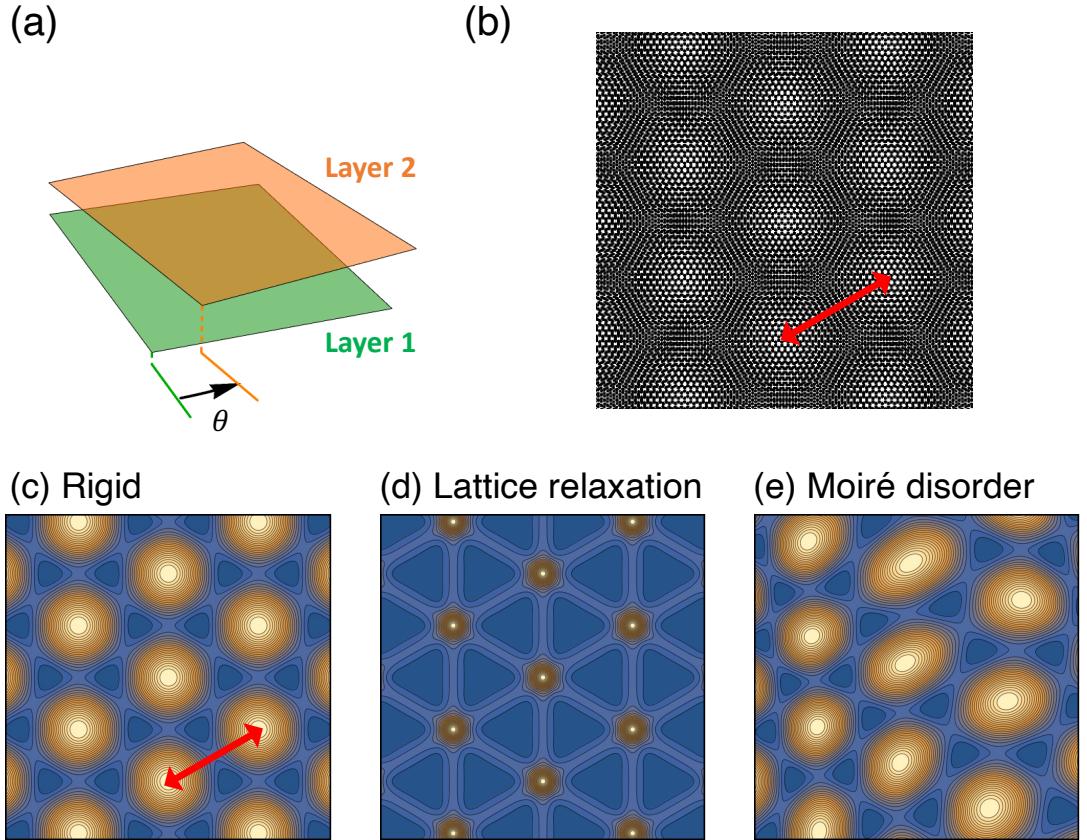
Figure 1.1: (a) The schematic figure of twisted bilayer graphene (TBG) with twist angle θ where Green and orange sheets represent the bottom and top graphene layer respectively. (b) The moiré pattern of TBG where black dots are the each carbon atoms, and red arrow indicates the moiré period. We can see the sparse and dense regions of atoms appear periodically. (c-e) The schematic figures of moiré pattern of TBG for (e) rigid, (d) with lattice relaxation and (e) with random moiré disorder. Here, yellow region represents the structure of the sparse region of atoms in (b), and blue region corresponds the dense region of atoms. In the case of (d) lattice relaxation, blue region is expanded while yellow region is shrink. On the other hand, in the case of (e) moiré disorder, we see that the moiré pattern is distorted non-periodically.

1.2 Moiré materials

Moiré materials, formed by the stacking of two-dimensional materials, have been the focus of extensive research in recent years. In these systems a long-range moiré pattern resulting from lattice mismatch profoundly influences their electronic properties. There are a wide variety of moiré materials arising from a choice of two-dimensional materials and twist angles. The previous studies have unveiled numerous remarkable phenomena that have never been observed in individual 2D materials. [3, 4, 11, 15, 18, 19, 20, 2, 3, 5, 6, 7, 8, 11, 14, 15, 16, 17, 18, 19, 20, 10, 12, 9, 13, 14]. In the following, we briefly introduce the representative graphene-based moiré systems, which are closely related to the topic of this thesis.

1.2.1 Twisted bilayer graphene

Twisted bilayer graphene (TBG), the simplest example of a moiré system, is created by stacking two monolayer graphene layers with relative twist angle [Fig. 1.1(a)]. The period of the moiré pattern increases as the twist angle decreases. The electronic properties of TBG dramatically depend on the twist angle. At a specific twist angle called the magic angle, it exhibits the generation of flat bands as a result of the moiré superlattice effect as shown in Fig. 1.2(a). Owing to the flat band, TBG shows a variety of correlated quantum phases like superconductivity[3, 4, 11, 15, 18, 19, 20], correlated insulator state[2, 3, 5, 6, 7, 8, 11, 14, 15, 16, 17, 18, 19, 20], strange metal[10, 12] and even ferromagnetic state[9, 13, 14]. Figure 1.2(b) shows the measurement of the resistance of the TBG with magic angle given by the experiment[3], where we see a superconductivity dome enclosed by white dash line in the phase space of electronic density and temperature.

The electronic structure of TBG can theoretically be computed using density functional theory [47, 48, 49, 50, 51] and tight binding model[52, 53, 48, 49, 51]. However, handling TBG with small twist angles ($\theta <\sim 1°$) using these atom-based
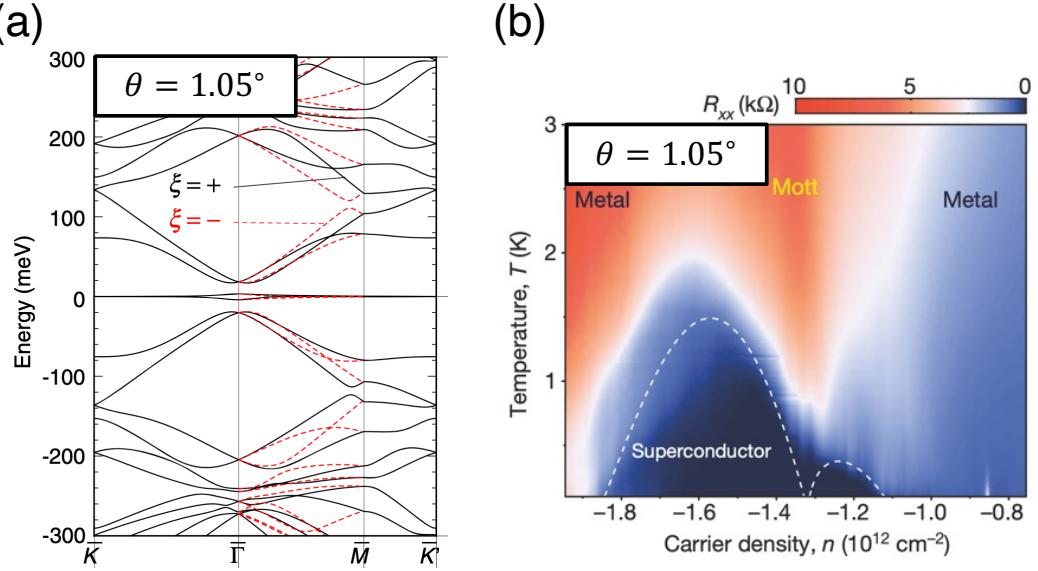
Figure 1.2: (a) The energy band structure of magic angle TBG calculated by [57]. We observe the flat band appears around zero energy. (b) The color map of the resistance R_{xx} masured with sweeping the temperature T and carrier density n. It shows Mott insulator phase around $n \simeq -1.3 \times 10^{12}$ cm^2, and Superconducting phase surrounded by white dashed line.

methods is challenging due to the vast number of atoms within the moiré unit cell. This complexity is significantly reduced by the continuum model [54, 55, 1, 56, 57, 42], which effectively averages the atomic degrees of freedom to capture the long-range moiré scale.

1.2.2 Twisted trilayer graphene

In addition to the extensive study of twisted bilayers in the past decade, the scope of investigation has extended to encompass multilayer systems including three or more layers. Particular attention has recently been directed towards twisted trilayer graphene (TTG), which consists of three graphene layers arranged in a specific rotational configuration [58, 59, 60, 61, 62, 63, 64, 65, 66, 67, 68, 69, 70, 71, 72, 73, 74, 21, 24, 22, 23, 75, 76, 77, 27, 78, 79, 80, 81]. The system is characterized by twist angles θ^{12} and θ^{23}, which represent the relative rotation of layer 2 to 1, and 3 to 2, respectively, as shown in Fig. 1.3(a).

The special case of $\theta^{12} = -\theta^{23}$ is called the mirror symmetric TTG [59, 60,

61, 62, 63, 64, 65, 66, 67, 68, 69, 72, 71, 73, 74, 70], where layer 1 and layer 3 are aligned precisely, leading to a single moiré periodicity [Fig. 1.3(b)]. The band structure of symmetric TTG has the Dirac band like monolayer graphene and moiré band like twisted bilayer graphene [60]. Recent transport measurements observed correlated insulator phases and superconductivity in mirror-symmetric TTGs [70, 71, 72, 73, 74].

Beyond the symmetric case, TTG offers a vast parameter space that remains largely unexplored. In general TTGs with $\theta^{12} \neq -\theta^{23}$, the system has two different moiré patterns originating from the interference of layer 1 and 2 and that of layer 2 and 3 [58, 24, 22, 23, 75, 76, 77, 27, 78, 79, 21, 80, 81, 82], as illustrated in Fig. 1.3(a). These two periodicities are generally incommensurate, giving rise to a quasi-crystalline nature in the system [83, 84, 27]. When the two moiré periods are close but slightly different, in particular, an interference of competing moiré structures generate a super-long range moiré-of-moiré pattern [21, 22, 23, 24]. Similar situation occurs also in composite multilayer systems consisting of graphene and hexagonal boron nitride [85, 86, 87, 88, 89, 90, 91, 92, 93, 94, 95, 96]. Previous researches investigated the electronic properties of general TTGs with various angle pairs by using several theoretical approaches [58, 79, 76, 77, 27, 23, 24, 78, 80, 81]. Recent experimental study also reported superconductivity in some asymmetric TTGs [27].

1.3   Lattice distortion in moiré materials

1.3.1   Lattice relaxation

Most of the theoretical research on the twisted moiré materials assume that the individual 2D layers are rigid, keeping the original lattice structures. In a real system, however, the lattice spontaneously distorts to the energetically stable structure . In the case of TBG, it has been demonstrated that the lattice relaxation leads to a creation of the locally commensurate domains with so-called AB

12

(a) General ($\theta^{12} \neq \theta^{23}$)

Layer 3

Layer 2

Layer 1

Layer 3

Layer 2

Layer 1

θ^{23}

θ^{12}

θ^{12} θ^{23}
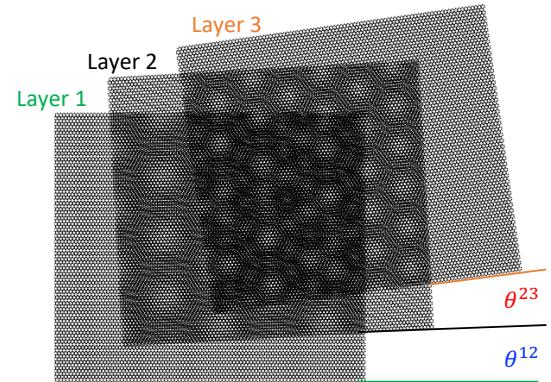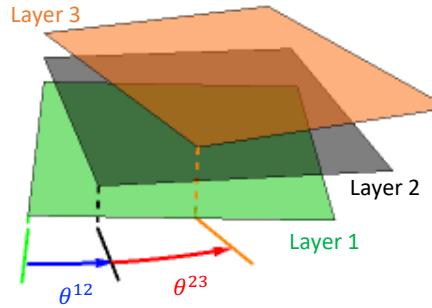
(b) Symmetric ($\theta^{12} = -\theta^{23}$)

$\theta^{12} = -\theta^{23}$
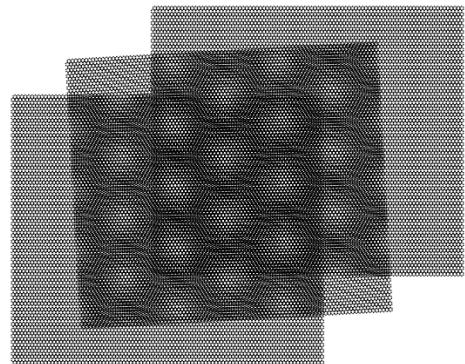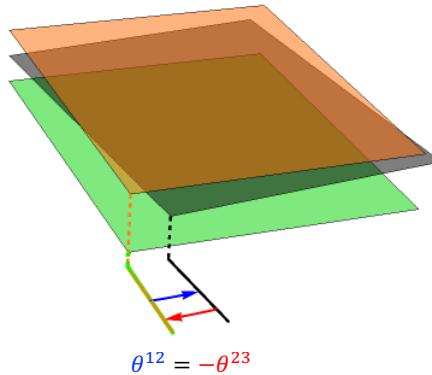
Figure 1.3: (a) The lattice structure of general twisted trilayer graphene (TTG). The left is the schematic figure of stacking structure of TTG where green, black and orange sheets indicate the monolayer graphene of layer 1, 2 and 3. In the right figure of the moiré pattern of TTG, we observe that the moiré 12 (between layer 1 and layer 2) and moiré 23 (between layer 2 and layer 3) have different pattern, and moiré-of-moiré pattern appears from the interference between moiré 12 and moiré 23. (b) The similar figure of (a) for mirror symmetric TTG.

and BA stacking [28, 32, 33, 34, 36, 37]. We will explain the detailed concept in the following. Figure 1.4 illustrates the lattice structure of TBG composed of rigid honeycomb lattices. We can see that the local structure at any particular position approximates a non-twist bilayer graphene configuration with a certain lateral shift, such as AA, AB and BA stacking as shown in the right. Here AA stack represents the structure that two honeycomb lattice completely overlap, and AB(BA) stack is the lattice structure where A(B) site of bottom layer and B(A) site of top layer vertically align. In non-rotated bilayer graphene, AB and BA stack (graphite structure) are the most energitically stable while AA is the most unstable [28, 97, 98]. In TBG, therefore, the graphene lattice simultaneously distorts to increase the AB/BA stacking[32, 33, 36, 34, 37].

Such a lattice relaxation of TBG has been theoretically studied by using DFT [32], molecular dynamics [33], various DFT-based effective methods [36, 34], and also by an effective continuum approach [37]. The coninuum model in Ref. [37] treats graphene layer as a continuum elastic membrane smearing carbon atoms. This approach significantly reduces the computational burden compared to earlier simulations that explicitly handled individual carbon atoms. The top row of Fig. 1.5 presents the lattice relaxation of TBG that calculated by Ref. [37]. Here the local stacking structure is depicted through the contour plot of the local stacking energy. We observe that the triangular domain structure of AB/BA stack becomes more remarkable for smaller twist angles.

The effect of the lattice relaxation is also investigated in other moiré bilayers. In graphene/hBN bilayer, for instance, the moiré pattern exhibits hexagonal domains [See Fig. 1.6(b)] unlike trigonal pattern in TBG. This occurs because in hBN, a boron and a nitrogen atom occupy A and B sublattices, respectively, giving different interlayer coupling energies in AB and BA stacking with graphene. The lattice relaxation expands only the most stable AB region, creating hexagonal domains. TMD moire systems can show both trigonal and hexagonal domains depending on the theirs stacking arrangements [Fig. 1.6(d) and (f)], parallel (P)
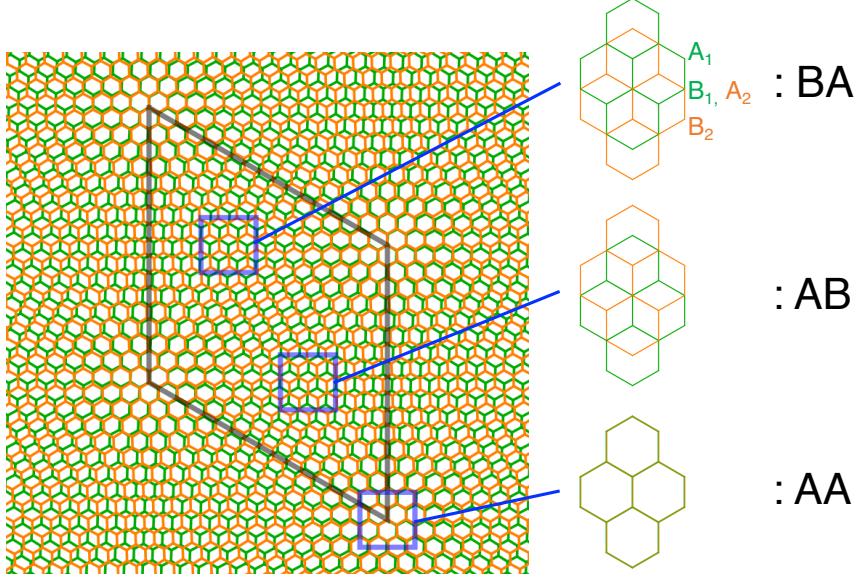
Figure 1.4: Lattice structure of TBG, where green and orange honeycomb represent the graphene lattice of bottom and top layer. Due to the lattice mismatch, local lattice structure of TBG varies between AA, AB and BA stacking illustrated in right column.

and anti-parallel (AP) stack. Here P stack illustrated on Fig. 1.6(c) constructed from the two monolayer TMD with relative twist near 0°, where while AP stack is given by the twist around 180° as shown in Fig. 1.6(e). In monolayer TMD, sublattice A and B are occupied by a metal atom and a chalcogen atom, respectively. In the P stack, AB and BA stack configurations give distinct structures and hence different interlayer coupling energies as in graphene/hBN, resulting in the hexagonal deomains. In the AP stack, on the other hand, AB and BA give identical structures related by the space inversion, leading to triangular domains as in TBG.
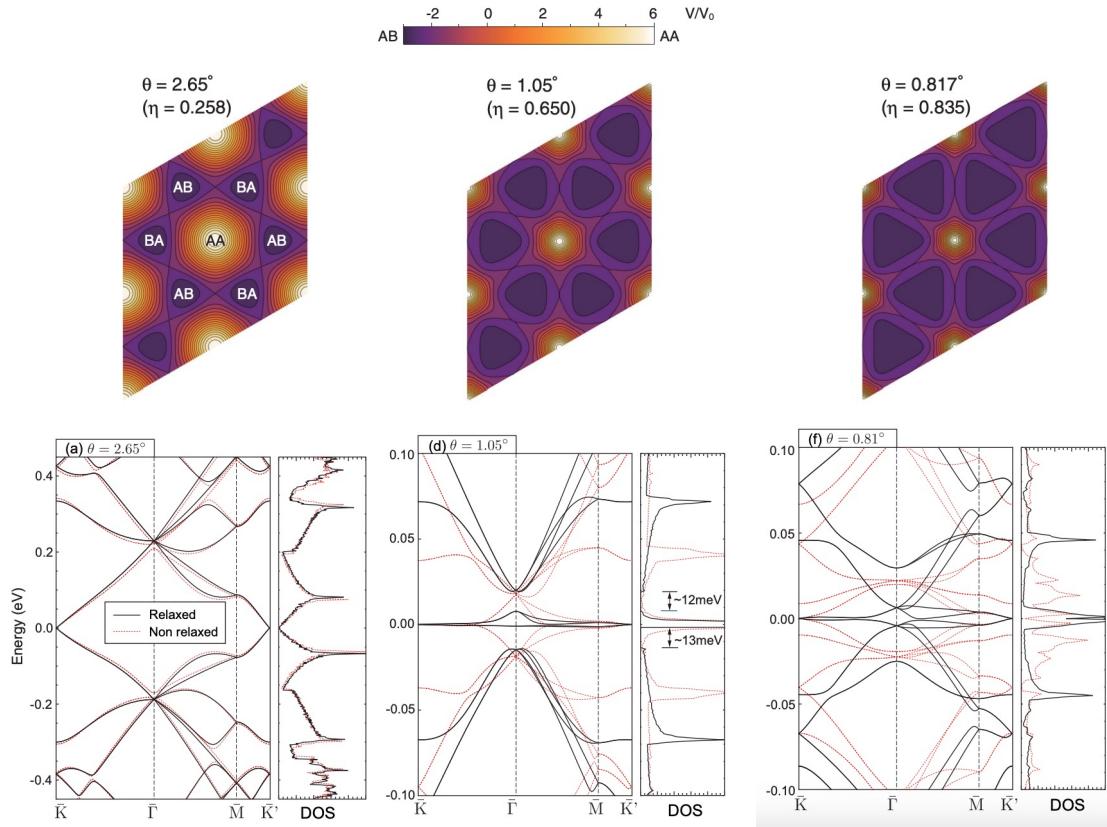
Figure 1.5: Moiré patterns (top) and energy band structures (bottom) with lattice relaxation at twist angle (left) $\theta = 2.65°$, (middle) $1.05°$ and (right) $0.817°$ given by [37]. In the top figure of moiré pattern, blight and dark regions are AA and AB/BA stacking respectively. We see that the AB/BA domain construction is dominant for the lower twist angle TBG. In bottom figures, black and red lines represent the energy band of relaxed and non-relaxed TBG.
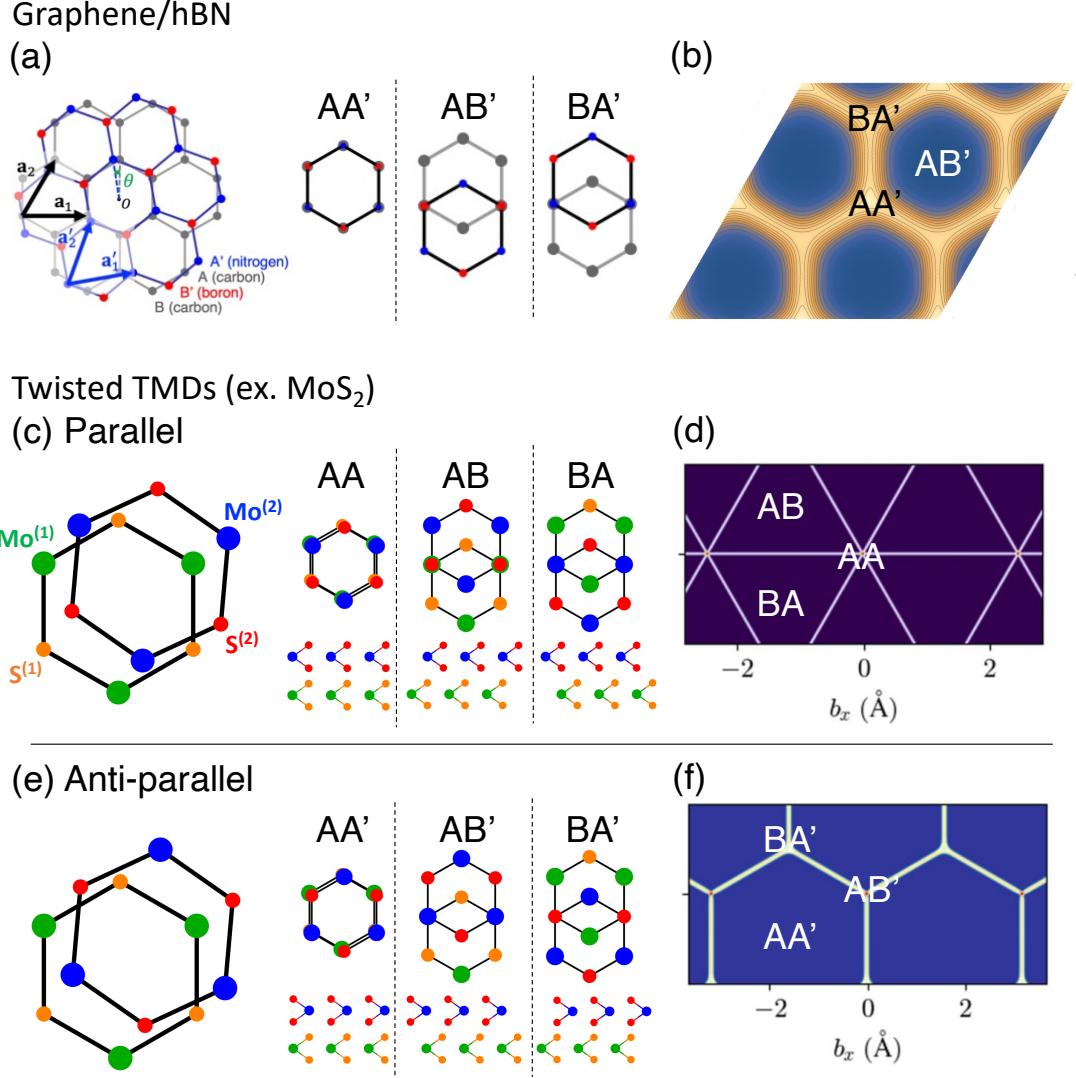
Figure 1.6: (a) Schematic figure of graphene/hBN. The local lattice structure of its moiré varies AA', AB' and BA' illustrated the right figures. (b) Relaxed moiré pattern of graphene/hBN (G/hBN) at $\theta = 0°$ given by [43]. (c,e) The schematic figures of twsited bilayer MoS2 for parallel and anti-parallel stack. The right figures show the local stacking structure in the theirs moiré, where top and bottom show the plane view and the cross-section of each stacking. (d,f) Relaxed moiré patterns of twisted TMDs (tTMDs) at $\theta = 0.1°$ for parallel and anti-parallel stack. These figures are calculated by [38].

1.3.2 Electronic structure under lattice relaxation

The lattice relaxation is also reflected in the electronic properties of moiré systems. The band structure of the relaxed TBG was theoretically studied in various methods [37, 39, 99, 57, 100]. The bottom row of Fig. 1.5 represents the band structure of TBG with various twist angles calculted in Ref. [37], where the black and red lines show the results for relaxed and non-relaxed TBG respectively. We see that the band structure is more strongly modulated by the relaxation in smaller twist angles. In the case of $\theta = 1.05°$, particularly, the energy gap arises between the central and the secondary bands, leaving the flat band isolated.

Recently the effect of the lattice relaxation in general moiré systems was integrated into the electronic continuum band model [101, 42, 102], enabling more efficient simulations with significantly reduced numerical costs compared to atomic models. In TBG, the effect of the lattice relaxation on the continuum band model manifests in two ways: firstly, the lattice strain within each layer induces an effective vector potential in the Dirac Hamiltonian of monolayer graphene [103, 104, 105], and secondly, the interlayer sliding singificantly modulates the moiré interlayer matrix elements [57, 100, 106, 102].

Similar lattice relaxation and the resulting band modulation are anticipated in multilayer moiré systems more than bilayer. However, to date, the study in this area remains largely unexplored. The primary challenge stems from the vast length scale of TTG, caused by the interference between two moiré patterns, resulting in a substantial number of atoms within the relevant scale. In this thesis, we solve this problem for the first time by extending the continuum model in Ref. [37] to multilayer moiré systems. We will show that the three-layer system exhibits a multi-scale lattice relaxation and moiré-of-moiré patchwork structure, which are never observed in bilayer systems. We also calculate the electronic structure of TTG incorporating the lattice relaxation. We will find that moiré-of-moiré patchwork structure gives rise to a network of one-dimensional topological electronic states localized on the boundary of domains.

1.3.3 Moiré disorder

In addition to the regular lattice relaxation within the moiré periodicity, real samples of moiré materials exhibit non-uniform lattice distortion, which includes local tensile and variance of the twist angle [6, 7, 8, 5, 107, 108, 109, 110, 111, 40, 112, 113, 114, 115, 116, 117, 118, 96, 119]. Figure 1.7(a) displays a moiré structure experimentally observed in a low-angle TBG sample [111], where blight spots indicate the AA stacking. We can see a non-uniform moiré pattern due to uniaxial stain in the sample. In other experiments, twist angle disorder which varying twist angle in real space, also observed [113][Fig. 1.7(b)]

The disorder within the moiré pattern is anticipated to significantly impact the electronic properties. Theoretically, calculating the electronic structure under such moiré disorder presents a challenge due to the necessity of considering numerous moiré periods, each involving a vast number of atoms, to comprehensively capture the entire disordered pattern. In previous works, the effect of the twist angle disorder in TBG was investigated using various theoretical approaches, such as a real-space domain model composed of regions with different twist angles [120], transmission calculations through one-dimensional variation of twist angle [121, 122, 123], and a Landau-Ginzburg theory to study the interplay between electron-electron interactions and disorder [124]. However, the influence of the long-range two-dimensional disorder as observed in real systems has not yet been investigated theoretically.

In this thesis we apply the effective continuum formulation in Ref. [42] to the TBG with moiré disorder. To simulate a non-periodic moiré disorder, we take a super unit cell composed of a number of moiré periods, and introduce the structural disorder within the period of the super cell. We will calculate the local density states, and discuss the fate of the flat band under the moiré disorder in detail.
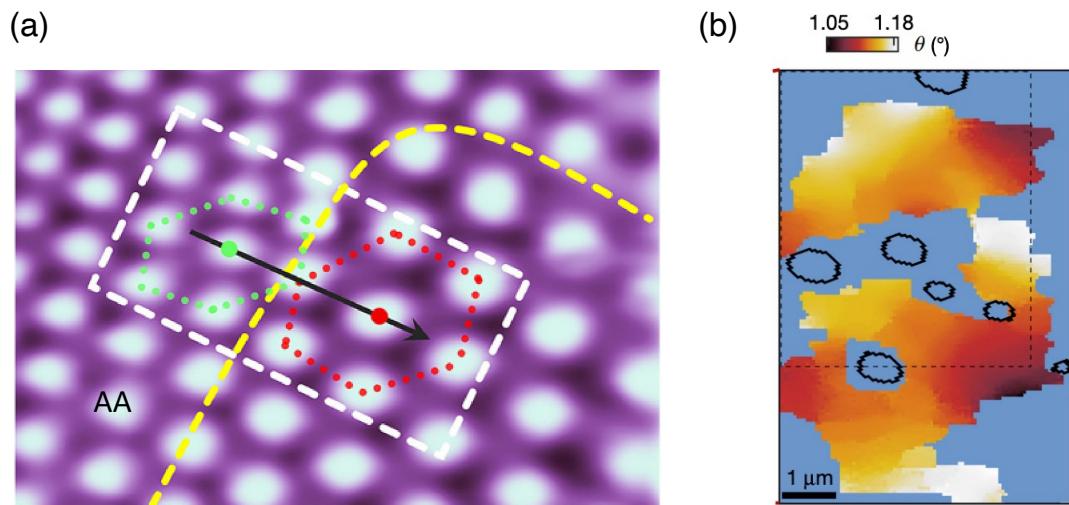
Figure 1.7: (a) Moiré pattern of the real sample of TBG observed by experiment[111], where blight spot represents AA stack. (b) Twist angle disorder in the sample of TBG obseved by experiment[113], where color plot represents the local twist angle.

Chapter 2

Theoretical background

Here, we introduce the basic theory for twisted bilayer graphene. We first explain the geometry of lattice structure of TBG. Second, we present a continuum method to treat the lattice relaxation by considering the total energy change in the presence of the distortion, By using the formula, we obtain the optimized atomic structure of TBG. In the third section, we introduce an electronic continuum band model of monolayer graphene and TBG. First, we introduce the Dirac Hamiltonian of monolayer graphnene. After that, we derive the continuum Hamiltonian for the intrinsic TBG with rigid honeycomb lattices, and then extend it to TBG with lattice distortion.

2.1 Geometry of moiré pattern of TBG

First, we define the geometry of monolayer graphene. We take the xy-plane parallel to graphene layer and the z axis as the perpendicular direction for graphene. In this thesis, we define the lattice vector of monolayer graphene without rotation as $\boldsymbol{a}_1 = a(1, 0)$ and $\boldsymbol{a}_2 = a(1/2, \sqrt{3}/2)$, where $a = 0.246$ nm is the lattice constant of monolayer graphene illustrated in Fig. 2.1(a). We also define the nearest-neighbor site vector as $\boldsymbol{\tau}_j = R\left(\frac{2\pi}{3}(j-1)\right)(a/\sqrt{3})(0, 1)$ for $j = 1, 2, 3$, where $R(\theta)$ is the rotation matrix. The reciprocal lattice vector is given by $\boldsymbol{b}_1 = (4\pi/\sqrt{3}a)(\sqrt{3}/2, -1/2)$ and $\boldsymbol{b}_2 = (4\pi/\sqrt{3}a)(0, 1)$. We define the $\boldsymbol{K}$ and $\boldsymbol{K}'$ valley, which are two independent corners of Brilluoin zone (BZ) of monolayer graphene, as

$$\boldsymbol{K} = -\frac{4\pi}{3a}(1, 0), \quad \boldsymbol{K}' = +\frac{4\pi}{3a}(1, 0), \tag{2.1}$$
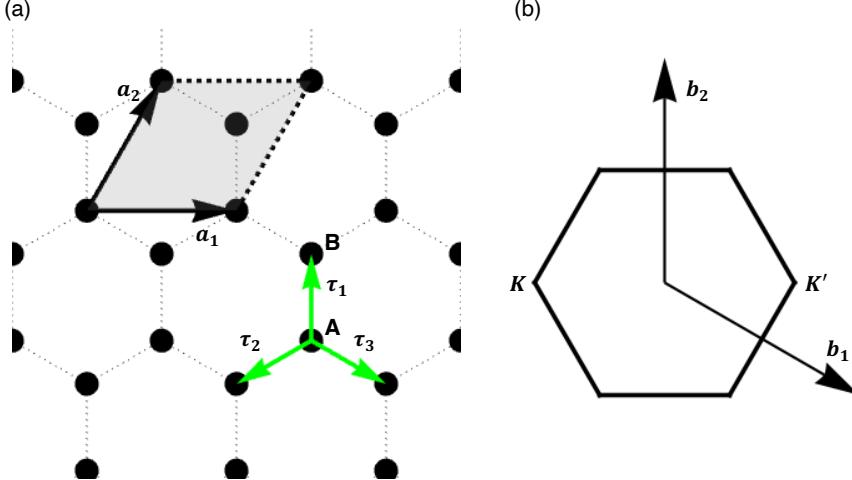
Figure 2.1: (a) Lattice structure of monolayer graphene. Black dots represent the carbon atoms and gray rhombus is the unit cell. Black and green arrows are the lattice vector $\boldsymbol{a}_j$ and the nearest-neighbor vectors $\boldsymbol{\tau}_j$ respectively. (b) Brillouin zone of monolayer graphene, where the arrows indicate the reciprocal lattice vector. we define two independent Dirac points as $\boldsymbol{K}$ and $\boldsymbol{K'}$ as illustrated in figure.

like in Fig. 2.1(b). As we show later, monolayer graphene has the linear band dispersion called the Dirac band around these corners.

From here on, we introduce the geometry of moiré structure [125]. We consider two monolayer graphenes stacked with relative twist angle θ. Here we assume that layer 1 and layer 2 are rotated $\mp\theta/2$, respectively, so the lattice vector of layer $l(=1,2)$ are given by $\boldsymbol{a}_j^{(l)} = R(\mp\theta/2)\boldsymbol{a}_j$ where $\mp$ is for $l = 1$ and 2, respectively. Likewise, the reciprocal lattice vectors of layer l are $\boldsymbol{b}_j^{(l)} = R(\mp\theta/2)\boldsymbol{b}_j$.

The atomic structure of TBG is not exactly periodic in general because the periodicities of the two layers are generally incommensruate. However, in some special twist angles, the atomic lattices of the two layers happen to commensurate, and the entire system becomes periodic. This is called a commensurate TBG. In such a case, we can express the period $\boldsymbol{L}^{(\mathrm{atom})}$ in terms of integers n, m, n' and m' as

$$\boldsymbol{L}^{(\mathrm{atom})} = n\boldsymbol{a}_1^{(1)} + m\boldsymbol{a}_2^{(1)} = n'\boldsymbol{a}_1^{(2)} + m'\boldsymbol{a}_2^{(2)}. \tag{2.2}$$

In TBG, we can write $n' = m$ and $m' = n$ in a proper choice of the lattice vectors

$a_i^{(1)}$ and $a_i^{(2)}$. Thus Eq. (2.2) become as

$$L^{(\text{atom})} = na_1^{(1)} + ma_2^{(1)} = ma_1^{(2)} + na_2^{(2)}. \qquad (2.3)$$

By solving this equation, the twist angle θ (i.e. the angle between $a_i^{(1)}$ and $a_i^{(2)}$) can be obtained as a function of m and n as,

$$\theta(n, m) = \cos^{-1}\left[\frac{1}{2}\frac{m^2 + n^2 + 4mn}{m^2 + n^2 + mn}\right]. \qquad (2.4)$$

The $60°$ rotation of $L^{(\text{atom})}$ also gives a lattice vector because of C_{6z} rotational symmetry. Fig. 2.2(a) and (c) show the commensurate lattice structure of TBG for $\theta = 13.2°$ and $7.34°$, where green and orange dots are the carbon atoms of bottom and top layer respectively, and black rhombus is the commensurate moiré unit cell. (b) and (d) of Fig. 2.2 show first BZ of bottom (green dotted) and top (orange) layer in the k-space. Gray honeycomb is the moiré BZ, and we labeled the high symmetry points in BZ as Γ, $\bar{M}$, $\bar{K}$ and $\bar{K}$ illustrated in right figure of (b).

When twist angle is small enough ($\theta \lesssim 10°$), the mismatch of the lattice periods of the rotated layers gives rise to a long-period moiré pattern. In this low-angle regime, the spatial period of the moiré pattern serves as an effective period and the electronic properties can be treated by a usual Bloch system, even when the system is not exactly periodic in the atomic scale. The moiré super period is estimated as follows. We take the origin as the rotation center, then we can define the interlayer atomic shift $\delta_0(r)$ as the difference of the two atoms after the rotation,

$$\delta_0(r) = [R(-\theta/2) - R(+\theta/2)]\, r. \qquad (2.5)$$

When the interlayer atomic shift $\delta_0(L_i)$ at $r = L_i$ coincides with a lattice vector of monolayer graphene without rotation a_i ($i = 1, 2$), the system has the moiré

23

period of L_i. Here, we assume that the condition $\delta_0(L_i) = a_i$, it lead to,

$$L_i = [R(-\theta/2) - R(+\theta/2)]^{-1} a_i = L \times R(-\pi/2)a_i \qquad (2.6)$$

for $i = 1, 2$, where L is the lattice constant of the moiré pattern written by

$$L = \frac{a}{2\sin(\theta/2)}. \qquad (2.7)$$

The reciprocal lattice vectors of moiré lattice satisfying $G_i \cdot L_j = 2\pi\delta_{ij}$, are given as

$$G_i = [R(-\theta/2) - R(+\theta/2)]\, b = b_i^{(1)} - b_i^{(2)}. \qquad (2.8)$$

For a commensurate TBG, the exact period $L^{(\mathrm{atom})}$ in Eq. (2.2) and the moiré period L in Eq. (2.7) are simply related by $L^{(\mathrm{atom})} = |m - n|L$. Figure 2.3 shows the moiré lattice structure of TBGs with $\theta = 13.2°$, $11.0°$ and $9.43°$. Here green and orange dots represent the carbon atoms of bottom and top layer, and red and blue rhombuses indicate the incommensurate and commensurate moiré unit cell.

2.2 Continuum method for lattice relaxation

In this section, we introduce a continuum method to obtain the stable lattice structure of TBG allowing the lattice distortion [37]. We express the total energy as a functional of the position-dependent displacement vector, which expresses the atomic shift at the position r. We then derive the Euler-Lagrange equation to minimize the total energy. Here, we assume that the distortion of X (=A or B) atom in layer l is the continuum function $s_X^{(l)}$ as the real space r, and ignore the dependence of the sublattice $s_A^{(l)} = s_B^{(l)} = s^{(l)}$.

First, we express the total energy of TBG as the summation of the binding energy (inter-layer term) and the elastic energy (intra-layer term). The local
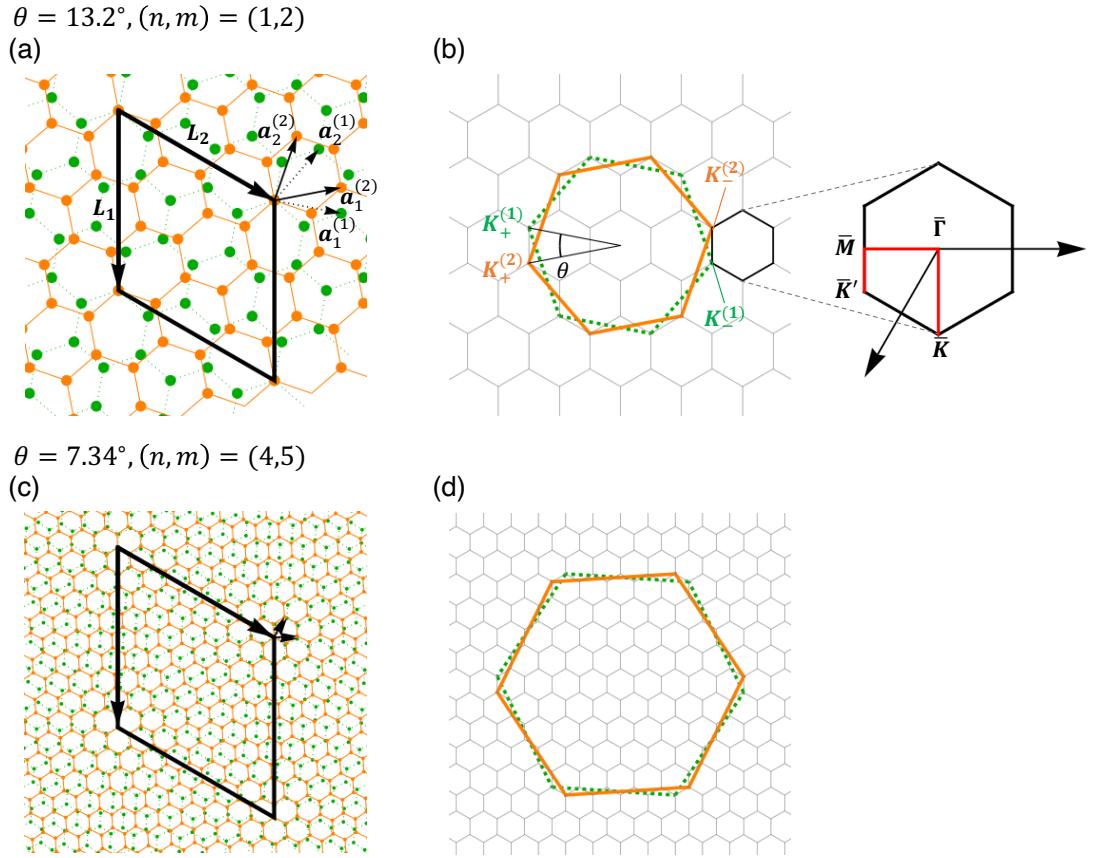
Figure 2.2: (a) Lattice structure of TBG at $\theta = 13.2°$, $(n, m) = (1, 2)$, where green and orange dots represent the carbon atoms, and black rhombus is the moiré unit cell. (b) The schematic figure of k-space of TBG with same angle of (a), where green and orange hexagon is the BZ of monolayer graphene for layer 1 and 2 respectively. Small gray hexagon are the moiré BZ, and we label the symmetric point as Γ, $\bar{M}$, $\bar{K}$ and $\bar{K}'$ as shown right figure of (b). (c-d) The similar figure of (a) and (b) for TBG at $\theta = 7.34°$, $(n, m) = (4, 5)$.
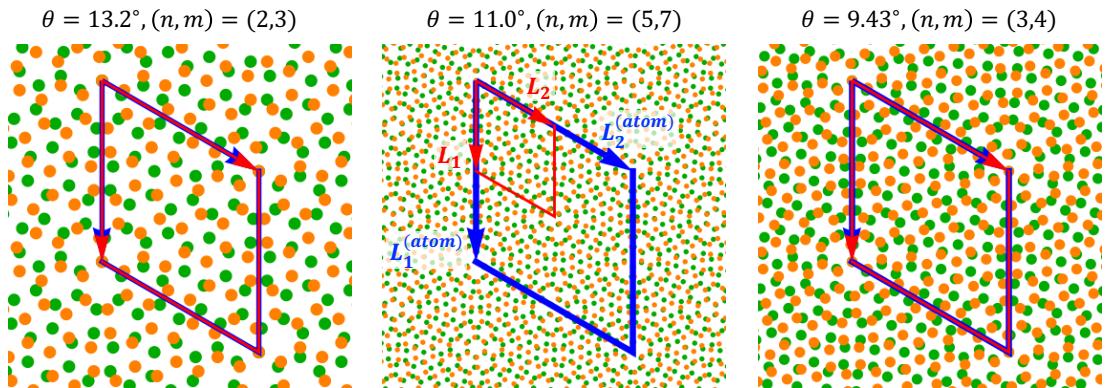
Figure 2.3: Lattice structure of TBG at (left) $\theta = 13.2°$, (middle) $11.0°$ and (right) $9.43°$, where green and orange dots represent the carbon atoms, and red and blue rhombus indicate the incommensurate and commensurate moiré unit cell[125].

atomic shift between the both layer at r is given by

$$\delta(r) = \delta_0(r) + s^{(2)}(r) - s^{(1)}(r). \tag{2.9}$$

Here $\delta_0(r)$ is the interlayer atomic shift without lattice deformation which is given as Eq. (2.5). When the moiré period L is much larger than the lattice constant of graphene a, the local stacking structure can be regarded similar to the nonrotated bilayer graphene with the relative shift by δ depending on the position smoothly. We define the nonrotated bilayer graphene's interlayer local binding energy per area as $V[\delta]$. In the simplest approximation, it can be expressed as a cosine function as

$$V[\delta] = \sum_{j=1}^{3} 2V_0 \cos\left[b_j \cdot \delta\right], \tag{2.10}$$

where $b_3 = -b_1 - b_2$. In TBG, δ is not constant but it smoothly varying as a function of the position r. Then the total interlayer binding energy of TBG U_B is written as

$$
\begin{aligned}
U_B &= \int \mathrm{d}^2 r V[\delta(r)] \\
&= \int \mathrm{d}^2 r \sum_{j=1}^{3} 2V_0 \cos\left[G_j \cdot r + b_j \cdot (s^{(2)} - s^{(1)})\right],
\end{aligned}
\tag{2.11}
$$

where $G_3 = -G_1 - G_2$, and we used Eq. (2.9), (2.10) and the relation $b_j \cdot \delta_0 = G_j \cdot r$.

The elastic energy of TBG is written in a standard form [103, 126] as

$$U_E = \sum_{l=1}^{2} \frac{1}{2} \int \left[(\mu + \lambda)\left(s_{xx}^{(l)} + s_{yy}^{(l)}\right)^2 + \mu\left\{\left(s_{xx}^{(l)} - s_{yy}^{(l)}\right)^2 + 4\left(s_{xy}^{(l)}\right)^2\right\}\right] \mathrm{d}^2 r, \tag{2.12}$$

where $\lambda = 3.25$ eV$/\mathring{A}^2$ and $\mu = 9.57$ eV$/\mathring{A}^2$ are graphene's Lamé factors[127, 35], and $s_{ij}^{(l)} = (\partial_i s_j^{(l)} + \partial_j s_i^{(l)})/2$ is the strain tensor. The relaxed lattice structure can be obtained by minimizing the total energy $U = U_E + U_B$ as a function of $s^{(l)}$ ($l = 1, 2$). We introduce $s^{\pm} = s^{(2)} \pm s^{(1)}$ and rewirite U as a function of $s^{\pm}$. To obtain the relaxed lattice structure, we solve the Eular-Lagrange equations for $s^{\pm}$

as

$$\frac{\mathrm{d}}{\mathrm{d}t}\left(\frac{\partial U}{\partial \dot{s}_\mu^\pm}\right) = \frac{\partial U}{\partial s_\mu^\pm}, \tag{2.13}$$

where $\mu = x, y$ and $l = 1, 2$. The left-hand side is 0 because U does not depend on the $\dot{s}^\pm$ and t. Since the binding energy U_B is the function only for s^- not s^+, the equation that come from $s_{\mu=x,y}^+$ terms gives $s^+ = 0$. While the equation of s_μ^- terms are given as

$$\frac{1}{2}(\lambda + \mu)\left(\frac{\partial^2 s_x^-}{\partial x^2} + \frac{\partial^2 s_y^-}{\partial xy}\right) + \frac{1}{2}\mu\left(\frac{\partial^2 s_x^-}{\partial x^2} + \frac{\partial^2 s_x^-}{\partial y^2}\right)$$
$$+ \sum_{j=1}^{3} 2V_0 \sin\left[\boldsymbol{G}_j \cdot \boldsymbol{r} + \boldsymbol{b}_j \cdot \boldsymbol{s}^-(\boldsymbol{r})\right] b_{j,x} = 0 \tag{2.14}$$

$$\frac{1}{2}(\lambda + \mu)\left(\frac{\partial^2 s_y^-}{\partial y^2} + \frac{\partial^2 s_x^-}{\partial xy}\right) + \frac{1}{2}\mu\left(\frac{\partial^2 s_y^-}{\partial x^2} + \frac{\partial^2 s_y^-}{\partial y^2}\right)$$
$$+ \sum_{j=1}^{3} 2V_0 \sin\left[\boldsymbol{G}_j \cdot \boldsymbol{r} + \boldsymbol{b}_j \cdot \boldsymbol{s}^-(\boldsymbol{r})\right] b_{j,y} = 0 \tag{2.15}$$

where $b_{j,\mu}$ is $\mu(= x, y)$ component of $\boldsymbol{b}_j$, and we used following relations,

$$\frac{\partial U_B}{\partial s_\mu^-} = -\int \mathrm{d}^2\boldsymbol{r} \sum_{j=1}^{3} 2V_0 \sin\left[\boldsymbol{G}_j \cdot \boldsymbol{r} + \boldsymbol{b}_j \cdot \boldsymbol{s}^-(\boldsymbol{r})\right] b_{j,\mu}, \tag{2.16}$$

and

$$\frac{\partial U_E}{\partial s_\mu^{(l)}} = -\frac{1}{2}\int \mathrm{d}^2\boldsymbol{r}\left[(\mu + \lambda)\,\partial_\mu\left(s_{xx}^{(l)} + s_{yy}^{(l)}\right)\right.$$
$$\left. + \mu\left\{\pm\partial_\mu\left(s_{xx}^{(l)} - s_{yy}^{(l)}\right) + \partial_{\bar{\mu}}\left(s_x^{(l)} + s_y^{(l)}\right)\right\}\right]. \tag{2.17}$$

Here, we rewrite the elastic potential term by using the integration by parts. The integrated term of the integration by part is 0 because the displacement vector $s_\mu^{(l)}$ is a periodic function for the moiré period. Then the elastic potential term is

written as

$$U_E = -\frac{1}{2} \sum_{l=1}^{2} \int d^2 r \left[(\mu + \lambda) \left(s_x^{(l)} \partial_x + s_y^{(l)} \partial_y \right) \left(s_{xx}^{(l)} + s_{yy}^{(l)} \right) \right.$$

$$\left. + \mu \left\{ \left(s_x^{(l)} \partial_x - s_y^{(l)} \partial_y \right) \left(s_{xx}^{(l)} - s_{yy}^{(l)} \right) + \left(s_x^{(l)} \partial_y + s_y^{(l)} \partial_x \right) \left(s_x^{(l)} + s_y^{(l)} \right) \right\} \right]. \tag{2.18}$$

We define the Fourier components s_q^- and $f_q^j (j = 1, 2, 3)$ as

$$s^-(r) = \sum_q s_q^- e^{iq \cdot r} \tag{2.19}$$

$$\sin \left[G_j \cdot r + b_j \cdot s^- \right] = \sum_q f_q^j e^{iq \cdot r} \tag{2.20}$$

where $q = m_1 G_1 + m_2 G_2$ are vectors of the reciprocal lattice. In the Fourier form, Eq. (2.14) are written as

$$s_q = \sum_{j=1}^{3} 4V_0 f_q^j \hat{K}_q^{-1} b_j, \tag{2.21}$$

where

$$\hat{K}_q = \begin{pmatrix} (\lambda + 2\mu)q_x^2 + \mu q_y^2 & (\lambda + \mu)q_x q_y \\ (\lambda + \mu)q_x q_y & \mu q_x^2 + (\lambda + 2\mu)q_y^2 \end{pmatrix}. \tag{2.22}$$

Equations (2.19), (2.20) and (2.21) are self-consistent equation. To obtain the optimized lattice structure, we solve this self-consistent equation with the Fourier component of the displacement vector s_q as the variable.

Figure 2.4 shows (a) binding energy of TBG with (left) $\theta = 2.65$, (middle) $1.05°$ and (right) $0.547°$, where yellow region corresponds to the AA stack while blue region corresponds to the AB/BA stack. We can see that the lattice relaxation constructs the AB/BA domains and it's remarkable for smaller angle. Fig. 2.4(b) represents the displacement vector $s^-(r)$ for same angles of (a), where the color plot corresponds to the norm of displacement vector $|s^-|$ and the arrows indicate the direction of s^- at each position.
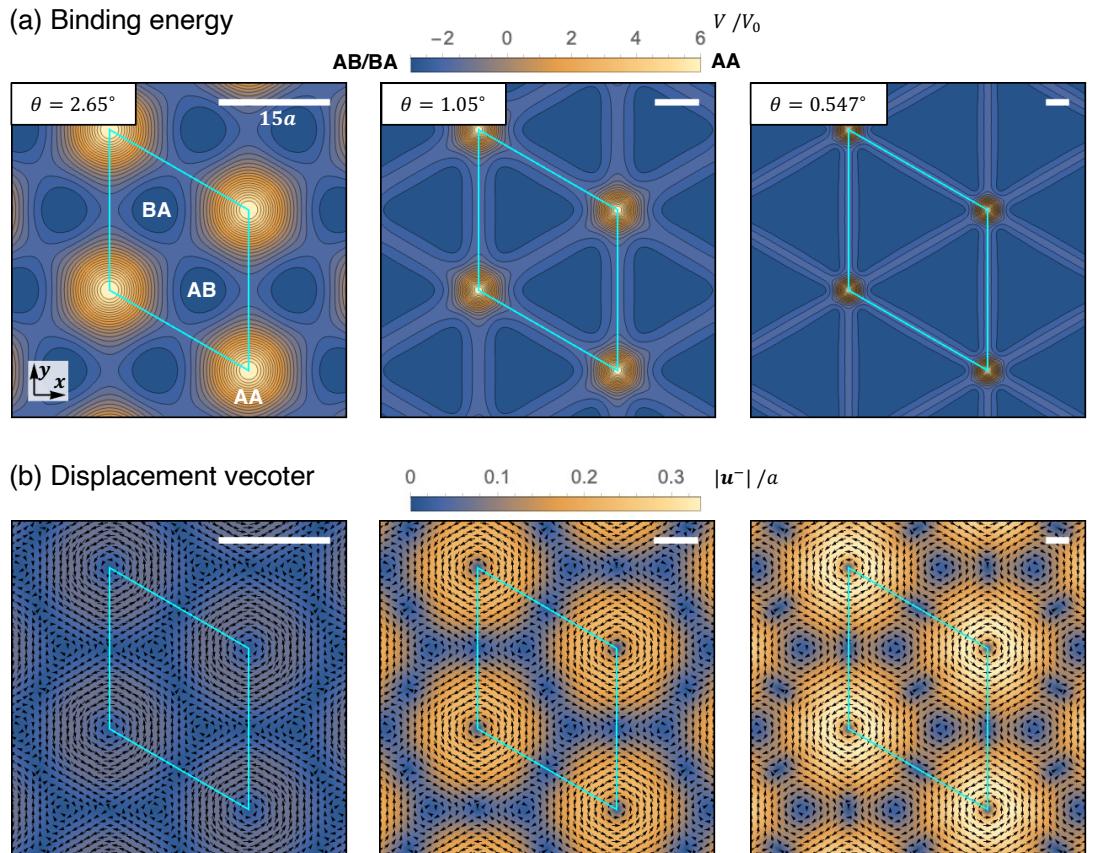
Figure 2.4: (a) The color plot of binding energy of TBG at $\theta = 2.65°$, (midlle) 1.05° and (right) 0.547°, where yellow and blue regions correspond to AA and AB/BA stack. (b) The plot of the displacement vector of TBG with same angle for (a). Here color plot represents the norm of the displacement vector and arrows show the direction of such vectors at each position. Blue rhombus is the moiré unit cell in all figures.

2.3 Continuum Hamiltonian for the electronic band

In this section, we introduce the effective continuum Hamiltonian for electrons in monolayer graphenes and TBGs for both cases with and without lattice relaxation. We derive them from the tight binding model with the Slater-Koster formula[128]. In this thesis, we use the Slater-Koster formula

$$-T(\boldsymbol{r}) = V_{pp\pi} \left[1 - \left(\frac{\boldsymbol{r} \cdot \boldsymbol{e}_z}{|\boldsymbol{r}|} \right)^2 \right] + V_{pp\sigma} \left(\frac{\boldsymbol{r} \cdot \boldsymbol{e}_z}{|\boldsymbol{r}|} \right)^2, \tag{2.23}$$

$$V_{pp\pi} = V_{pp\pi}^0 \exp\left(-\frac{|\boldsymbol{r}| - a_0}{\delta_0} \right), \quad V_{pp\sigma} = V_{pp\sigma}^0 \exp\left(-\frac{|\boldsymbol{r}| - d}{\delta_0} \right) \tag{2.24}$$

as the hooping function $T(\boldsymbol{r})$ for intra and inter layer hooping. we assume the hooping depends on only the distance $|\boldsymbol{r}|$. $a_0 = a/\sqrt{3}$ is the distance of nearest neigboher atoms and $d = 0.335$ nm is the distance between two layer. $V_{pp\pi} = -2.7$ eV is the hooping integral between nearest neighbor atoms of monolayer graphene and $V_{pp\sigma} = 0.48$ meV is the hooping integral between two layer atoms when these are vertically aligned. δ_0 represents the decay length of the hooping integral. Here we take $\delta_0 = 0.184a$ as that the next nearest neighbor hooping are $0.1V_{pp\pi}$.

2.3.1 Monolayer graphene

Here, we introduce the Hamiltonian of monolayer graphene H_G without rotation. The electronic state around Fermi energy for monolayer graphene is mainly occupied by the p_z orbit of carbons. The tight binding model constructed by the p_z orbits is a good approximation. We define $\langle \boldsymbol{r} | | \boldsymbol{R}_X \rangle \equiv \phi_X(\boldsymbol{r} - \boldsymbol{R}_{X,i})$ as the atomic state of the sublattice X at $\boldsymbol{R}_X$. By using Eq. (2.23) as the hooping integral, tight binding Hamiltonian of monolayer graphene is given by

$$H = -\sum_{X,X'} T\left(\boldsymbol{R}_{X'} - \boldsymbol{R}_X\right) |\boldsymbol{R}_X\rangle \langle \boldsymbol{R}_{X'}| + h.c.. \tag{2.25}$$

We define the Blach basis of the wave function of the p_z orbit for each sublattice $X = A, B$ as

$$\Phi_X(\boldsymbol{k}, \boldsymbol{r}) = \frac{1}{\sqrt{N}} \sum_{i=1}^{N} e^{i\boldsymbol{k}\cdot\boldsymbol{R}_{X,i}} \phi_X(\boldsymbol{r} - \boldsymbol{R}_{X,i}). \tag{2.26}$$

N is the number of the unit cell in the system and i is the index of the unit cell. $\boldsymbol{R}_{X,i}$ is the position of sublattice X in the ith unit cell which is given as

$$\boldsymbol{R}_{X,i} = n_i \boldsymbol{a}_1 + m_i \boldsymbol{a}_2 + \boldsymbol{\tau}_X, \tag{2.27}$$

where n_i, m_i are the integers, and $\boldsymbol{\tau}_A = \boldsymbol{0}, \boldsymbol{\tau}_B = \boldsymbol{\tau}_1$. The wave function of the electron is expressed as the linear combination of the above Bloch basis,

$$\Psi_j(\boldsymbol{k}, \boldsymbol{r}) = \sum_X \phi_{j,X} \Psi_X(\boldsymbol{k}, \boldsymbol{r}). \tag{2.28}$$

The coefficient $\psi_{j,X}$ satisfies the relation $\sum_X \psi_{j,X}^* \psi_{j,X} = 1$ and j is the index for the eigenenergy. Using this wave function, the Hamiltonian is expanded as

$$H\psi_j = E_j S \psi_j \simeq E_j \psi_j, \tag{2.29}$$

where we define that $E_j = \langle \psi_j | H | \psi_j \rangle$ and $\psi_j^T = (\psi_{j,A}, \psi_{j,B})$. H and S are the 2×2 matrix defined as follows,

$$H_{X'X} = \langle \Phi_{X'} | \mathcal{H} | \Phi_X \rangle, \quad S_{X'X} = \langle \Phi_{X'} | | \Phi_X \rangle. \tag{2.30}$$

Here we used the fact that the S matrix becomes the identify matrix I_2 around low energy region. We only consider the on-site energy and the nearest-neighbor hooping and we assume that all unit cell gives similar contribution, each matrix

element of Hamiltonian are written as follows,

$$H_{XX} = \frac{1}{N} \sum_{i=1}^{N} \langle \boldsymbol{R}_{X,i} | \mathcal{H} | \boldsymbol{R}_{X,i} \rangle = \epsilon_X \tag{2.31}$$

$$H_{AB} = \frac{1}{N} \sum_{i=1}^{N} \sum_{l=1}^{3} e^{i\boldsymbol{k}\cdot\boldsymbol{\tau}_l} \langle \boldsymbol{R}_{A,i} | \mathcal{H} | \boldsymbol{R}_{A,i} - \boldsymbol{\tau}_l \rangle = \gamma_0 f(\boldsymbol{k}), \tag{2.32}$$

where we define the nearest-neighbor hooping integral γ_0 as

$$\gamma_0 \equiv \langle \boldsymbol{R}_{A,i} | \mathcal{H} | \boldsymbol{R}_{A,i} - \boldsymbol{\tau}_l \rangle = T(|\boldsymbol{\tau}_j|). \tag{2.33}$$

We define the phase part of Hamiltonian as

$$f(\boldsymbol{k}) \equiv \sum_{j=1}^{3} e^{i\boldsymbol{k}\cdot\boldsymbol{\tau}_j}. \tag{2.34}$$

The matrix element H_{BA} is given by replacing $f_{\boldsymbol{k}}$ to $f_{\boldsymbol{k}}^*$ because the difference between B atom to A atom are $-\boldsymbol{\tau}_j$ ($j = 1, 2, 3$). Both sublattice A and B are carbon atoms, which are equivalent when the lattice is rigid. This is understood from the C_{2z} symmetry of monolayer Graphene. In short, we can take the origin of the energy axis satisfied $\epsilon_A = \epsilon_B = 0$ because these on-site terms give the energy constant for both basis. Finally, the Hamiltonian as the matrix form is written as follows,

$$H_G = \begin{pmatrix} 0 & \gamma_0 f_{\boldsymbol{k}} \\ \gamma_0 f_{\boldsymbol{k}}^* & 0 \end{pmatrix}. \tag{2.35}$$

To take the local energy band structure near $\boldsymbol{K}_\xi (= \boldsymbol{K}_+ = \boldsymbol{K}, \boldsymbol{K}_- = \boldsymbol{K}')$, we expand this hamiltonian around $\boldsymbol{K}_\xi$. Since in the expansion to the 1st order of $|\boldsymbol{k}|$, $f_{\boldsymbol{k}}$ is written

$$f_{\boldsymbol{k}} \simeq -\sqrt{3}a(\xi k_x - ik_y)/2, \tag{2.36}$$

32

the effective Hamiltonian of monolayer graphene is expressed as

$$H_{G,\xi} = -\hbar v_F \boldsymbol{k} \cdot \boldsymbol{\sigma} \tag{2.37}$$

for the K_ξ-valley. Here $v = \sqrt{3}a\gamma_0/2$ is the Dirac velocity, and $\boldsymbol{\sigma} = (\xi\sigma_x, \sigma_y)$ is the Pauli matrix. We note that the minus sign in the front of $\hbar v$ is came from the sign of $V_{pp\sigma}$ and $V_{pp\pi}$ in the Slater-Koster formula Eq. (2.23) we used in this thesis. The eigenvalues of the Hamiltonian are given as

$$E_\pm = \pm\hbar v_F |\boldsymbol{k}|. \tag{2.38}$$

It shows that the monolayer graphene has the liner Dirac dispersion around K_ξ-valley.

Strained lattice

We introduce the effective Hamiltonian of strained monolayer graphene by following the paper[103]. After the strain, the position $\tilde{\boldsymbol{R}}_{X,i}$ of the atom originally at $\boldsymbol{R}_{X,i}$ moves to

$$\tilde{\boldsymbol{R}}_{X,i} = \boldsymbol{R}_{X,i} + \boldsymbol{s}(\boldsymbol{R}_{X,i}), \tag{2.39}$$

where we define the displacement vector $\boldsymbol{s}(\boldsymbol{R}_{X,i})$ that gives the shift of atom at $\boldsymbol{R}_{X,i}$ by the strain. On the strained lattice, the vector between the nearest neighbor atoms is modified as

$$\boldsymbol{\tau}_j \rightarrow \tilde{\boldsymbol{\tau}}_j \tag{2.40}$$

$$= \boldsymbol{\tau}_j + \delta s_{i,j} \tag{2.41}$$

$$\simeq [I_2 + \mathcal{E}]\, \boldsymbol{\tau}_j, \tag{2.42}$$

where

$$\mathcal{E} = \begin{pmatrix} \partial_x s_x & \partial_x s_y \\ \partial_y s_x & \partial_y s_y \end{pmatrix}, \tag{2.43}$$

33

and $\delta s_{i,j} \equiv s(R_{A,i} + \tau_j) - s(R_{A,i})$ Here We assume that the strain varies smoothly for the atomic scale, in short, we only take liner order of $\partial_\mu s_\nu$. By this chance of the distance, the hooping parameter and the phase of Hamiltonian 2.35 is also modulated as follows,

$$f_k \rightarrow \tilde{f}_k = \sum_{j=1}^{3} e^{i k \cdot \tilde{\tau}_j}, \tag{2.44}$$

$$\gamma_0 \rightarrow \tilde{\gamma}_0 = T(|\tilde{\tau}|). \tag{2.45}$$

Since $|\tau_j + \delta s_{i,j}| = |\tau_j| + \frac{\tau_j \cdot \delta s_{i,j}}{|\tau_j|} + O\left(|\delta s_{i,j}|^2\right)$, by assuming $|\delta s_{i,j}| \ll 1$, the hooping parameter is rewritten as

$$T(|\tau_j + \delta s_{i,j}|) = \gamma_0 - \frac{\beta \gamma_0}{|\tau_j|^2} \tau_j \cdot \left(s(R_{A,i} + \tau_j) - s(R_{A,i})\right) \tag{2.46}$$

$$\simeq \gamma_0 - \frac{\beta \gamma_0}{|\tau_j|^2} \tau_j \cdot \mathcal{E} \tau_j \tag{2.47}$$

with

$$\beta = -\frac{|\tau_j|}{\gamma_0} \frac{\partial \gamma_0}{\partial r}. \tag{2.48}$$

The Hamiltonian is rewritten as

$$\tilde{H}_G = \begin{pmatrix} 0 & \tilde{\gamma}_0 \tilde{f}_k \\ \tilde{\gamma}_0 \tilde{f}_k^* & 0 \end{pmatrix}. \tag{2.49}$$

As we mentioned, we assume that the strain varies smoothly for the atomic scale. On this assumption, we can expand the Hamiltonian to the 1st order of $|k|$ and $\partial_\mu s$ around K_ξ as follows,

$$\tilde{H}_{G,\xi}(k) = -\hbar v \left[(I_2 + \mathcal{E})^{-1} \left(k + \frac{e}{\hbar} A \right) \right] \cdot \sigma, \tag{2.50}$$

where the $\boldsymbol{A}$ is the strain-induced vector potential that is given by [103, 104, 105]

$$\boldsymbol{A} = \xi \frac{3}{4} \frac{\beta \gamma_0}{ev} \begin{pmatrix} s_{xx} - s_{yy} \\ -2s_{xy} \end{pmatrix}, \tag{2.51}$$

$\gamma_0 = 2.7$ eV is the nearest neighbor transfer energy of intrinsic graphene and $\beta \approx 3.14$, and $s_{ij} = (\partial_i s_j + \partial_j s_i)/2$.

2.3.2 Rigid TBG

Next, we derive the Hamiltonian of the rigid TBG before the relaxed TBG. When twist angle is small, as Fig. 2.2(d) shows, two Dirac points $\boldsymbol{K}^{(l)}$ and $\boldsymbol{K}'^{(l)}$ are well separated for the scale of moiré BZ. So, the two valleys are not coupled to each other in this case. For this reason, the Hamiltonian of each valley is block diagonalized. And more, since the moiré BZ of TBG is smaller enough than the graphene's BZ, only the local band structure for each valley affects the low-energy region around the Fermi surface. We can use the effective Dirac Hamiltonian that is expanded as the 1st order of wave number as each graphene's Hamiltonian.

We use the basis $(\psi_A^{(1)}, \psi_B^{(1)}, \psi_A^{(2)}, \psi_B^{(2)})$ for each degree of freedom, sublattice and layer to construct Hamiltonian, here we remove the index of the valley ξ for simple notation. the Hamiltonian of TBG for K_ξ valley is

$$H^{(\xi)} = \begin{pmatrix} H_{G,\xi}^{(1)} & U^\dagger \\ U & H_{G,\xi}^{(2)} \end{pmatrix}. \tag{2.52}$$

Here, the diagonal part $H_{G,\xi}^{(l)}$ is the monolayer graphene Hamiltonian of layer $l = 1, 2$ that is given by Eq. (2.37)

$$H_{G,\xi}^{(l)} = -\hbar v \left[R(\mp\theta/2) \left(\boldsymbol{k} - \boldsymbol{K}_\xi^{(l)} \right) \right] \cdot \boldsymbol{\sigma}. \tag{2.53}$$

The rotation matrix $R(\mp\theta/2)$ comes from that each layer is rotated with $\mp\theta/2$. The sublattice vectors of each layer is written as $\boldsymbol{\tau}_j^{(l)} = R(\mp\theta)\boldsymbol{\tau}_j$ due to the relative

rotation. $R(\mp\theta/2)$ appears from the expansion of the hamiltonian Eq. (2.35) by this sublattice vectors.

U is the 2×2 matrix giving the interlayer moiré coupling between two layers. In the following, we derive this term as the continuum model[1, 56, 125].

The position of atom in layer $l(=1,2)$ is given as

$$\boldsymbol{R}_X^{(l)} = n_l \boldsymbol{a}_1^{(l)} + m_l \boldsymbol{a}_2^{(l)} + \boldsymbol{\tau}_X^{(l)}, \tag{2.54}$$

where $X = A, B$ is the label of the sublattice, n_l, m_l ($l = 1, 2$) are integers, and $\boldsymbol{\tau}_X^{(l)}$ is the position of the sublattice X in the unit cell of monolayer graphene of layer l. We assume that the distance of two graphene layers is d, so we define $\boldsymbol{\tau}_X^{(1)} \cdot \boldsymbol{e}_z = 0$, $\boldsymbol{\tau}_X^{(2)} \cdot \boldsymbol{e}_z = d$, here $\boldsymbol{e}_z$ is the unit vector along the z axis. As the previous section, we use the notation $\langle \boldsymbol{r} | \boldsymbol{R}_{X,i}^{(l)} \rangle \equiv \phi_X^{(l)}(\boldsymbol{r} - \boldsymbol{R}_{X,i})$, where $\phi_X^{(l)}(\boldsymbol{r} - \boldsymbol{R}_{X,i})$ is the wave function of X sublattice atom at $\boldsymbol{R}_{X,i}$ of layer l. As we mentioned on Eq. (2.52), we assume that the hooping function depends on only the distance between the atoms. Then the interlayer moiré coupling is written as follows,

$$U = - \sum_{\boldsymbol{R} \in \boldsymbol{R}_X^{(1)}} \sum_{\boldsymbol{R}' \in \boldsymbol{R}_{X'}^{(2)}} T(\boldsymbol{R} - \boldsymbol{R}') |\boldsymbol{R}'\rangle \langle \boldsymbol{R}| + \text{h.c..} \tag{2.55}$$

The Bloch wave function of each layer and sublattice can be defined as

$$|\boldsymbol{k}, X, l\rangle = \frac{1}{\sqrt{N_l}} \sum_{\boldsymbol{R} \in \boldsymbol{R}_X^{(l)}} e^{i\boldsymbol{k}\cdot\boldsymbol{R}} |\boldsymbol{R}\rangle, \tag{2.56}$$

where N_l is the number of atom of layer l in the total system having the area S_{tot}. Generally, two periods of both layers do not correspond each other in the atomic scale. However, we assume that $S_{\text{tot}} = N_1 S_1 = N_2 S_2$, where $S_l = |\boldsymbol{a}_1^{(l)} \times \boldsymbol{a}_2^{(l)}|$ is the area of unit cell for layer l. By using this wave function, the operator (2.55) is

36

expanded as follows,

$$U_{X'X;21}(\mathbf{k}', \mathbf{k}) \equiv \langle \mathbf{k}', X', 2 | U | \mathbf{k}, X, 1 \rangle \tag{2.57}$$

$$= -\frac{1}{\sqrt{N_1 N_2}} \sum_{\mathbf{R} \in \mathbf{R}_X^{(1)}} \sum_{\mathbf{R}' \in \mathbf{R}_{X'}^{(2)}} T(\mathbf{R} - \mathbf{R}') e^{i\mathbf{k} \cdot \mathbf{R} - i\mathbf{k}' \cdot \mathbf{R}'}. \tag{2.58}$$

We define the Fourier transform of the interlayer moiré hooping as

$$t(\mathbf{q}) = \frac{1}{S_1 S_2} \int d^2 \mathbf{r} T(\mathbf{r} + z_{X'X;l'l} \mathbf{e}_z) e^{-i\mathbf{q} \cdot \mathbf{r}}. \tag{2.59}$$

It is integrated for total area of the system S_{tot}. $z_{X'X;l'l} = (\boldsymbol{\tau}_{X'}^{(l)} - \boldsymbol{\tau}_X^{(l')}) \cdot \mathbf{e}_z$ is the z component of the different of $\boldsymbol{\tau}$ vectors. From Eq. (2.57) and (2.59), the matrix element of the interlayer moiré coupling is given by

$$U_{X'X;21}(\mathbf{k}', \mathbf{k}) = -\sum_{\mathbf{g}, \mathbf{g}'} t(\mathbf{k} + \mathbf{g}) e^{-i\mathbf{g} \cdot \boldsymbol{\tau}_X^{(1)} + i\mathbf{g}' \cdot \boldsymbol{\tau}_{X'}^{(2)}} \delta_{\mathbf{k}+\mathbf{g}, \mathbf{k}'+\mathbf{g}'}, \tag{2.60}$$

where we assume that $N_1 = N_2 = N$, and we use

$$\sum_{\mathbf{R} \in \mathbf{R}_X^{(l)}} e^{i(\mathbf{k} - \mathbf{k}' - \mathbf{g}') \cdot \mathbf{R}} = e^{i(\mathbf{k} - \mathbf{k}' - \mathbf{g}') \cdot \boldsymbol{\tau}_X} N \sum_{\mathbf{g}} \delta_{\mathbf{k} - \mathbf{k}' - \mathbf{g}', \mathbf{g}}. \tag{2.61}$$

The summation of $\mathbf{g}$ and $\mathbf{g}'$ in the Eq. (2.60) are taken for all reciprocal lattice vectors of each layer. Since $t_{X'X}(\mathbf{q})$ decays for enough large $|\mathbf{q}|$, we can take finite terms of Eq. (2.60) in the numerical calculation.

As we mentioned, for small twist angles, two valley of TBG are decoupled. So here, we consider the interlayer moiré coupling U around $\mathbf{K}$ valley. From equation (2.60), two wave vectors of each layer have a finite matrix element when these satisfy

$$\mathbf{k} + \mathbf{g} = \mathbf{k}' + \mathbf{g}'. \tag{2.62}$$

Here we ignore the $\mathbf{k}$ dependence of Eq. (2.60). we take all $\mathbf{k}'$ that can be coupled with $\mathbf{k} = \mathbf{K}^{(1)}$, and apply to all $\mathbf{k}$ points in Burilloun zone. This approximation is

valid only when the moiré BZ is sufficiently smaller than graphene BZ, in short, the twist angle is small enough. The figure 2.5 shows the $\boldsymbol{k}$ points which can couple with $\boldsymbol{K}^{(1)}$. Blue, triangle and white are $\boldsymbol{k}$ points with the norm $|\boldsymbol{K}|, |2\boldsymbol{K}|$ and $|\sqrt{7}\boldsymbol{K}|$ from $\boldsymbol{\Gamma}$. Since the Fourier form $t_{X'X}(\boldsymbol{q})$ rapidly decay for large $|\boldsymbol{q}|$, we take only the largest terms of the summation in Eq. (2.60) that correspond to blue points in Fig. 2.5. The interlayer moiré coupling is given by

$$U = u_0 \left[\begin{pmatrix} 1 & 1 \\ 1 & 1 \end{pmatrix} + \begin{pmatrix} 1 & \omega^* \\ \omega & 1 \end{pmatrix} e^{i\boldsymbol{G}_1 \cdot \boldsymbol{r}} + \begin{pmatrix} 1 & \omega \\ \omega^* & 1 \end{pmatrix} e^{i(\boldsymbol{G}_1 + \boldsymbol{G}_2) \cdot \boldsymbol{r}} \right], \qquad (2.63)$$

where $\omega = \exp(i 2\pi/3)$, $u_0 = t_{X'X}(\boldsymbol{K})(X', X = A, B)$. we calculated this at the wave points,, Similarly, the coupling term $\boldsymbol{K}'$ valley is calculated. Finally, the interlayer moiré coupling is given by

$$U = u_0 \left[M_1 + M_2 e^{i\xi \boldsymbol{G}_1 \cdot \boldsymbol{r}} + M_3 e^{i\xi(\boldsymbol{G}_1 + \boldsymbol{G}_2) \cdot \boldsymbol{r}} \right] \qquad (2.64)$$

for $\boldsymbol{K}_\xi$ valley, where we define the matrixes

$$M_1 = \begin{pmatrix} 1 & 1 \\ 1 & 1 \end{pmatrix}, \quad M_2 = \begin{pmatrix} 1 & \omega^{-\xi} \\ \omega^{+\xi} & 1 \end{pmatrix}, \quad M_3 = \begin{pmatrix} 1 & \omega^{+\xi} \\ \omega^{-\xi} & u \end{pmatrix}.$$

For the analytic calculation, the Hamiltonian applied the unitary transformation is useful. We consider the unitary transformation $(\psi_A^{(1)}, \psi_B^{(1)}, \psi_A^{(2)}, \psi_B^{(2)})^t = \mathcal{U}(\bar{\psi}_A^{(1)}, \bar{\psi}_B^{(1)}, \bar{\psi}_A^{(2)}, \bar{\psi}_B^{(2)})^t$, where

$$\mathcal{U}_\xi = \begin{pmatrix} e^{i\boldsymbol{K}_\xi^{(1)} \cdot \boldsymbol{r}} & 0 \\ 0 & e^{i\boldsymbol{K}_\xi^{(2)} \cdot \boldsymbol{r}} \end{pmatrix} \qquad (2.65)$$

is the unitary 4×4 matrix for $\boldsymbol{K}_\xi$-valley. This transformation takes a different

gauge for each layer. The Hamiltonian is written as

$$
\bar{H}^{(\xi)} = \mathcal{U}_\xi^\dagger H^{(\xi)} \mathcal{U}_\xi = \begin{pmatrix} -\hbar v \left[R\left(-\theta/2\right) \boldsymbol{k} \right] \cdot \boldsymbol{\sigma} & \bar{U}^\dagger \\ \bar{U} & -\hbar v \left[R\left(+\theta/2\right) \boldsymbol{k} \right] \cdot \boldsymbol{\sigma} \end{pmatrix}, \quad (2.66)
$$

where

$$
\bar{U} = \sum_{j=1}^{3} u_0 M_j \mathrm{e}^{\mathrm{i}\xi \boldsymbol{q}_j \cdot \boldsymbol{r}}, \quad (2.67)
$$

and we define

$$
\boldsymbol{q}_1 = \boldsymbol{K}_+^{(1)} - \boldsymbol{K}_+^{(2)},
$$

$$
\boldsymbol{q}_j = R(2\pi/3)\boldsymbol{q}_1 \quad (j = 2, 3).
$$

Figure 2.6 represents the band structure calculated from Eq. (2.52) and (2.64). We use the parameters $\hbar v/a = 2.1435$ eV, $u_0 = 110$ eV. We included the $\boldsymbol{k}$ points that are in the circle with radius $4|\boldsymbol{G}_1|$ as the basis of the Hamiltonian, and we take the path shown in Fig. 2.2(b) as a red line.

2.3.3 Distorted lattice

From here on, we consider the distorted TBG, and drive the continuum Hamiltonian[42]. Here, we also assume that the distortion of lattice is continuum function $\boldsymbol{s}_X^{(l)}$ as the real space $\boldsymbol{r}$.

On the basis $(\psi_A^{(1)}, \psi_B^{(1)}, \psi_A^{(2)}, \psi_B^{(2)})$, the Hamiltonian of distorted TBG for K_ξ valley is written as

$$
\tilde{H}^{(\xi)} = \begin{pmatrix} \tilde{H}_{G,\xi}^{(1)} & \tilde{U}^\dagger \\ \tilde{U} & \tilde{H}_{G,\xi}^{(2)} \end{pmatrix}. \quad (2.68)
$$

The diagonal term $\tilde{H}_{G,\xi}^{(l)}$ is the strained graphene Hamiltonian of layer $l = 1, 2$

39
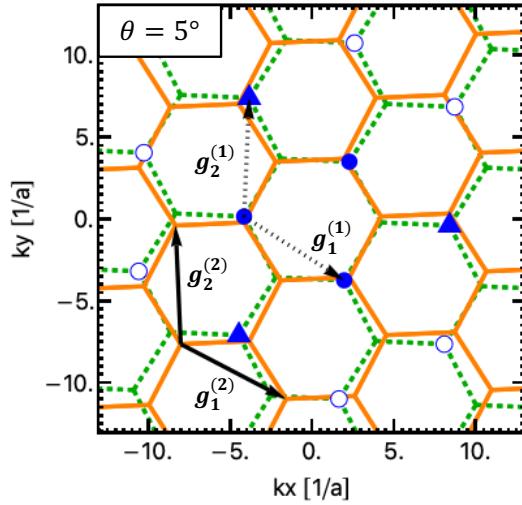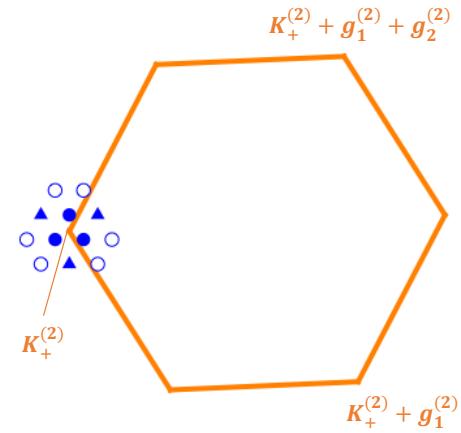
Figure 2.5: (a) Brillouin zones of bottom (green) and top (orange) graphene in the extended zone scheme. Each symbols (filled circle, triangle and open circle) represent the position of $K^{(1)} + G$ for several G, here different symbols have a different distance from the origin of k-space. (b) Corresponding position of symbols of (a) around the K point of top layer $K^{(2)}$.
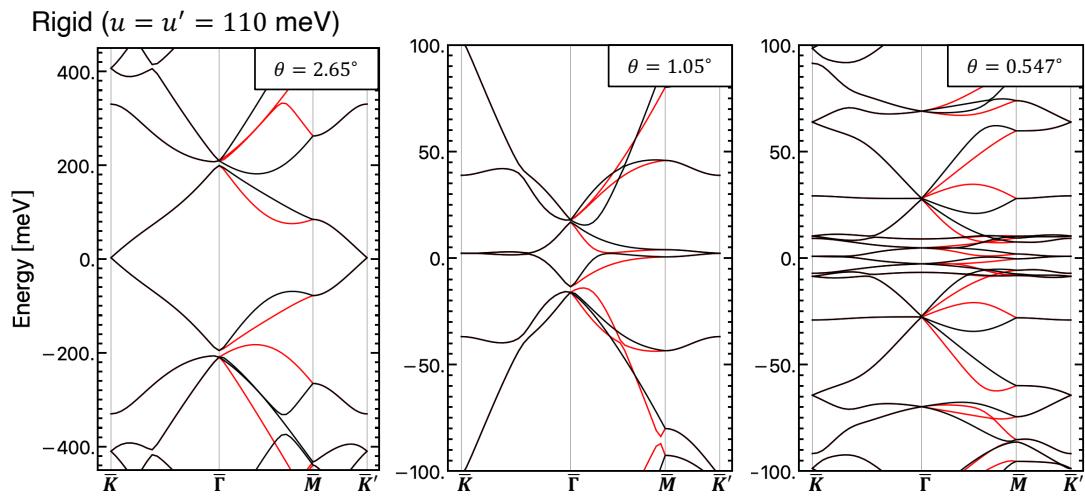
Figure 2.6: Energy band structure of rigid TBG at $\theta = 2.65°$, (midlle) $1.05°$ and (right) $0.547°$, where black and red lines represent energy band of K and K'-valley respecticelly.

40

around K_ξ valley [Eq. (2.50)]s

$$\tilde{H}^{(l)}_{G,\xi} = -\hbar v \left[R\left(\mp\theta/2\right)\left(\mathbf{k} - \mathbf{K}^{(l)}_\xi + \frac{e}{\hbar}\mathbf{A}^{(l)}\right)\right] \cdot \boldsymbol{\sigma}, \tag{2.69}$$

where $\mathbf{A}^{(l)}$ is the strain-induced vector potential that is given by Eq. (2.51).

Next, we consider the off-diagonal term $\tilde{U}$ of Eq. (2.68). It's given by the matrix element of the interlayer moiré coupling

$$\tilde{U} = -\sum_{\mathbf{R}\in\mathbf{R}^{(1)}_X}\sum_{\mathbf{R}'\in\mathbf{R}^{(2)}_{X'}} T\left(\mathbf{R} + \mathbf{s}^{(1)}_X(\mathbf{R}) - \mathbf{R}' - \mathbf{s}^{(2)}_{X'}(\mathbf{R})\right)\left|\mathbf{R}' + \mathbf{s}^{(2)}_{X'}(\mathbf{R}')\right\rangle\left\langle\mathbf{R} + \mathbf{s}^{(1)}_X(\mathbf{R})\right| + \text{h.c.}, \tag{2.70}$$

expanded by the Bloch basis under the lattice distortion $|\mathbf{k}, X, l\rangle$. We define it as

$$|\mathbf{k}, X, l\rangle = \frac{1}{\sqrt{N}}\sum_{\mathbf{R}\in\mathbf{R}_{X_l}} e^{i\mathbf{k}\cdot\mathbf{R}}\left|\mathbf{R} + \mathbf{s}^{(l)}_X(\mathbf{R})\right\rangle, \tag{2.71}$$

where $\mathbf{k}$ is a two-dimensional Bloch wave vector, and $N = S/S_0$ is the number of graphene's unit cells per layer in the total system area S. The interlayer matrix element between the Bloch basis is written as

$$\langle\mathbf{k}', X', 2|\tilde{U}|\mathbf{k}, X, 1\rangle$$
$$= -\frac{1}{N}\sum_{\mathbf{R}\in\mathbf{R}^{(1)}_X}\sum_{\mathbf{R}'\in\mathbf{R}^{(2)}_{X'}} e^{i\mathbf{k}\cdot\mathbf{R}-i\mathbf{k}'\cdot\mathbf{R}'} T\left(\mathbf{R}' + \mathbf{s}^{(2)}_{X'}(\mathbf{R}') - \mathbf{R} - \mathbf{s}^{(1)}_X(\mathbf{R})\right)$$
$$= -\frac{1}{N}\frac{S_0 d_0}{(2\pi)^3}\int \mathrm{d}^3 p\, t(\mathbf{p})$$
$$\times \sum_{\mathbf{R}\in\mathbf{R}^{(1)}_X} e^{i(\mathbf{k}-\mathbf{p})\cdot\mathbf{R}-i\mathbf{p}\cdot\mathbf{s}X^{(1)}(\mathbf{R})}\sum_{\mathbf{R}'\in\mathbf{R}^{(2)}_{X'}} e^{-i(\mathbf{k}'-\mathbf{p})\cdot\mathbf{R}'+i\mathbf{p}\cdot\mathbf{s}X'^{(2)}(\mathbf{R}')}. \tag{2.72}$$

We replace $\mathbf{s}^{(1)}_X(\mathbf{R})$ and $\mathbf{s}^{(2)}_{X'}(\mathbf{R}')$ with its Fourier transform in Eq. (2.23) and expand the exponential functions such as $\exp(i\mathbf{p}\cdot\mathbf{s}_q e^{i\mathbf{q}\cdot\mathbf{R}})$ in a Taylor series as

$$\exp\left(i\mathbf{p}\cdot\mathbf{s}_q e^{i\mathbf{q}\cdot\mathbf{R}}\right) = \sum_{n=0}^{\infty}\frac{1}{n!}(i\mathbf{p}\cdot\mathbf{s}_q)^n e^{in\mathbf{q}\cdot\mathbf{R}}. \tag{2.73}$$

41

Then we can take the summation over the lattice points by using

$$\sum_{\boldsymbol{R} \in \boldsymbol{R}_X^{(l)}} \mathrm{e}^{\mathrm{i}\boldsymbol{p}\cdot\boldsymbol{R}} = N \sum_{\boldsymbol{g}} \mathrm{e}^{\mathrm{i}(\boldsymbol{g}+p_z\boldsymbol{e}_z)\cdot\boldsymbol{\tau}_X^{(l)}} \delta_{\boldsymbol{p}_{||},\boldsymbol{g}}, \tag{2.74}$$

where $\boldsymbol{p}_{||}$ is the xy component of the vector $\boldsymbol{p}$, and the summation of $\boldsymbol{g}$ is taken over all the recprocal lattice vectors $\boldsymbol{g} = m_1\boldsymbol{b}_1^{(l)} + m_2\boldsymbol{b}_2^{(l)}$. Using these, we get a formula

$$\langle \boldsymbol{k}', X', 2 | \tilde{U} | \boldsymbol{k}, X, 1 \rangle$$
$$= \sum_{\boldsymbol{g},\boldsymbol{g}'} \sum_{n_1,n_2,\dots} \sum_{n_1',n_2',\dots} \Gamma_{(n_1,n_2,\dots)}^{(n_1',n_2',\dots)}(\boldsymbol{Q}) \mathrm{e}^{-\mathrm{i}\boldsymbol{g}\cdot\boldsymbol{\tau}_X^{(l)}+\mathrm{i}\boldsymbol{g}'\cdot\boldsymbol{\tau}_{X'}^{(2)}} \delta_{\boldsymbol{k}+\boldsymbol{g}+n_1\boldsymbol{q}_1+n_2\boldsymbol{q}_2+\dots,\boldsymbol{k}'+\boldsymbol{g}'-n_1'\boldsymbol{q}_1-n_2'\boldsymbol{q}_2+\dots},$$

$$\tag{2.75}$$

where $\boldsymbol{g} = m_1\boldsymbol{b}_1^{(1)} + m_2\boldsymbol{b}_2^{(1)}$ and $\boldsymbol{g}' = m_1'\boldsymbol{b}_1^{(2)} + m_2'\boldsymbol{b}_2^{(2)}$, $n_i, n_i' = 0, 1, 2, \dots$, $\boldsymbol{Q} = \boldsymbol{k} + \boldsymbol{g} + n_1\boldsymbol{q}_1 + n_2\boldsymbol{q}_2 + \dots$ and

$$\Gamma_{(n_1,n_2,\dots)}^{(n_1',n_2',\dots)}(\boldsymbol{Q}) = -\frac{d_0}{2\pi}\int_{-\infty}^{\infty} \mathrm{d}p_z t(\boldsymbol{Q}') \mathrm{e}^{\mathrm{i}p_z d_0}$$
$$= \times \frac{\left[-\mathrm{i}\boldsymbol{Q}'\cdot\boldsymbol{s}_{X,\boldsymbol{q}_1}^{(1)}\right]^{n_1}}{n_1!} \frac{\left[-\mathrm{i}\boldsymbol{Q}'\cdot\boldsymbol{s}_{X,\boldsymbol{q}_2}^{(1)}\right]^{n_2}}{n_2!}\dots$$
$$\times \frac{\left[+\mathrm{i}\boldsymbol{Q}'\cdot\boldsymbol{s}_{X',\boldsymbol{q}_1}^{(2)}\right]^{n_1'}}{n_1'!} \frac{\left[+\mathrm{i}\boldsymbol{Q}'\cdot\boldsymbol{s}_{X',\boldsymbol{q}_2}^{(2)}\right]^{n_2'}}{n_2!}\dots \tag{2.76}$$

here $\boldsymbol{Q}' = \boldsymbol{Q} + p_z\boldsymbol{e}_z$. In the above formula, $\boldsymbol{q}_i$ is the two dimensional wave numbers in which $\boldsymbol{u}_{X,\boldsymbol{q}}^{(l)}$ has finite Fourier amplitude. Similar to the rigid case, Eq. (2.75) means the Bloch state of layer 1 and layer 2 are coupled when

$$\boldsymbol{k} + \boldsymbol{g} + n_1\boldsymbol{q}_1 + n_2\boldsymbol{q}_2 + \dots = \boldsymbol{k}' + \boldsymbol{g}' - n_1'\boldsymbol{q}_1 - n_2'\boldsymbol{q}_2 + \dots (= \boldsymbol{Q}). \tag{2.77}$$

The amplitude of coupling is given by $\Gamma_{(n_1,n_2,\dots)}^{(n_1',n_2',\dots)}(\boldsymbol{Q})$.

From here on, we assume that the distortion has only in-plane component, in

short, $s_z^{(l)} = 0$. On this assumption, Eq. (2.76) is replaced as

$$\Gamma_{(n_1,n_2,...)}^{(n'_1,n'_2,...)}(\boldsymbol{Q}) = - t_{\parallel}(\boldsymbol{Q}; d_0) \frac{\left[-\mathrm{i}\boldsymbol{Q} \cdot \boldsymbol{s}_{X,\boldsymbol{q}_1}^{(1)}\right]^{n_1}}{n_1!} \frac{\left[-\mathrm{i}\boldsymbol{Q} \cdot \boldsymbol{s}_{X,\boldsymbol{q}_2}^{(1)}\right]^{n_2}}{n_2!} \cdots$$
$$\times \frac{\left[+\mathrm{i}\boldsymbol{Q} \cdot \boldsymbol{s}_{X',\boldsymbol{q}_1}^{(2)}\right]^{n'_1}}{n'_1!} \frac{\left[+\mathrm{i}\boldsymbol{Q} \cdot \boldsymbol{s}_{X',\boldsymbol{q}_2}^{(2)}\right]^{n'_2}}{n_2!} \cdots \quad (2.78)$$

where

$$t_{\parallel}(\boldsymbol{Q}; z) = \frac{d_0}{2\pi} \int_{-\infty}^{\infty} \mathrm{d}p_z t(\boldsymbol{Q} + p_z \boldsymbol{e}_z) \mathrm{e}^{\mathrm{i}p_z z}$$
$$= \frac{1}{S_0} \int \mathrm{d}^2 \boldsymbol{r} T(\boldsymbol{r} + z\boldsymbol{e}_z) \mathrm{e}^{-\mathrm{i}\boldsymbol{Q} \cdot \boldsymbol{r}} \quad (2.79)$$

is the two dimensional Fourier transform of $T(\boldsymbol{r})$ on a plane parallel to xy at fixed height z. In the absence of the lattice distortion (i.e. $\boldsymbol{s}_X^{(l)} = 0$), the above formula exactly matches Eq. (2.59).

Eq. (2.75) is the general formula of the matrix element of the interlayer coupling. From here on, we apply it to the twisted bilayer graphene. We also assume that the displacement vector does not depend on the degree of the sublattice $\boldsymbol{s}_A^{(l)} = \boldsymbol{s}_B^{(l)} = \boldsymbol{s}^{(l)}$. We also assume that the moiré period is large enough similar to the rigid case. Then we can use the same approximation which takes only the largest terms at $\boldsymbol{k} = \boldsymbol{K}_\xi$, $\boldsymbol{K}_\xi + \boldsymbol{b}_1$, $\boldsymbol{K}_\xi + \boldsymbol{b}_1 + \boldsymbol{b}_2$. The matrix element is written as

$$\langle \boldsymbol{k}', X', 2| \tilde{U} |\boldsymbol{k}, X, 1\rangle = \sum_{j=1}^{3} \sum_{n_1,n_2,...} \sum_{n'_1,n'_2,...} \Gamma_{(n_1,n_2,...)}^{(n'_1,n'_2,...)}(\boldsymbol{Q}_j) \left[M_j\right]_{X'X} \delta_{\boldsymbol{k}',\boldsymbol{k}+\delta\boldsymbol{k}_j(n_1+n'_1)\boldsymbol{q}_1+(n_2+n'_2)\boldsymbol{q}_2+...},$$
$$(2.80)$$

where $\delta\boldsymbol{k}_j(= \boldsymbol{g} - \boldsymbol{g}')$ is given by

$$\delta\boldsymbol{k}_1 = 0, \quad \delta\boldsymbol{k}_2 = \xi\boldsymbol{G}_1, \quad \delta\boldsymbol{k}_3 = \xi(\boldsymbol{G}_1 + \boldsymbol{G}_2), \quad (2.81)$$

and we define

$$\boldsymbol{Q}_1 = \boldsymbol{K}_\xi, \quad \boldsymbol{Q}_j = R\left(\frac{2\pi}{3}(j - 1)\right)\boldsymbol{Q}_1 \quad (j = 2, 3). \quad (2.82)$$

43

The matrix M_j are defined at (2.65). In the real space representation, Eq. (2.80) is simply written as

$$\langle \boldsymbol{k}', X', 2| \, \tilde{U} \, |\boldsymbol{k}, X, 1\rangle = \frac{1}{S} \int \mathrm{d}^2 \boldsymbol{r} \mathrm{e}^{\mathrm{i}(\boldsymbol{k}-\boldsymbol{k}')\cdot\boldsymbol{r}} U_{X'X}(\boldsymbol{r}), \tag{2.83}$$

where

$$\tilde{U}(\boldsymbol{r}) = -\sum_{j=1}^{3} M^j \, t_{\parallel} \left[\boldsymbol{Q}_j ; d_0 + s_z^-(\boldsymbol{r}) \right] \exp\left[\mathrm{i}\boldsymbol{Q}_j \cdot \boldsymbol{s}^-(\boldsymbol{r}) + \mathrm{i}\delta\boldsymbol{k}_j \cdot \boldsymbol{r} \right]. \tag{2.84}$$

Specially, when $s_z^{(l)} = 0$, Eq. (2.84) becomes

$$\tilde{U}(\boldsymbol{r}) = u_0 \sum_{j=1}^{3} M^j \exp\left[\mathrm{i}\boldsymbol{Q}_j \cdot \boldsymbol{s}^-(\boldsymbol{r}) + \mathrm{i}\delta\boldsymbol{k}_j \cdot \boldsymbol{r} \right]. \tag{2.85}$$

The black like of figure 2.7 represents the band structure calculated from Eq. (2.68), and red line is band structure of non-relaxed for the comparison. We use the parameters $\hbar v/a = 2.1435$ eV, $u_0 = 110$ eV. We included the $\boldsymbol{k}$ points that are in the circle with radius $4|\boldsymbol{G}_1|$ as the basis of the Hamiltonian, and we take the path shown in Fig. 2.2(b) as a red line. For the band calculation of relaxed TBG, we use the displacement vector $\boldsymbol{s}^{(l)}$ that is given by the self-consistent equation (2.21) for each angle. We see that the lattice relaxation modulates the band structure, specially at $\theta = 1.05°$, it gives the gap between the flat band and secondary bands. Since lattice relaxation is more dominant in the smaller angle, the effect of lattice relaxation is more pronounced at smaller angles.
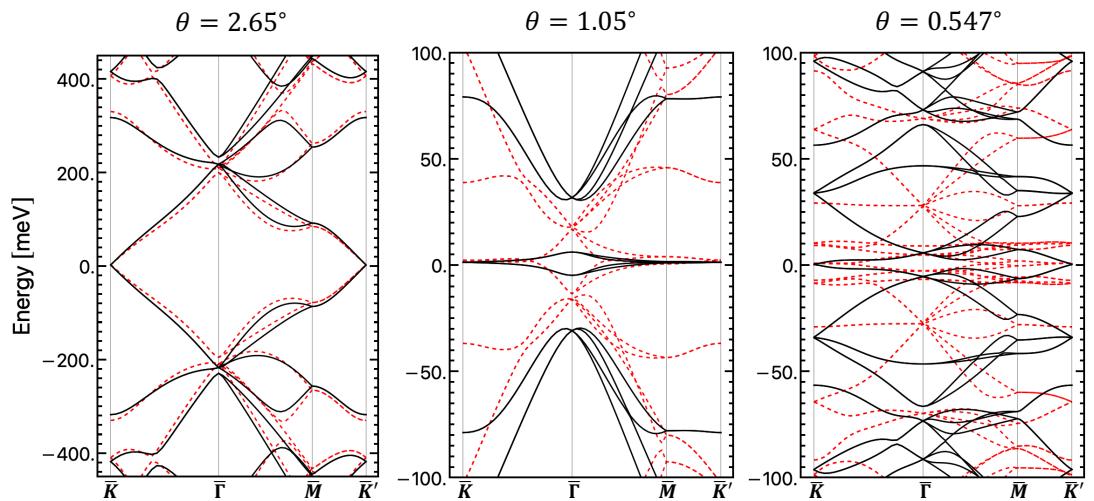
Figure 2.7: Energy band structure of rigid TBG at $\theta = 2.65°$, (midlle) $1.05°$ and (right) $0.547°$, where black and red lines represent energy band of relaxed and non-relaxed TBG respecticelly.

Chapter 3

Multi-scale lattice relaxation in twisted trilayer graphene

In this chapter, we study the lattice relaxation and the electronic band structure in non-symmetric twisted trilayer graphenes (TTGs). We find that there are two distinct length-scale relaxations in the moiré-of-moiré and moiré scales, which give rise to a formation of a patchwork of super-moiré domains as schematically shown in Fig. 3.1. In theses domains, the first moiré pattern given by layer 1 and 2 (moiré 12) and the second pattern by layer 2 and 3 (moiré 23) are deformed to become commensurate.

The atomic configuration inside the domain exhibits a distinct contrast between chiral and alternating stacks, which are determined by the relative signs of the two twist angles. For chiral stack, band calculation reveals that the spectrum has an energy window more than 50 meV wide with low density of state, where highly one-dimensional electron bands are sparsely distributed. The wave function of the one-dimensional bands is sharply localized at the boundary between the super-moiré domains. By calculating the Chern number of the local band structure of the commensurate domains, the one-dimensional state is shown to be a topological boundary state between distinct Chern insulators. On the other hand, the alternating TTG exhibits a coexistence of the flat bands and a monolayer-like Dirac cone, and it is attributed to the formation of moiré-of-moiré domains equivalent to the mirror-symmetric twisted trilayer graphene.
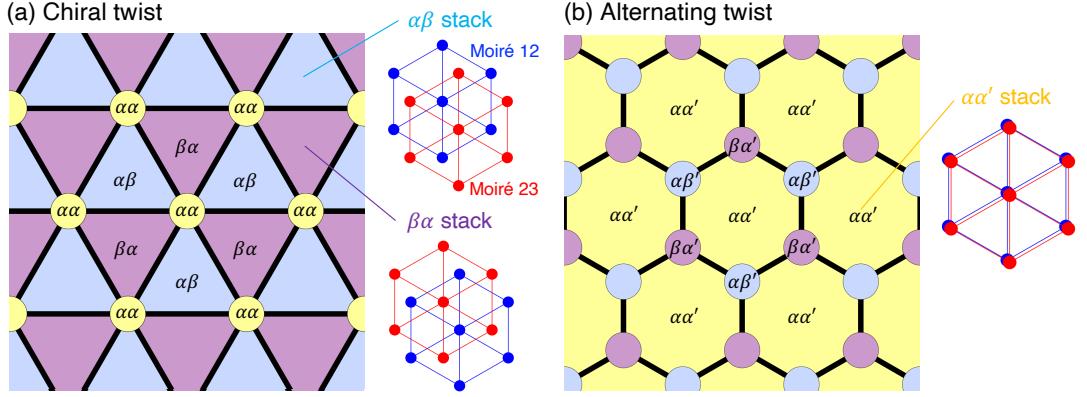
Figure 3.1: Schematic illustration of the moiré-of-moiré domain structures in (a) chiral TTG and (b) alternating TTG with close twist angles. Right figures represent relative arrangements of two moiré patterns within the domains, where blue and red dots indicate AA stacking of moiré 12 (between layer 1 and 2) and of moiré 23 (between layer 2 and 3), respectively (See also Fig. 3.2).

3.1 Model

3.1.1 Geometry of TTG

We define a TTG by stacking three graphene layers labeled by $l = 1, 2$ and 3, with relative twist angles θ^{12} (layer 1 to 2) and θ^{23} (layer 2 to 3). The configuration is schematically depicted in Fig. 3.2(a) and (b), for the chiral case ($\theta^{12} \cdot \theta^{23} > 0$) and the alternating case ($\theta^{12} \cdot \theta^{23} < 0$), respectively. The primitive lattice vectors of layer l are defined by $\boldsymbol{a}_i^{(l)} = R(\theta^{(l)})\boldsymbol{a}_i$ where $\boldsymbol{a}_1 = a(1, 0)$ and $\boldsymbol{a}_2 = a(1/2, \sqrt{3}/2)$ are the lattice vectors of unrotated monolayer graphene, $a = 0.246$ nm is the graphene's lattice constant. R is the rotation matrix, and $\theta^{(l)}$ is the absolute twist angle of layer l given by $\theta^{(1)} = -\theta^{12}$, $\theta^{(2)} = 0$ and $\theta^{(3)} = \theta^{23}$. Accordingly, the primitive reciprocal lattice vectors become $\boldsymbol{b}_i^{(l)} = R(\theta^{(l)})\boldsymbol{b}_i$ where $\boldsymbol{b}_1 = (2\pi/a)(1, -1/\sqrt{3})$ and $\boldsymbol{b}_2 = (2\pi/a)(0, 2/\sqrt{3})$ are the reciprocal lattice vectors without rotation. The Dirac points of graphene layer l are intrinsically located at the corners of Brillouin zone (BZ), $K_\xi^{(l)} = -\xi \left(2\boldsymbol{b}_1^{(l)} + \boldsymbol{b}_2^{(l)}\right)/3$ where $\xi = \pm 1$ is the valley index.

In this thesis, we consider TTGs with small twist angles ($|\theta^{12}|, |\theta^{23}| \lesssim 10°$).

Then the system is governed by two competing moiré patterns, one from the layer 1 and 2 and the other from layer 2 and 3. The reciprocal lattice vectors for these moiré patterns are given by $\boldsymbol{G}_i^{ll'} = \boldsymbol{b}_i^{(l)} - \boldsymbol{b}_i^{(l')}$ where $(l, l') = (1, 2)$ or $(2, 3)$. The moiré lattice vectors can be obtained from $\boldsymbol{G}_i^{ll'} \cdot \boldsymbol{L}_j^{ll'} = 2\pi\delta_{ij}$, and explicitly written as

$$\boldsymbol{L}_1^{12} = \frac{a}{2\sin{(\theta^{12}/2)}} R(-\theta^{12}/2) \begin{pmatrix} 0 \\ -1 \end{pmatrix}$$

$$\boldsymbol{L}_1^{23} = \frac{a}{2\sin{(\theta^{23}/2)}} R(\theta^{23}/2) \begin{pmatrix} 0 \\ -1 \end{pmatrix}, \tag{3.1}$$

and $\boldsymbol{L}_2^{ll'} = R(60°)\boldsymbol{L}_1^{ll'}$. The moiré lattice constant is given by $L^{ll'} = |\boldsymbol{L}_1^{ll'}| = |\boldsymbol{L}_2^{ll'}| = a/|2\sin{(\theta^{ll'}/2)}|$.

When absolute twist angles are close ($|\theta^{12}| \approx |\theta^{23}|$), an interference between the two moiré patterns gives rise to a higher order structure called a moiré-of-moiré pattern as shown in Fig. 3.2. Here the upper and lower rows correspond to the chiral and alternating structures, respectively. For the chiral twist, the left panel [Fig. 3.2(a)] illustrates the overlapped moiré patterns where blue and red dots represent the AA spots of moiré 12 and 23, respectively. The local structure can be viewed as a pair of non-twisted moiré superlattices with a relative translation, as illustrated in Fig. 3.2(b). Here shaded and empty triangles represent AB, and BA stacking regions of individual moiré patterns, respectively. By defining AB and BA points (the centers of triangles) by α and β, respectively, the local stacking configuration of the two moiré patterns is labeled by $\alpha\alpha$, $\alpha\beta$ and $\beta\alpha$. Figure 3.2(c) depicts the local structure in the atomic scale. Here A_l and B_l represent the graphene's sublattice in layer l. We define the sublattice C_l as the center of the hexagon in the honeycomb lattice. For instance, BAC-stacking represents B_1, A_2 and C_3 are vertically aligned.

The lower panels [Figs. 3.2(d), (e) and (f)] are the corresponding figures for the alternate twist. The key difference from the chiral case lies in the 180° rotation

of the moiré 23 (red lattice) due to the opposing sign of θ^{23}. This results in the flipping of the positions of AB and BA. Consequently, the local atomic structure (shown in the rightmost panels) differs between the chiral and alternating structures, even though the relative arrangement of AA spots is identical. We define AB and BA points in the inverted moiré 23 pattern by β' and α', respectively, and label the local structure in the alternating TTG by $\alpha\alpha'$, $\alpha\beta'$ and $\beta\alpha'$, as in Fig. 3.2(e).

3.1.2 Commensurate TTGs

Generally the two moiré patterns in a TTG are not commensurate, and the spatial period of moiré-of-moiré pattern is infinite. However, there are special angle sets $(\theta^{12}, \theta^{23})$ where the two patterns happen to have a finite common period. In such a case, we can express the moiré-of-moiré primitive lattice vectors $\boldsymbol{L}_1$ and $\boldsymbol{L}_2$ in terms of integers n, m, n' and m' as

$$\boldsymbol{L}_1 = n\boldsymbol{L}_1^{12} + m\boldsymbol{L}_2^{12} = n'\boldsymbol{L}_1^{23} + m'\boldsymbol{L}_2^{23},$$
$$\boldsymbol{L}_2 = R(60°)\boldsymbol{L}_1. \tag{3.2}$$

The moiré-of-moiré reciprocal lattice vectors are given by the condition $\boldsymbol{G}_i \cdot \boldsymbol{L}_j = 2\pi\delta_{ij}$. The corresponding twist angles are obtained by solving Eqs. (3.1) and (3.2) for variables θ^{12} and θ^{23}, as

$$\theta^{12} = \theta(n, m, n', m'), \quad \theta^{23} = -\theta(n', m', n, m), \tag{3.3}$$

where

$$\theta(n, m, n', m') =$$
$$2\tan^{-1}\frac{\sqrt{3}\,\{m\,(2n' + m') - (2n + m)\,m'\}}{(2n + m)\,(2n' + m') + 3mm' + (2n' + m')^2 + 3m'^2}. \tag{3.4}$$
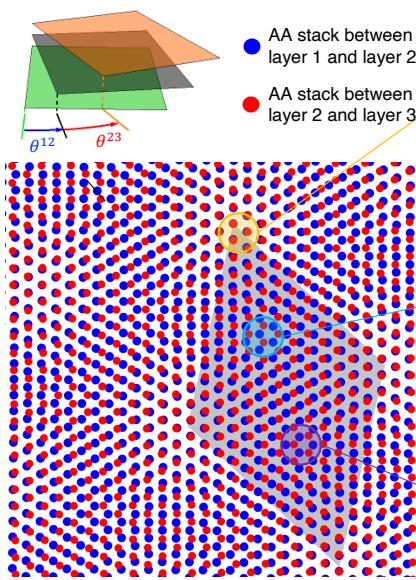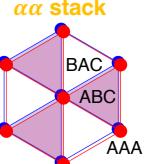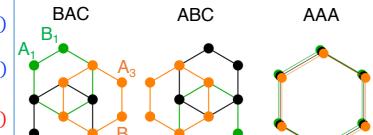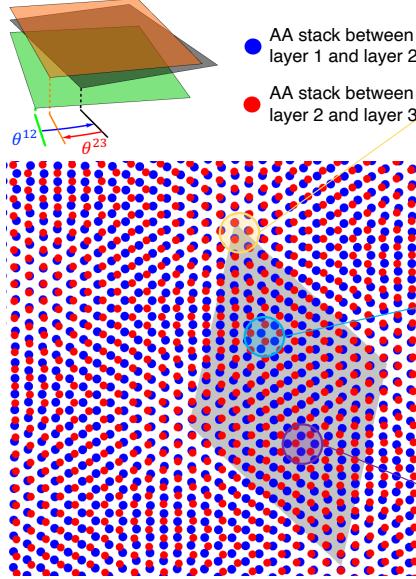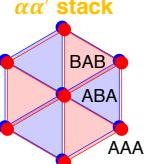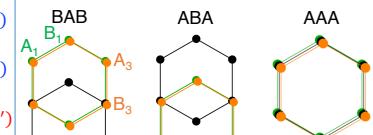
Figure 3.2: (a) Schematics of moiré-of-moiré pattern of chiral TTG, where blue and red dots represent AA stacking points of moiré 12 (between layer 1 and 2) and of moiré 23 (between layer 2 and 3), respectively. The insert panel illustrates the stacking structure of a chiral TTG, where green, black and orange represent the layer 1, 2 and 3 respectively. (b) Local structures of moiré-of-moiré pattern in (a), where circles, filled triangles, and empty triangles indicate AA, AB, and BA stacking of individual moiré patterns. (c) Local atomic structures at specific points in (b), where A_l and B_l are the graphene's sublattice in layer l. The lower panels [(d), (e) and (f)] are the corresponding figures for the alternate TTG.

50
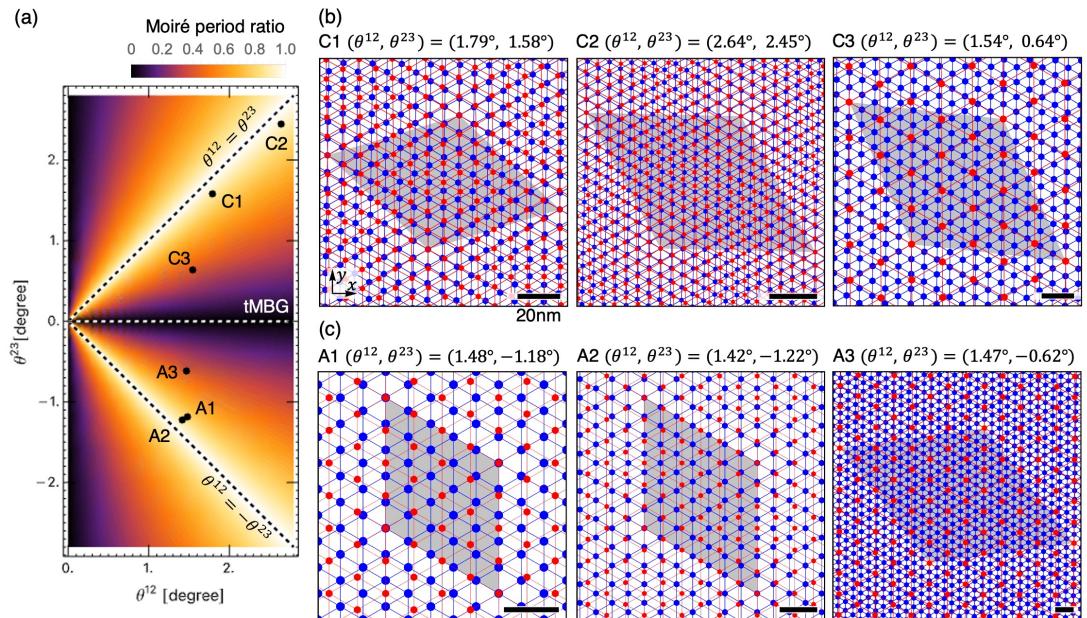
Figure 3.3: (a) Two-dimensional map of $(\theta^{12}, \theta^{23})$ of TTGs considered in this thesis. The color code represents the ratio of the two moiré periods, $\min\left(L^{12}/L^{23}, L^{23}/L^{12}\right)$. Diagonal dashed lines indicate $\theta^{12} = \pm\theta^{23}$, and a horizontal dashed line represents twisted monolayer-bilayer graphene (tMBG). (Right) Moiré-of-moiré patterns without lattice relaxation of (b) chiral TTGs (C1, C2 and C3) and (c) alternating TTGs (A1, A2 and A3). Blue and red dots indicate the AA spot of moiré 12 (between layer 1 and 2) and moiré 23 (between layer 2 and 3) respectively, and gray area represents the moiré-of-moiré unit cell. All scale bars indicate 20 nm.

	$(\theta^{12}, \theta^{23})$	(n, m, n', m')	L^{12}/L^{23}
C1	$(1.79°, 1.58°)$	$(2, 7, 2, 6)$	0.88
C2	$(2.64°, 2.45°)$	$(7, 7, 7, 6)$	0.93
C3	$(1.54°, 0.64°)$	$(7, 5, 3, 2)$	0.42
A1	$(1.48°, -1.18°)$	$(5, 0, -4, 0)^*$	0.80
A2	$(1.42°, -1.22°)$	$(7, 0, -6, 0)^*$	0.86
A3	$(1.47°, -0.62°)$	$(7, 12, -3, -5)$	0.42

Table 3.1: Definition of commensurate chiral TTGs (C1, C2, C3) and commensurate alternating TTGs (A1, A2, A3) considered in this thesis. The asterisk (*) symbol for A1 and A2 indicates the use of the approximation of Eq. (3.5) to obtain the commensurate structures.

The spatial period of the super-moiré pattern is given by $L = L^{12}\sqrt{n^2 + m^2 + nm} = L^{23}\sqrt{n'^2 + m'^2 + n'm'}$.

In alternating TTGs with $\theta^{12} \approx -\theta^{23}$, the relative angle between two moiré lattice vectors nearly vanishes, resulting in an extremely large commensurate moiré-of-moiré unit cell. To treat such cases, we neglect the tiny misorientation of the moiré lattice vectors $\boldsymbol{L}_j^{12}$ and $\boldsymbol{L}_j^{23}$, while retaining their norms. In this approximation, the moiré-of-moiré commensurate period is expressed as

$$\boldsymbol{L}_1 = n\boldsymbol{L}_1^{12} = n'\boldsymbol{L}_1^{23}, \quad \boldsymbol{L}_2 = R(60°)\boldsymbol{L}_1, \tag{3.5}$$

instead of Eq.(3.2). Note that Eq. (3.3) does not apply to this approximate commensurate structure.

In this thesis, we consider commensurate chiral TTGs, C1, C2 and C3, and commensurate alternating TTGs, A1, A2 and A3, defined in Table 3.1. We employ the exact commensurate formulas Eqs. (3.2) and (3.3) for C1, C2, C3, and A3, while we utilize the approximate formula, Eq. (3.5) for A1 and A2. Figure 3.3(a) maps $(\theta^{12}, \theta^{23})$ of these systems in two-dimensional space, where the color code represents the ratio of the two moiré periods, $\min\left(L^{12}/L^{23}, L^{23}/L^{12}\right)$. The moiré-of-moiré structures of these TTGs without lattice relaxation are illustrated in Fig. 3.3(b) and (c), respectively.

We show the schematics of Brillouin zone (BZ) of a chiral TTG for a commen-
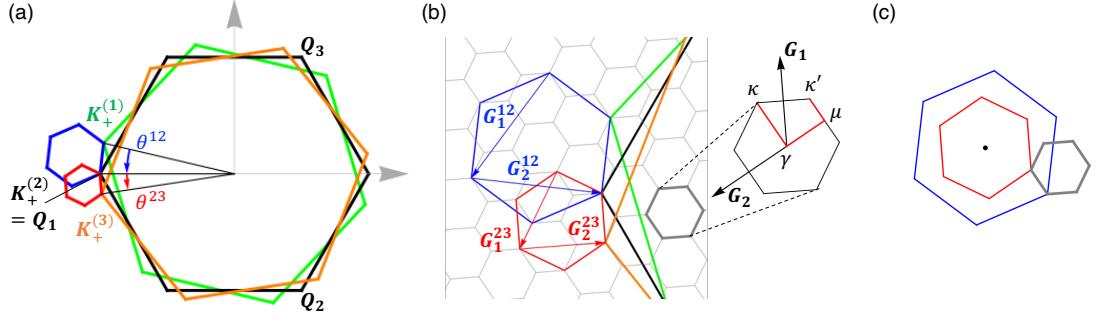
Figure 3.4: (a) Brillouin zone of chiral TTG for a commensurate case of $(\theta^{12}, \theta^{23}) = (13.2°, 8.61°)$ and $(n, m, n', m') = (1, 2, 1, 1)$. Green, black and orange hexagons represent the first Brillouin zone of graphene layer 1, 2, and 3, respectively. Blue and red hexagons represent the BZ for the moiré patterns given by $l = 1, 2$ and that by $l = 2, 3$, respectively. (b) Magnified plot near $\boldsymbol{K}_+^{(l)}$, where gray hexagons are the BZs of the moiré-of-moiré pattern. (c) The moiré BZ's (blue and red hexagons) aligned at the shared center indicated by a black dot. The moiré-of-moiré BZ (a gray hexagon) is identified by drawing a hexagon with its side connecting the nearest corner points of the moire BZ's.

surate case of $(\theta^{12}, \theta^{23}) = (13.2°, 8.61°)$ and $(n, m, n', m') = (1, 2, 1, 1)$ in Fig. 3.4.

Here green, black and orange hexagons represent the first BZ of layer 1, 2, and 3, respectively. Blue and red hexagons represent the BZ for the first moiré patterns given by $l = 1, 2$ and the second pattern given by $l = 2, 3$, respectively. Finally, the gray hexagon in Fig. 3.4(b) is the BZ of the moiré-of-moiré pattern. It is identified by aligning the moire BZ's (blue and red hexagons) at the shared center as in Fig. 3.4(c), and drawing a hexagon with its side connecting the nearest corner points of the two moire BZ's. This procedure is analogous to deriving the moire BZ from the two graphene's BZs. In the commensurate setting, the moiré-of-moiré BZ can be consistently tiled over the whole graphene's BZ. We label the corner points of the moiré-of-moiré BZ by κ and κ', the midpoint of a side by μ and the center by γ as in Fig. 3.4(b).

3.1.3 Continuum method for multi-scale lattice relaxation

We adopt a continuum approximation [37, 129, 43] to describe the lattice relaxation on TTG. Let $\boldsymbol{s}^{(l)}(\boldsymbol{R}_X)$ be the displacement vector of sublattice $X = A$, or B at a two-dimensional position $\boldsymbol{R}_X$ of layer $l = 1, 2, 3$. Here we consider a long-rage

lattice relaxation which has much longer scales than graphene's lattice constant. The displacement vectors can then be expressed by continuous functions in real space as $s^{(l)}(R_A) = s^{(l)}(R_B) = s^{(l)}(r)$. We ignore the out-of-plane component of the displacement vector in this model, as it does not much contribute to the commensurate domain formation. The optimized lattice structure can be obtained by minimizing the total energy $U = U_E + U_B^{12} + U_B^{23}$, where U_E is the elastic energy and $U_B^{ll'}$ is the interlayer binding energy between layers l and l'. We assume that U_B^{12} and U_B^{23} are given by the interlayer interaction energy of the twisted bilayer graphene [37], and neglect a remote interaction between layer 1 and 3. The U_E and $U_B^{ll'}$ can be expressed as functionals of the displacement field $s^{(l)}(r)$. We solve the Euler-Lagrange equation to obtain the optimized $s^{(l)}(r)$ self-consistently.

The elastic energy of strained TTG is written in a standard form [103, 126] as

$$
\begin{aligned}
U_E = \sum_{l=1}^{3} \frac{1}{2} \int & \left[(\mu + \lambda) \left(s_{xx}^{(l)} + s_{yy}^{(l)} \right)^2 \right. \\
& \left. + \mu \left\{ \left(s_{xx}^{(l)} - s_{yy}^{(l)} \right)^2 + 4 \left(s_{xy}^{(l)} \right)^2 \right\} \right] d^2 r,
\end{aligned}
\tag{3.6}
$$

similar to Eq. 2.12 in TBG. The interlayer binding energy of adjacent layers $(l, l') = (1, 2), (2, 3)$ is given by [37]

$$
U_B^{ll'} = \int d^2 r \sum_{j=1}^{3} 2 V_0 \cos \left[G_j^{ll'} \cdot r + b_j \cdot \left(s^{(l')} - s^{(l)} \right) \right],
\tag{3.7}
$$

where $G_3^{ll'} = -G_1^{ll'} - G_2^{ll'}$. We take $V_0 = 0.160$ eV/nm^2[28, 97].

We introduce

$$
w = s^{(1)} + s^{(2)} + s^{(3)}
$$

$$
u = s^{(1)} - 2 s^{(2)} + s^{(3)}
$$

$$
v = s^{(1)} - s^{(3)},
\tag{3.8}
$$

and rewrite U as a functional of $\boldsymbol{w}, \boldsymbol{u}$ and $\boldsymbol{v}$. Here $\boldsymbol{w}$ represents an overall translation of three layers, while $\boldsymbol{u}$ and $\boldsymbol{v}$ are relative slidings which are mirror-even and odd, respectively, with respect to the middle layer. In the subsequent analysis, we fix $\boldsymbol{w}$ to zero and focus solely on $\boldsymbol{u}$ and $\boldsymbol{v}$, as $\boldsymbol{w}$ does not alter the interlayer registration and therefore does not impact the formation of moiré domains. The Euler-Lagrange equation is written as

$$
\hat{K}\boldsymbol{u} + 6V_0 \sum_{j=1}^{3} \left\{ \sin\left[\boldsymbol{G}_j^{12} \cdot \boldsymbol{r} - \boldsymbol{b}_j \cdot (\boldsymbol{u} + \boldsymbol{v})/2\right] \right.
$$

$$
\left. + \sin\left[\boldsymbol{G}_j^{23} \cdot \boldsymbol{r} + \boldsymbol{b}_j \cdot (\boldsymbol{u} - \boldsymbol{v})/2\right] \right\} \boldsymbol{b}_j = 0 \tag{3.9}
$$

$$
\hat{K}\boldsymbol{v} + 2V_0 \sum_{j=1}^{3} \left\{ \sin\left[\boldsymbol{G}_j^{12} \cdot \boldsymbol{r} - \boldsymbol{b}_j \cdot (\boldsymbol{u} + \boldsymbol{v})/2\right] \right.
$$

$$
\left. - \sin\left[\boldsymbol{G}_j^{23} \cdot \boldsymbol{r} + \boldsymbol{b}_j \cdot (\boldsymbol{u} - \boldsymbol{v})/2\right] \right\} \boldsymbol{b}_j = 0, \tag{3.10}
$$

where

$$
\hat{K} = \begin{pmatrix} (\lambda + 2\mu)\,\partial_x^2 + \mu\partial_y^2 & (\lambda + \mu)\,\partial_x\partial_y \\ (\lambda + \mu)\,\partial_x\partial_y & (\lambda + 2\mu)\,\partial_y^2 + \mu\partial_x^2 \end{pmatrix}. \tag{3.11}
$$

We assume $\boldsymbol{s}^{(l)}$'s (so $\boldsymbol{u}$ and $\boldsymbol{v}$) are periodic in the original moiré-of-moiré period, and define the Fourier components as

$$
\boldsymbol{u}(\boldsymbol{r}) = \sum_{\boldsymbol{G}} \boldsymbol{u}_{\boldsymbol{G}} e^{i\boldsymbol{G}\cdot\boldsymbol{r}}, \quad \boldsymbol{v}(\boldsymbol{r}) = \sum_{\boldsymbol{G}} \boldsymbol{v}_{\boldsymbol{G}} e^{i\boldsymbol{G}\cdot\boldsymbol{r}}, \tag{3.12}
$$

where $\boldsymbol{G} = m_1\boldsymbol{G}_1 + m_2\boldsymbol{G}_2$ are the moiré-of-moiré reciprocal lattice vectors. We also introduce $f_{\boldsymbol{G},j}^{ll'}$ by

$$
\sin\left[\boldsymbol{G}_j^{12} \cdot \boldsymbol{r} - \boldsymbol{b}_j \cdot (\boldsymbol{u} + \boldsymbol{v})/2\right] = \sum_{\boldsymbol{G}} f_{\boldsymbol{G},j}^{12} e^{i\boldsymbol{G}\cdot\boldsymbol{r}},
$$

$$
\sin\left[\boldsymbol{G}_j^{23} \cdot \boldsymbol{r} + \boldsymbol{b}_j \cdot (\boldsymbol{u} - \boldsymbol{v})/2\right] = \sum_{\boldsymbol{G}} f_{\boldsymbol{G},j}^{23} e^{i\boldsymbol{G}\cdot\boldsymbol{r}}. \tag{3.13}
$$

Eq. (3.9) is then written as

$$\boldsymbol{u_G} = -6V_0 \sum_{j=1}^{3} \left(f_{\boldsymbol{G},j}^{12} + f_{\boldsymbol{G},j}^{23} \right) \hat{K}_{\boldsymbol{G}}^{-1} \boldsymbol{b}_j,$$

$$\boldsymbol{v_G} = -2V_0 \sum_{j=1}^{3} \left(f_{\boldsymbol{G},j}^{12} - f_{\boldsymbol{G},j}^{23} \right) \hat{K}_{\boldsymbol{G}}^{-1} \boldsymbol{b}_j, \qquad (3.14)$$

where $\hat{K}_{\boldsymbol{G}}$ is defined by Eq. 2.22.

We obtain the optimized $\boldsymbol{u_G}$ and $\boldsymbol{v_G}$ by solving Eqs. (3.13) and (3.14) in an iterative manner. In the calculation, we only consider a finite number of the Fourier components in $|\boldsymbol{G}| < 3 \max (|n|, |m|, |n'|, |m'|)$, which are sufficient to describe the lattice relaxation in the systems considered. For the case of C2, this cutoff gives 231 Fourier components of wave vector. It should be noted that the components of $\boldsymbol{G} = 0$ cannot be determined by this scheme, since $\hat{K}_{\boldsymbol{G}}$ becomes 0 in Eq. (3.14). Here we treat $\boldsymbol{s}_{\boldsymbol{G}=0}^{(l)}$ as parameters, and perform the above iteration for different parameter choices. We finally choose the solution having the lowest total energy. The dependence on $\boldsymbol{G} = 0$ component arises because the moiré-of-moiré structure depends on a relative translation of the two moiré patterns, and hence it cannot be eliminated by a shift of the origin unlike twisted bilayer graphene. Practically, it is sufficient to consider only the lateral sliding of layer 3 with other two layers fixed.

3.1.4 Continuum Hamiltonian with lattice relaxation

We compute the band structure of the TTGs by using an electronic continuum model [130, 1, 131, 132, 125, 56] that incorporates lattice relaxation [42]. The effective Hamiltonian for valley ξ is written as

$$H^{(\xi)} = \begin{pmatrix} H_1 (\boldsymbol{k}) & U_{21}^{\dagger} & \\ U_{21} & H_2 (\boldsymbol{k}) & U_{32}^{\dagger} \\ & U_{32} & H_3 (\boldsymbol{k}), \end{pmatrix}. \qquad (3.15)$$

The matrix works on a six-component wave function $(\psi_A^{(1)}, \psi_B^{(1)}, \psi_A^{(2)}, \psi_B^{(2)}, \psi_A^{(3)}, \psi_B^{(3)})$, where $\psi_X^{(l)}$ represents the envelope function of sublattice $X(= A, B)$ on layer $l(= 1, 2, 3)$. The $H_l(\boldsymbol{k})$ is the 2×2 Hamiltonian of monolayer graphene and $U_{ll'}$ is the interlayer coupling matrix, in the presence of the lattice distortion. The $H_l(\boldsymbol{k})$ is Dirac Hamiltonian of distorted graphene [Eq. (2.50)] given by

$$H_l(\boldsymbol{k}) = -\hbar v \left[R\left(\theta^{(l)}\right)^{-1} \left(\boldsymbol{k} - \boldsymbol{K}_\xi^{(l)} + \frac{e}{\hbar}\boldsymbol{A}^{(l)}\right)\right] \cdot \boldsymbol{\sigma}, \qquad (3.16)$$

where v is the graphene's band velocity, $\boldsymbol{\sigma} = (\xi\sigma_x, \sigma_y)$ and σ_x, σ_y are the Pauli matrices in the sublattice space (A, B). We change the notation for simplicity. We take $\hbar v/a = 2.14$ eV [57]. The $\boldsymbol{A}^{(l)}$ is the strain-induced vector potential that is given by Eq. (2.51).

By following Eq. (2.85), [the interlayer coupling matrix U_{21} and U_{32} are given by

$$U_{l'l} = \sum_{j=1}^{3} U_j e^{i\delta\boldsymbol{k}_j^{(ll')}\cdot\boldsymbol{r}+i\boldsymbol{Q}_j\cdot\left(\boldsymbol{s}^{(l')}-\boldsymbol{s}^{(l)}\right)} \qquad (3.17)$$

where we defined

$$\delta\boldsymbol{k}_1^{ll'} = 0, \quad \delta\boldsymbol{k}_2^{ll'} = \xi\boldsymbol{G}_1^{ll'}, \quad \delta\boldsymbol{k}_3^{ll'} = \xi\left(\boldsymbol{G}_1^{ll'} + \boldsymbol{G}_2^{ll'}\right), \qquad (3.18)$$

$$\boldsymbol{Q}_1 = \boldsymbol{K}_\xi, \quad \boldsymbol{Q}_2 = \boldsymbol{K}_\xi + \xi\boldsymbol{b}_1, \quad \boldsymbol{Q}_3 = \boldsymbol{K}_\xi + \xi\left(\boldsymbol{b}_1 + \boldsymbol{b}_2\right), \qquad (3.19)$$

and

$$U_1 = \begin{pmatrix} u & u' \\ u' & u \end{pmatrix}, \quad U_2 = \begin{pmatrix} u & u'\omega^{-\xi} \\ u'\omega^{+\xi} & u \end{pmatrix},$$
$$U_3 = \begin{pmatrix} u & u'\omega^{+\xi} \\ u'\omega^{-\xi} & u \end{pmatrix}. \qquad (3.20)$$

The parameters $u = 79.7$ meV and $u' = 95.7$ meV are interlayer coupling strength between AA/BB and AB/BA stack region, respectively. The difference be-

tween u and u' effectively arise from the in-plane lattice relaxation and from the out-of-plane corrugation effect [57, 42]. We assume that the lattice relaxation of z-direction occurs on the moiré scale, and it's similar to TBG. In the band calculation, we take Fourier components within the radius of $|\boldsymbol{G}| \leq 2\max(|n|,|m|,|n'|,|m'|)$ as the basis of Hamiltonian. For C2 case, this cutoff gives the 12642×12642 Hamiltonian. We neglect remote interlayer hoppings between layer 1 and 3.

3.2 Chiral TTGs

3.2.1 Multi-scale lattice relaxation

We study the lattice relaxation in the TTGs of C1$(1.79°, 1.58°)$, C2$(2.64°, 2.45°)$ and C3$(1.54°, 0.64°)$ by using the method described in Sec. 3.1.3. Figure 3.5 summarizes the optimized moiré structures for the three systems. In each row, the left panel shows the moiré pattern 12 (given by layer 1 and 2), and the middle panel shows moiré pattern 23 (by layer 2 and 3) after the relaxation. Here the color represents the local interlayer binding energy $U_B^{ll'}$, where bright and dark regions correspond to the AA stack and AB/BA stack respectively. Tiny magenta dots indicate the original AA stack points without lattice relaxation for reference. In the right-most panel, we overlap the two moiré structures in a single diagram, where blue and red points represent the AA stack of the moiré 12 and 23 respectively. A rhombus in each panel represents the moiré-of-moiré unit cell, and all scale bars indicate 20 nm.

We first consider C1 and C2 which have relatively close twist angles $(\theta^{12}, \theta^{23})$. In the rightmost panels of Fig. 3.5 (a) and (b), we see that locally-commensurate $\alpha\beta$ and $\beta\alpha$ domains (indicated by triangles) are formed. In these domains, the lattice relaxation equalizes the two moiré periods which were initially different, to achieve a commensurate structure. The formation of locally-commensurate domains is more clearly seen in Fig. 3.6, which plots the distribution of the total
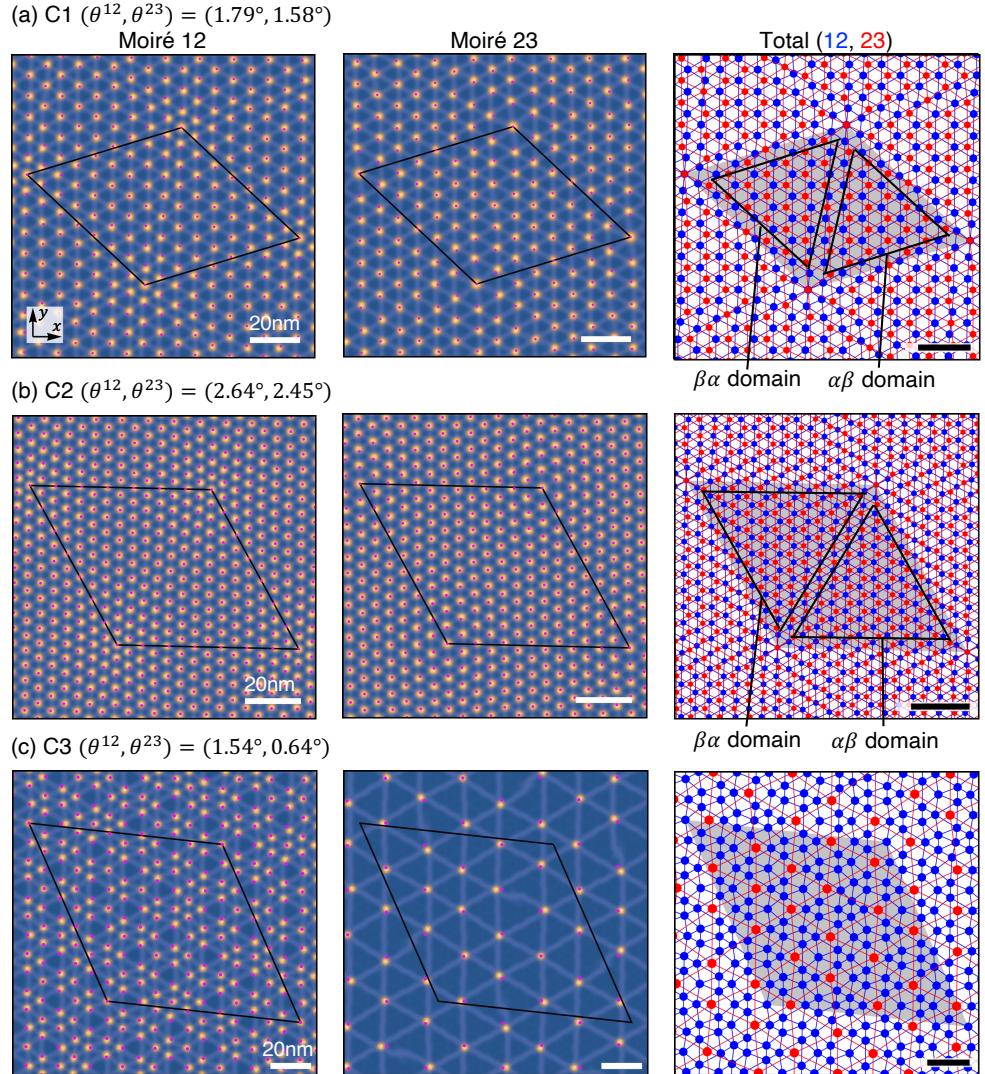
Figure 3.5: Relaxed moiré patterns in chiral TTGs, (a) C1 $(\theta^{12}, \theta^{23})$ = $(1.79°, 1.58°)$, (b) C2 $(2.64°, 2.45°)$ and (c) C3 $(1.54°, 0.64°)$. In the each row, the left and middle panels are the moiré 12 (between layer 1 and 2) and moiré 23 (between layer 2 and 3) patterns after the relaxation. The color corresponds the local interlayer binding energy $U_B^{ll'}$, where bright and dark regions correspond to the AA stack and AB/BA stack respectively. Small magenta dots indicate the AA stack points without lattice relaxation for the reference. The right panel combines the two moiré patterns in a single plot, where blue and red points indicate the AA stack of the moiré 12 and 23 respectively. Black triangles represent $\alpha\beta/\beta\alpha$ domains. A rhombus in each panel shows the moiré-of-moiré unit cell and all scale bars indicate 20 nm.

59

C2 $(\theta^{12}, \theta^{23}) = (2.64°, 2.45°)$

Non-relaxed   Relaxed

$\beta\alpha$

$\alpha\alpha$ $\alpha\beta$

20nm
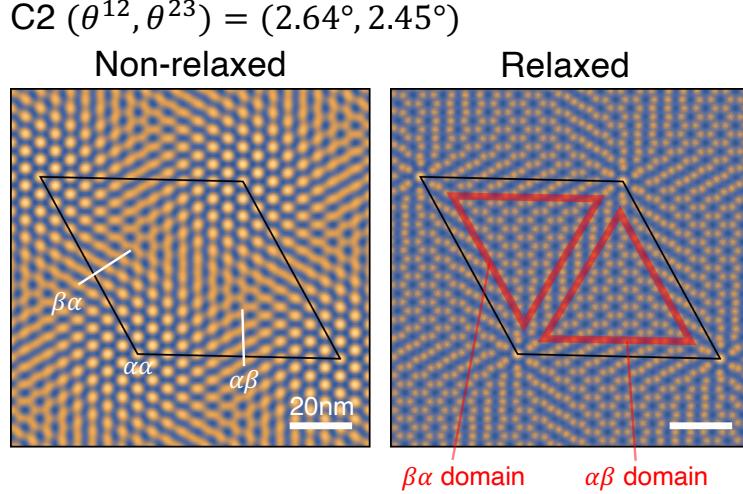
$\beta\alpha$ domain $\alpha\beta$ domain

Figure 3.6: Density plot of the total interlayer binding energy $U_B^{12} + U_B^{23}$ in non-relaxed (left) and relaxed (right) TTG of C2. The black rhombus indicates the moiré-of-moiré unit cell, and the red triangles in right panel indicate emergent $\alpha\beta/\beta\alpha$ domains.

interlayer binding energy $U_B^{12} + U_B^{23}$ in non-relaxed (left) and relaxed (right) cases.

At the same time, we also have the lattice relaxation in a smaller scale as in twisted bilayer graphene, which shrinks AA regions and expands AB/BA regions in each of two moiré patterns. Therefore we have the relaxations in the moiré-of-moiré scale ($\alpha\beta/\beta\alpha$ domains) and in moiré scale (AB/BA domains) at the same time. The following questions naturally arise: (i) What distribution of displacement vectors lead to the multi-scale lattice relaxation? and (ii) Why does such a structure exhibit energetic preference? These questions can be answered by examining the obtained lattice displacement as follows.

Figure 3.7(a) shows the distribution of the displacement vector $\mathbf{s}^{(l)}(\mathbf{r})$ on layer 1, 2 and 3 for the case of C1. The middle row, Fig. 3.7(b), plots a coarse-grained component $\bar{\mathbf{s}}^{(l)}(\mathbf{r})$, which is calculated by averaging $\mathbf{s}^{(l)}(\mathbf{r})$ over a scale of moiré unit cell around the point $\mathbf{r}$. The bottom row [Fig.3.7(c)] displays magnified plots of $\mathbf{s}^{(l)}(\mathbf{r}) - \bar{\mathbf{s}}^{(l)}(\mathbf{r})$ (i.e., the local component with the coarse-grained part subtracted) within the region enclosed by a dashed square in Fig.3.7(a).

In Fig. 3.7(b), we clearly see that $\bar{\mathbf{s}}^{(1)}$ and $\bar{\mathbf{s}}^{(3)}$ rotate counter-clockwise around the center of the $\alpha\beta$ and $\beta\alpha$ domains, while $\bar{\mathbf{s}}^{(2)}$ rotates in the clockwise direc-
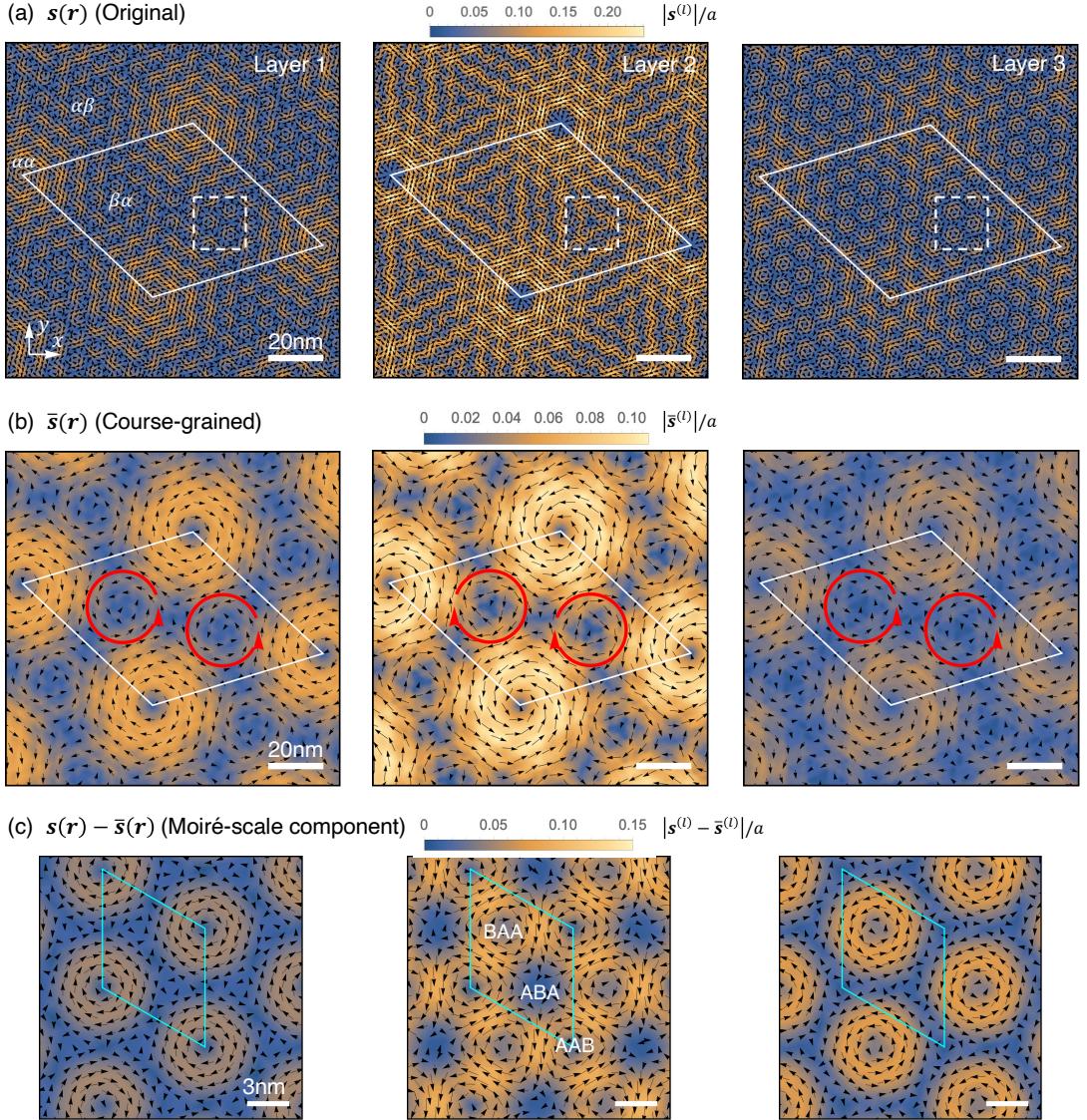
Figure 3.7: Distribution of the displacement vector in each layer of C1:$(\theta^{12}, \theta^{23}) = (1.79°, 1.58°)$. (a) Original non-averaged distribution $\boldsymbol{s}^{(l)}(\boldsymbol{r})(l = 1, 2, 3)$. (b) Coarse-grained component $\bar{\boldsymbol{s}}^{(l)}(\boldsymbol{r})$. (c) Moiré-scale component $\boldsymbol{s}^{(l)}(\boldsymbol{r}) - \bar{\boldsymbol{s}}^{(l)}(\boldsymbol{r})$ in a region indicated by the white square in the top panel. Black arrows represent the displacement vector, and color indicates its norm. Red arc arrows schematically show the direction of rotation in moiré-of-moiré scale. In (a) and (b), the white rhombus represents a moiré-of-moiré unit cell, while in (c) the blue rhombus represents a moiré unit cell.
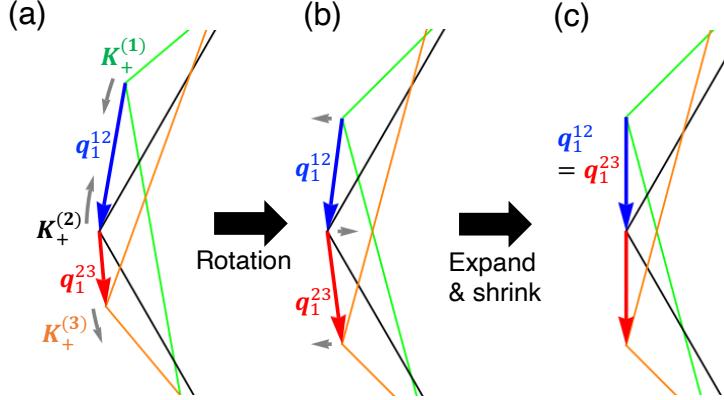
Figure 3.8: Relocation of BZ corners in the C1 system under the lattice relaxation. The panels depict: (a) the original non-distorted configuration, (b) the configuration with rotation included, and (c) with expansion and shrinkage taken into account. Green, black and orange line are the BZ of layer 1, 2 and 3, and gray arrows indicate the direction of rotation and expansion/shrink.

tion. This behavior is closely linked to $\alpha\beta/\beta\alpha$ domain formation, and it can be comprehended by examining the problem in the k-space. Figure 3.7 depicts the relocation of BZ corners of layer 1, 2 and 3 in the C1 system under the lattice relaxation. The panel (a) is for the original non-distorted configuration. We define $\boldsymbol{q}_1^{12} = \boldsymbol{K}_+^{(2)} - \boldsymbol{K}_+^{(1)}$ and $\boldsymbol{q}_1^{23} = \boldsymbol{K}_+^{(3)} - \boldsymbol{K}_+^{(2)}$, where $\boldsymbol{K}_+^{(l)}$ is the BZ corner of layer l near $\xi = +$ valley. The vectors $\boldsymbol{q}_1^{12}$ and $\boldsymbol{q}_1^{23}$ are associated with the periods of the moiré pattern 12 and that of 23, respectively. When these vectors are equal, two moiré periods completely match.

The lattice displacement in Fig. 3.7(b) works precisely to align the two vectors. In the case of C1, the angle between layer 1 and 2 is larger than the angle between layer 2 and 3 ($\theta^{12} > \theta^{23}$), so the layer 2 rotates clockwise, and the layer 1 and layer 3 rotate counter-clockwise to achieve $\theta^{12} = \theta^{23}$ [Fig. 3.7(b)]. There is still a tiny angle difference between $\boldsymbol{q}_1^{12}$ and $\boldsymbol{q}_1^{23}$. This can be eliminated by slightly expanding BZs layer 1 and 3, and shrinking BZ of layer 2, to finally obtain the perfect matching [Fig. 3.7(c)]. In the real space, this corresponds to a shrink of layer 1 and 3 and an expansion of layer 2. These changes are actually observed in Fig. 3.7(a), where the vector fields rotate around the center of the $\alpha\beta/\beta\alpha$ domain. In the final structure of Fig. 3.7(c), the moiré 12 and the moiré 23

become perfectly commensurate. In terms of the reciprocal lattice vectors of the graphene layers, this situation is described as a singular condition that the reciprocal lattice vectors add up to zero, or $\boldsymbol{b}_i^{(1)} - 2\boldsymbol{b}_i^{(2)} + \boldsymbol{b}_i^{(3)} = 0$ ($i = 1, 2$) [82].

To understand the energetic stability of $\alpha\beta/\beta\alpha$ domains, we examine the local moiré-scale lattice relaxation. Let us first consider the twisted bilayer graphene, which has only a single moiré pattern. There the lattice relaxation takes place such that AB/BA stack region expands and AA stack region shrinks [37]. This is realized by a local interlayer rotation around AA and AB/BA stack points. Around AB/BA, specifically, the layer 1 and 2 oppositely rotate to reduce the local twist angle. The AB/BA region is then enlarged, because the length scale of the moiré pattern is enlarged in decreasing the twist angle. In AA spots, on the contrary, the layer 1 and 2 rotate to increase the local twist angle to shrink the AA region.

The same deformation occurs also in TTG, where all three layers undergo relaxation to expand AB/BA domain in each of the two moiré patterns. However, as the middle layer $l = 2$ is shared by the two interference patterns, there can be a frustration such that, for instance, a local movement of the layer 2 leads to the expansion of the AB region in one moiré pattern while causing its contraction in the other. Therefore, the relative displacement of the two moiré superlattices should be determined in such a way that the middle-layer distortion can lower the total energies of the two moiré patterns at the same time.

Figure 3.9(a) is the schematic figure to illustrate the favorable local rotation of the middle layer, for the moiré 12 (between $l = 1, 2$) and moiré 23 (between $l = 2, 3$). The orange and green arc arrows correspond to clockwise and counter-clockwise directions, respectively. Here we notice that the direction of rotation is opposite for moiré 12 and moiré 23, since layer 1 and layer 3 are originally twisted in opposite directions with respect to layer 2. When AA stack points of moiré 12 and moiré 23 are aligned ($\alpha\alpha$ stacking), the rotation direction of layer 2 is completely frustrated as shown in Fig. 3.9(b), and therefore $\alpha\alpha$ stacking is
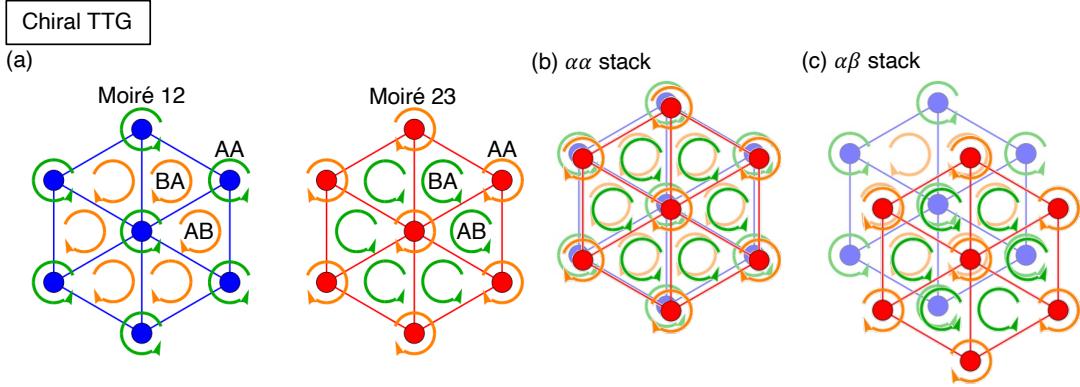
Figure 3.9: (a) Schematic figure of the preferred direction of the middle layer ($l = 2$), for the moiré 12 (between $l = 1, 2$) and moiré 23 (between $l = 2, 3$). Orange and green arc arrows correspond to clockwise and counterclockwise directions, respectively. Bottom row: Overlapped figures for (b) $\alpha\alpha$ stack and (c) $\alpha\beta$ stack.

energetically unfavorable. The optimized structure is $\alpha\beta$ stacking [Fig. 3.9(c)], where the rotation angles coincide in two out of three regions.

The mechanism of the moiré-of-moiré domain formation is summarized as follows. At the moiré scale, the local rotation [Fig. 3.7(c)] leads to a reduction of AA regions and an enlargement of AB regions in the moiré patterns (12 and 23), just as in twisted bilayer graphene. In contrast, a rotation in the moiré-of-moiré scale [Fig. 3.7(b)] adjusts the periodicities of the moiré 12 and 23, achieving local commensurability of the two patterns [Fig. 3.7(b)]. These rotations in the different scales work cooperatively to minimize the total energy. This cooperative mechanism is intuitively explained by the frustration picture in Fig. 3.7, which requires the two moiré patterns to align to avoid a frustration of the rotation direction in the moiré scale.

When the two angles θ^{12} and θ^{23} are not close to each other, $\alpha\beta/\beta\alpha$ domains do not appear any more, but still a locally-commensurate moiré-of-moiré structure emerges. Figure 3.5(c) shows the relaxed structure for the C3 TTG. Since the unit areas of the two moiré patterns differ by nearly 3, we have commensurate domains where a single red triangle includes three blue triangles. We also see red AA points always come to the center of blue triangles. This can also be understood in terms of the alignment of the favorable rotation angles explained
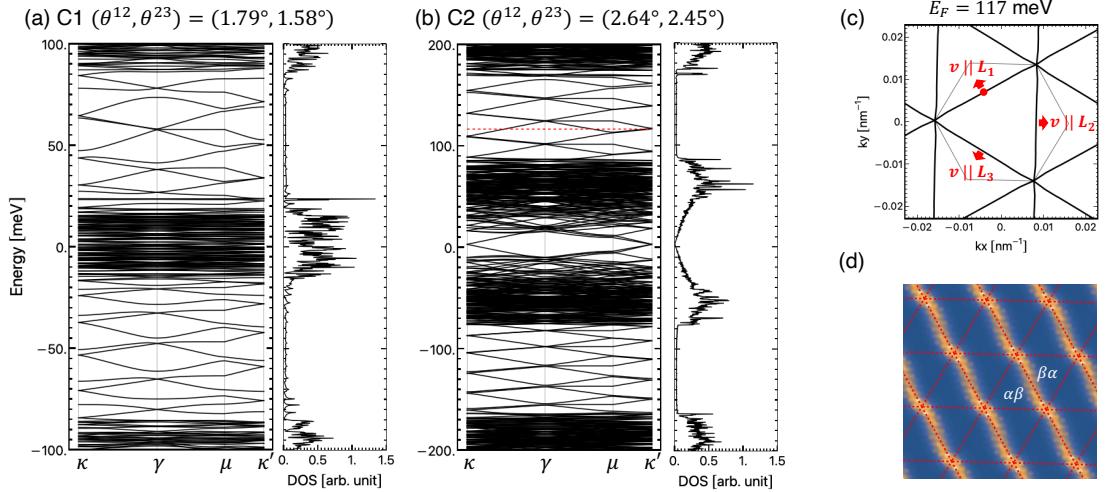
Figure 3.10: (a,b) Electronic band structures and the density of states of K_+-valley calculated for (a) C1 and (b) C2 with the lattice relaxation incorporated. The k-space path ($\kappa - \gamma - \mu - \kappa'$) is defined in Fig. 3.4. (c) Fermi surface of the C2 at $E_F = 117$ meV (indicated by a red dotted horizontal line in (b)). Three red arrows represent the directions of band velocities, which are parallel to the moiré lattice vectors L_1, L_2, and $L_3(= -L_1 + L_2)$. (d) Distribution of the squared wave amplitude of an eigenstate state, indicated by a red point in (c). Red rhombus represents a moiré-of-moiré unit cell.

above.

While our study focuses on commensurate twisted TTGs in this thesis, the domain formation in incommensurate cases can be conjectured by the intuitive picture for the formation of locally-commensurate domains. The calculation of C3 [Fig. 3.5(c)] provides a glimpse into this scenario, where various types of locally-commensurate domains coexist and form a mosaic pattern to fit the original moiré period difference. Since it is a commensurate TTG, the entire domain pattern is also periodic with a unit cell of gray rhombus, as a result of the shared common periodicity between the moiré patterns. In contrast, in incommensurate cases, we anticipate a similar formation of locally-commensurate domains but with a quasi-periodic arrangement.

3.2.2   Electronic properties

Using the electronic continuum model introduced in Sec. 3.1.4, we calculate the

band structure of TTGs in the presence of the lattice relaxation. Figure 3.10(a) and (b) show the energy bands (near K_+ valley) and the corresponding density of states (DOS) calculated for the case C1 and C2, respectively. The labels $\kappa, \gamma, \mu, \kappa'$ are symmetric points of the moiré-of-moiré BZ defined in Fig. 3.4.

We immediately notice that the spectrum exhibits distinct energy windows characterized by relatively low DOS, which span in the energy range of 20 meV $< |E| <$ 90 meV for C1, and in 90 meV $< |E| <$ 180 meV for C2. The windows are sparsely filled with energy bands. Figure 3.10(c) shows the Fermi surface at E_F = 117 meV in the C2, which is indicated by horizontal red line in Fig. 3.10(b). We see that the Fermi surface is composed of three intersecting lines arranged with a trigonal symmetry, indicating the dispersion is nearly one-dimensional. The band velocities of these one-dimensional bands (normal to the Fermi surface) are oriented to the moiré-of-moiré lattice vectors $\boldsymbol{L}_1$, $\boldsymbol{L}_2$ and $\boldsymbol{L}_3 (= -\boldsymbol{L}_1 + \boldsymbol{L}_2)$. Figure 3.10(d) plots the distribution of the squared wave amplitudes of an eigenstate marked by a red point in Fig. 3.10(c). The wave function actually takes a highly one-dimensional form, and it is sharply localized within the domain walls dividing $\alpha\beta$ and $\beta\alpha$ regions. Each of the three Fermi surfaces corresponds to one-dimensional states running along the domain walls in the corresponding directions. The states with different directions are barely hybridized. We also have a low-DOS region near $E = 0$ in the C2, while this is remnant of the graphene's Dirac cone and the energy bands are not one-dimensional.

The existence of one-dimensional channels on the domain walls indicates that the $\alpha\beta$ and $\beta\alpha$ regions are locally gapped with different topological numbers, and associated topological boundary modes emerge between the domains, as shown in Fig. 3.1. To verify this, we calculate the bands structures and the Chern numbers of *uniform* TTG having $\alpha\beta/\beta\alpha$ stacking. The Hamiltonian of such a uniform system can be obtained by assuming the BZ-corner arrangement in Fig. 3.7(c), where $\boldsymbol{q}_1^{12} = \boldsymbol{q}_1^{23} \equiv \boldsymbol{q}$. This corresponds to a TTG where $\theta^{12} = \theta^{23}$ and the layer 2 is slightly expanded in relative to layer 1 and 3. The two moiré periods then

66
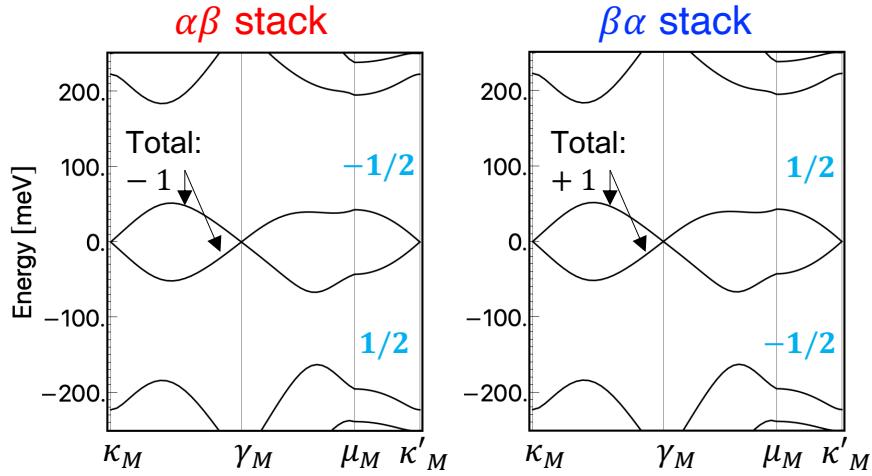
Figure 3.11: Local band structure of the $\alpha\beta$ (left) and $\beta\alpha$ (right) structure with $\theta = 2.54°$. Black and blue numbers indicate the Chern numbers for bands and gaps, respectively. $\kappa_M, \gamma_M, \mu_M, \kappa'_M$ are the labels for the common moiré BZ, where κ_M and κ'_M are corner points, μ_M is the midpoint of a side and γ_M is the center of the BZ.

become identical, and we have $\boldsymbol{G}_j^{12} = \boldsymbol{G}_j^{23} \equiv \boldsymbol{G}_j^{\mathrm{M}}$ and $\boldsymbol{q} = (2\boldsymbol{G}_1^{\mathrm{M}} + \boldsymbol{G}_2^{\mathrm{M}})/3$. The Hamiltonian for this system is obtained from Eq. (3.15) as

$$
H^{(\xi)} = \begin{pmatrix} H(\boldsymbol{k} + \xi\boldsymbol{q}) & U_{21}^\dagger & \\ U_{21} & H(\boldsymbol{k}) & U_{32}^\dagger \\ & U_{32} & H(\boldsymbol{k} - \xi\boldsymbol{q}), \end{pmatrix}. \tag{3.21}
$$

where

$$
H(\boldsymbol{k}) = -\hbar v \boldsymbol{k} \cdot \boldsymbol{\sigma}, \tag{3.22}
$$

$$
U_{21} = \sum_{j=1}^{3} U_j \mathrm{e}^{\mathrm{i}\delta\boldsymbol{k}_j \cdot \boldsymbol{r}}, \quad U_{32} = \sum_{j=1}^{3} U_j \mathrm{e}^{\mathrm{i}\xi\delta\boldsymbol{k}_j \cdot (\boldsymbol{r} - \boldsymbol{r}_0)}
$$

$$
\delta\boldsymbol{k}_1 = \boldsymbol{0}, \quad \delta\boldsymbol{k}_2 = \xi\boldsymbol{G}_1^{\mathrm{M}}, \quad \delta\boldsymbol{k}_3 = \xi\left(\boldsymbol{G}_1^{\mathrm{M}} + \boldsymbol{G}_2^{\mathrm{M}}\right), \tag{3.23}
$$

and we neglect the strain-induced vector potentials which does not affect the topological nature argued here. Here U_{21} and U_{32} differ by the parameter $\boldsymbol{r}_0$, which

specifies the relative displacement between the two moiré patterns. The $\alpha\beta$ and $\beta\alpha$ stackings correspond to $\boldsymbol{r}_0 = \left(\boldsymbol{L}_1^M + \boldsymbol{L}_2^M\right)/3$ and $2\left(\boldsymbol{L}_1^M + \boldsymbol{L}_2^M\right)/3$ respectively, where $\boldsymbol{L}_j^M$ is the common moiré lattice vector given by $\boldsymbol{G}_i^M \cdot \boldsymbol{L}_j^M = 2\pi\delta_{ij}$.

Here we consider uniform $\alpha\beta$ and $\beta\alpha$ TTGs with $\theta^{12} = \theta^{23} = 2.54°$, which approximate the local structures of $\alpha\beta$ and $\beta\alpha$ domains in the C2. Figure 3.11 plots the energy bands in $\xi = +$ valley calculated by Eq. (3.21). We observe energy gaps in the electron and hole sides in the region $50\,\mathrm{meV} < |E| < 180\,\mathrm{meV}$, which approximately coincides with the energy window of the C2 [Fig. 3.10(b)]. Between the gaps in the electron and hole sides, we have two bands touching at the charge neutrality point. The total Chern number for the two-band cluster is found to be ∓1 for $\alpha\beta$ and $\beta\alpha$, respectively. The absolute Chern number in the upper gap can also be calculated, and it turns out to be $\mp1/2$ for $\alpha\beta$ and $\beta\alpha$, respectively. This is obtained by opening mass gap (adding asymmetric energies to A and B sublattices in all the graphene layers) to lift the band touching at the Dirac point. Since the difference of the Chern number of the upper gap between the $\alpha\beta$ and $\beta\alpha$ regions is 1, we have a single edge mode (per a single valley) at the domain boundary. This coincides with the number of the one-dimensional modes per a single direction in the moiré-of-moiré superlattice band Fig. 3.10. The Chern number of the valley $\xi = -1$ is negative of $\xi = +1$ valley due to the time reversal symmetry. Therefore the TTG is a quantized valley Hall insulator when the Fermi energy is in the energy window.

The energy windows and one-dimensional domain-wall states also appear in the C1 case [Fig. 3.10(a)], which has a smaller moiré-of-moiré period. The degree of one-dimensionality is not as pronounced as in the C2 configuration, as evidenced by the appearance of small gaps at the intersections of bands. The hybridization tends to be greater when the moiré-of-moiré period is smaller.

Finally, the band structure in Fig. 3.10 closely resembles the marginally-stacked twisted bilayer graphene in a strong perpendicular electric field [133, 134, 135, 136, 137, 138, 139]. There the topological one-dimensional edge states

arise since the AB and BA regions in the moiré pattern have opposite valley Chern numbers in the electric field. The chiral TTG realizes a similar situation in the moiré-of-moiré scale, without the need for an applied electric field. This can be achieved in any chiral TTGs where θ^{12} and θ^{23} are close to each other, such that the two moiré periods are comparable.

3.3   alternating TTGs

3.3.1   Multi-scale lattice relaxation

Alternating TTGs display distinct relaxed structures that differ entirely from the chiral cases. Figure 3.12 shows optimized moiré structures calculated for alternating TTGs (a) A1 $(\theta^{12}, \theta^{23}) = (1.48°, -1.18°)$, (b) A2 $(1.42°, -1.22°)$ and (c) A3 $(1.47°, -0.62°)$, corresponding to Fig. 3.5 for chiral TTGs. In the A1 and A2, we observe a formation of commensurate $\alpha\alpha'$ domains, where AA spots of the two moiré patterns completely overlaps [See Fig. 3.2(e)]. This is in a sharp contrast to the chiral TTGs, where AA spots are repelled to each other, giving rise to $\alpha\beta/\beta\alpha$ domains. The atomic structure of $\alpha\alpha'$ domain corresponds precisely to the mirror-symmetric TTG with $\theta^{12} = -\theta^{23}$. In A3 case [Fig. 3.12(c)], where the two moiré periods are not comparable, we observe a different type of commensurate domain with the ratio of the lattice periods fixed at 2, reflecting the original moiré-period ratio $L^{23}/L^{12} \simeq 2.3$. Here the AA stacking points of the red and blue moiré lattices are vertically aligned as in $\alpha\alpha'$ domains observed in A1 and A2.

The formation of the commensurate domains can be attributed to a specific type of lattice distortion that differs from the chiral case. Figure 3.13 shows the distribution of the coarse-grained displacement vector $\bar{s}^{(l)}(r)$ in the A1 case (corresponding to Fig. 3.7(b) for the chiral case). We observe that the layer 1 and layer 3 rotate anti-clockwise and clockwise directions, respectively, around $\alpha\alpha'$ domain center. In k-space, accordingly, the Brillouin zone corners of layers

(a) A1 $(\theta^{12}, \theta^{23}) = (1.48°, -1.18°)$

Moiré 12   Moiré 23   Total (12, 23)

20nm

$\alpha\alpha'$ domain

(b) A2 $(\theta^{12}, \theta^{23}) = (1.42°, -1.22°)$

20nm

$\alpha\alpha'$ domain

(c) A3 $(\theta^{12}, \theta^{23}) = (1.47°, -0.62°)$

20nm

2 : 1 domain
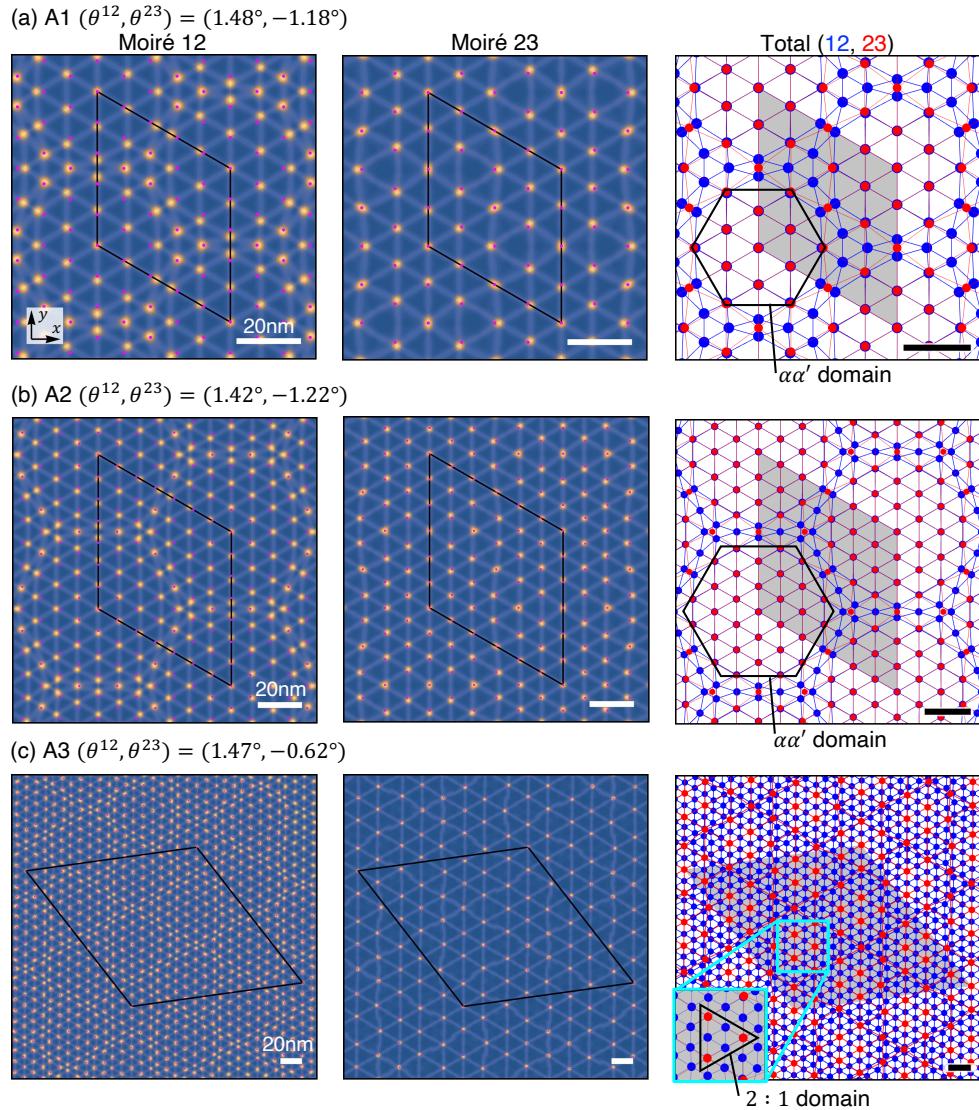
Figure 3.12: Relaxed moiré patterns in alternating TTGs, (a) A1:$(\theta^{12}, \theta^{23})$ = $(1.48°, -1.18°)$, (b) A2: $(1.42°, -1.22°)$ and (c) A3:$(1.47°, -0.62°)$, corresponding to Fig. 3.5 for the chiral TTGs.
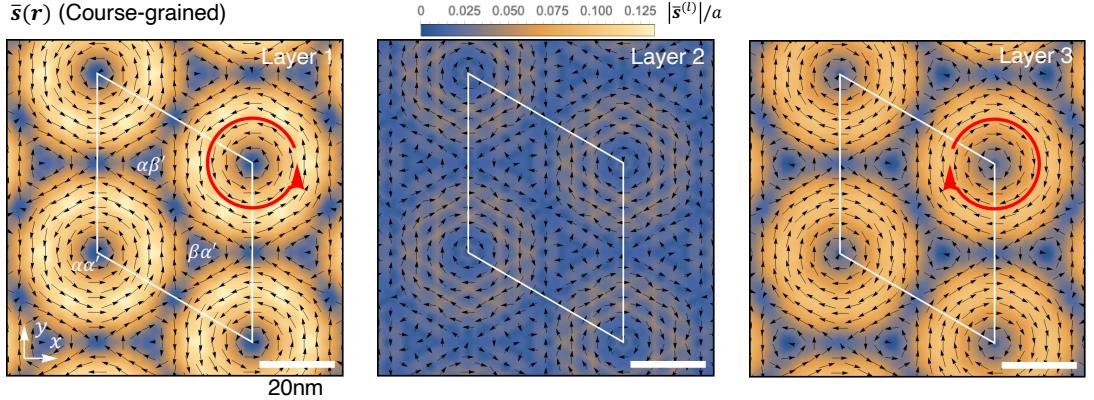
Figure 3.13: Distribution of the coarse-grained displacement vector $\bar{\boldsymbol{s}}^{(l)}(\boldsymbol{r})$ in A1:$(\theta^{12}, \theta^{23}) = (1.48°, -1.18°)$, corresponding to Fig. 3.7(b) for the C1.
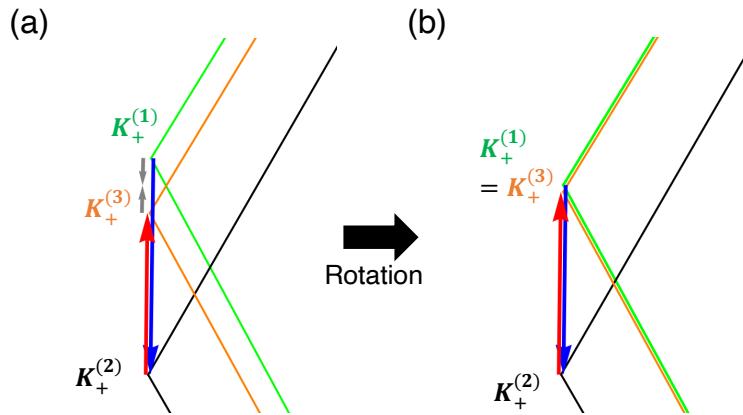

Figure 3.14: Relocation of BZ corners in the A1:$(\theta^{12}, \theta^{23}) = (1.48°, -1.18°)$ under the lattice relaxation. The panels depict (a) the original non-distorted configuration and (b) the relaxed configuration.

1 and 3 move to overlap as shown in Fig. 3.14. This corresponds to the symmetric TTG ($\theta^{12} = -\theta^{23}$) where the layer 1 and layer 3 are perfectly aligned.

The stability of $\alpha\alpha'$-domain is also explained by considering moiré-scale lattice relaxation. As discussed in Sec. 3.2.1, the graphene layers in TTG undergo spontaneous distortion to expand the AB/BA regions for the moiré patterns 12 and 23, giving a competitive environment for the shared layer 2. Figure 3.15(a) depicts the preferred orientation of layer 2 for the two moiré patterns in alternating TTG. In contrast to the chiral stack [Fig. 3.9], the rotation direction is identical for both moiré patterns, since layer 1 and layer 3 are rotated in the same direction relative to the layer 2. Consequently, there is no frustration when
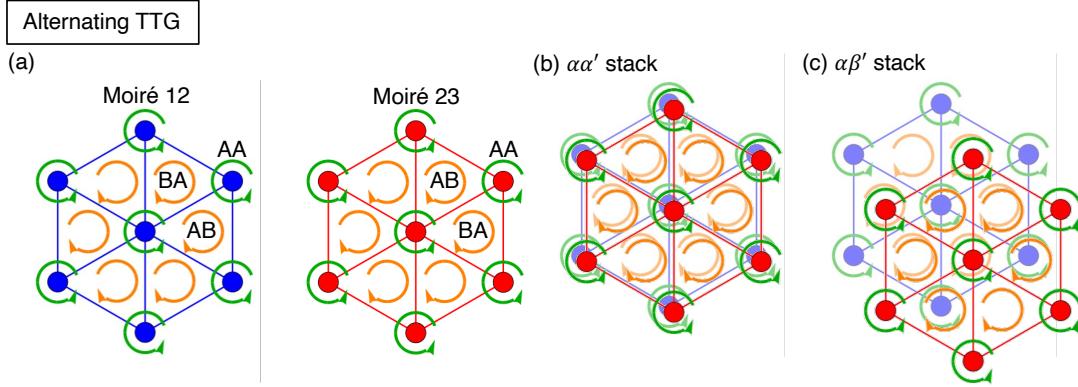
Figure 3.15: (a) Schematic figure of the preferred distorting direction of the middle layer ($l = 2$) in an alternating TTG, corresponding to Fig. 3.9 for a chiral TTG.

the moiré lattices are arranged in an $\alpha\alpha'$ stack as shown in Fig. 3.15(b). In this structure, the motion of the shared layer 2 allows for the simultaneous relaxation of the moiré patterns 12 and 23, resulting in an energy advantage compared to partially frustrated configurations like the $\alpha\beta'$ stack [Fig. 3.15(c)]. The stability of $\alpha\alpha'$ stack in nearly-symmetric TTGs was pointed out in the previous theoretical works [60, 64, 80, 81], and it was observed in recent experiments [25, 26].

3.3.2 Electronic properties

We calculate the band structure for alternating TTGs of A1($1.48°$, $-1.18°$), (b)A2($1.42°$, $-1.22°$) using the method described in Sec. 3.1. The energy band and DOS for A1 and A2 are displayed in Figs. 3.16(a) and (b), respectively. In each figure, the right and left panels correspond to the TTGs with and without the lattice relaxation, respectively. Black curves represent the energy bands, and blue straight lines indicate the intrinsic Dirac bands of layer 1 and layer 3 without the interlayer coupling. Red dots indicate the amplitude projected onto the mirror-odd plane

(a) A1 $(\theta^{12}, \theta^{23}) = (1.48°, -1.18°)$

Non-relaxed

Relaxed

(b) A2 $(\theta^{12}, \theta^{23}) = (1.42°, -1.22°)$

Non-relaxed

Relaxed
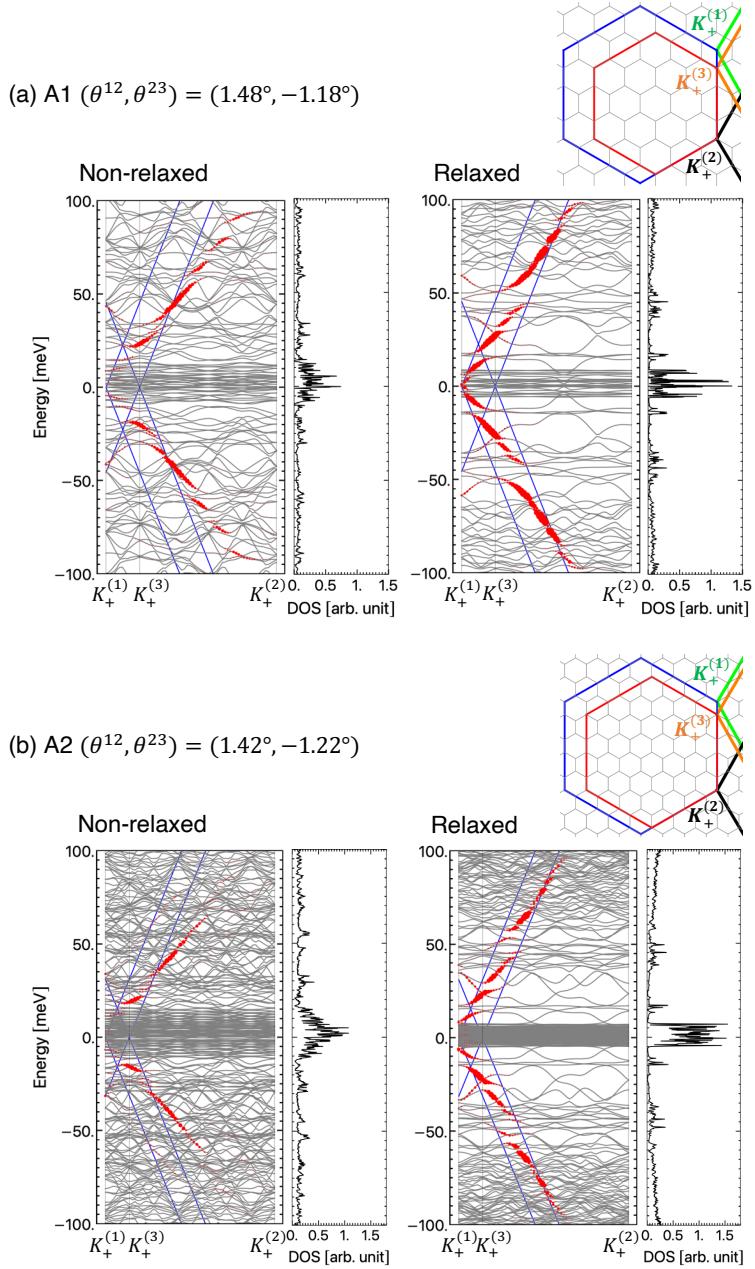
Figure 3.16: Energy bands and DOS for alternating TTGs, (a) A1:$(1.48°, 1.18°)$ and (b) A2:$(1.42°, 1.22°)$. The left and right panels in each figure show the results without and with the lattice relaxation, respectively. Black curves represent the energy bands, and blue straight lines indicate the intrinsic Dirac bands of layer 1 and layer 3 without the interlayer coupling. Red dots indicate the amplitude projected onto the mirror-odd plane wave states (see the text). The path is taken as $\boldsymbol{K}_+^{(1)} \to \boldsymbol{K}_+^{(3)} \to \boldsymbol{K}_+^{(2)}$ in the extended k-space shown in the inset.

wave states, as defined by

$$w_{nk}^{(\text{odd})} = \sum_{X=A,B} |\langle \psi_{nk} | k, X, \text{odd} \rangle|^2,$$

$$|k, X, \text{odd}\rangle = \frac{1}{\sqrt{2}} (|k, X, 1\rangle - |k, X, 3\rangle), \tag{3.24}$$

where ψ_{nk} is the eigenstates, and $|k, X, l\rangle$ is the plane wave at sublattice $X(=A, B)$ on layer l. We take the path $K_+^{(1)} \to K_+^{(3)} \to K_+^{(2)}$ on a straight line in the extended k-space, as shown in insets of Fig. 3.16.

In the band structures with the lattice relaxation, we observe numerous flat bands concentrated around zero energy, and these bands are surrounded by a region where dispersive energy bands are sparsely distributed. These features coincide with the mirror-symmetric TTG ($\theta^{12} = -\theta^{23}$), where the low-energy spectrum is composed of a flat band with even parity, and a Dirac cone with odd parity against the mirror inversion [59, 60]. We see that the red dots roughly form a conical dispersion, and it is regarded as a remnant of the symmetric TTG's Dirac cone having odd parity. In the non-relaxed calculations, we notice that the flat bands and Dirac cones are strongly hybridized, and the conical dispersion of the red dots is not clearly resolved. These results suggest that the formation of $\alpha\alpha'$ domains (equivalent to the mirror-symmetric TTG) supports the spectral separation of the flat bands and the Dirac-cone like bands. Therefore, we expect that asymmetric TTGs slightly away from the symmetric condition $\theta^{12} = -\theta^{23}$ acquire similar electronic properties to the symmetric TTG, through the moiré-of-moiré lattice relaxation.

The electronic properties of TTG can be tuned by applying a perpendicular electric field. We can introduce the field effect to our model as $H + V$, where H is the original Hamiltonian of Eq. (3.15), and V is the on-site potential term by
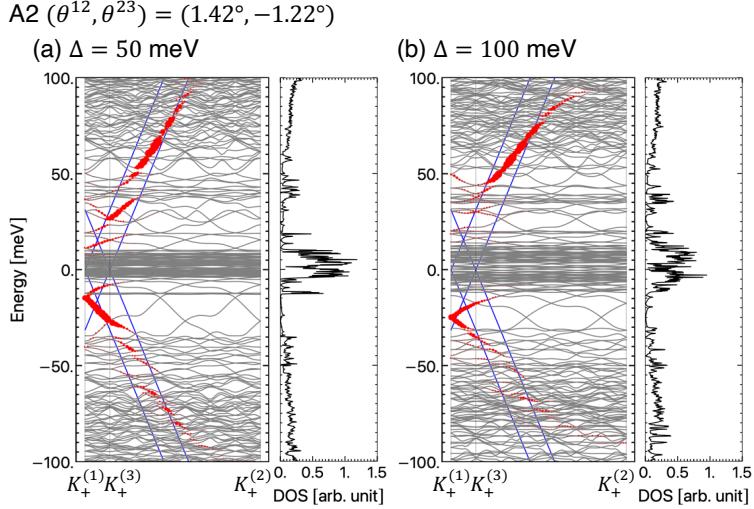
Figure 3.17: Plots similar to Fig. 3.7 for A2:$(1.43°, -1.28°)$ with the perpendicular electric field of (a) $\Delta = 50$ meV and (b) 100 meV.

perpendicular electronic field,

$$
V = \begin{pmatrix} -\Delta \hat{I}_2 & & \\ & 0 & \\ & & \Delta \hat{I}_2 \end{pmatrix}. \tag{3.25}
$$

Here Δ is the difference of the on-site energy and $\hat{I}_2$ is a 2×2 unit matrix, and we simply assumed the perpendicular electric field is constant between top layer and bottom layer. Figure 3.17 shows the energy band of the A2 with lattice relaxation, under the perpendicular electric field $\Delta = 50$ meV and 100 meV. When the electric field is applied, we observe the Dirac band moves along the energy axes, and eventually the Dirac point emerges out of the flat-band cluster. We also see that the electric fields broaden the energy width of the flat band region, and enhances a hybridization between the flat bands and the dispersive bands.

Chapter 4

Moiré disorder effect in twisted bi-layer graphene

In this Chapter, we study the electronic structure of magic-angle twisted bilayer graphene (TBG) with disordered moiré patterns. We first consider a uniform distortion case, and show that the the flat band is hardly broadened, but splits into upper and lower subbands in most places. This splitting energy is almost determined by the value of the effective vector potential induced by hoterostrain, whereas the variation of twist angle give relatively minor effects on the electronic structure. We explain the almost exclusive dependence on the vector potential by a pseudo Landau level picture for the magic-angle flat band, and we obtain an analytic expression of the splitting energy as a function of the strain amplitude. Second, we expand above to non-uniform distortion case. We show that the local density of states of the flat band also splits along the energy axis, and the spatial dependence of the splitting energy depends on the local value of the effective vector potential induced by heterostrain.

4.1   TBG with a uniform distortion

4.1.1   Atomic structure

We first consider a TBG with a uniform lattice distortion and investigate its effect on the flat band.
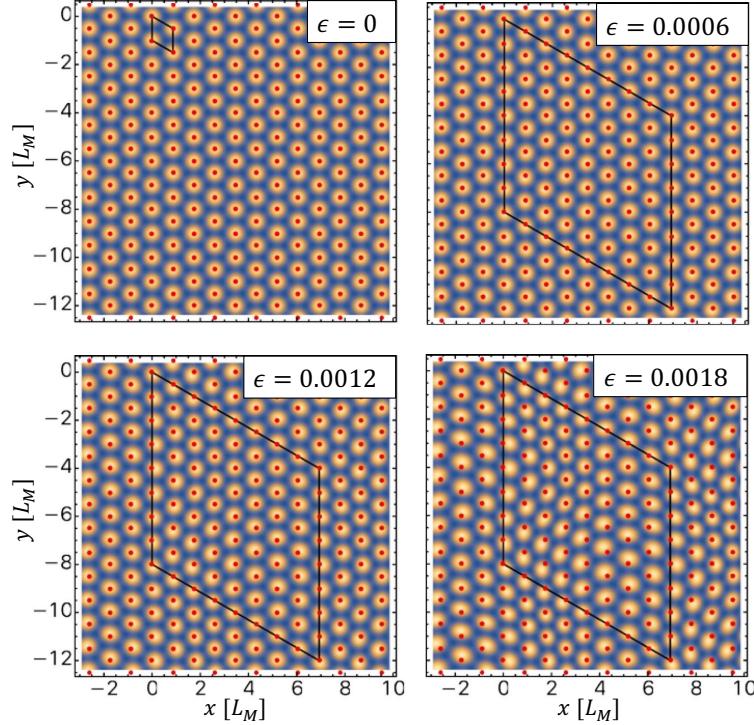
Figure 4.1: Moiré patterns of magic-angle TBG ($\theta = 1.05°$) with random non-uniform distortion of $\epsilon = 0$, 0.0006, 0.0012 and 0.0018, where the characteristic wave length is $\lambda = 7L_M$, and the super-cell size (big parallelogram) is $n_{\mathrm{SM}} = 8$. The bright region represents local AA stack and the dark region represents AB/BA stack. The red dots are the AA spots of the non-distorted TBG for reference.

We introduce a uniform distortion to layer l, which is expressed by a matrix,

$$\mathcal{E}^{(l)} = \begin{pmatrix} \epsilon_{xx}^{(l)} & -\Omega^{(l)} + \epsilon_{xy}^{(l)} \\ \Omega^{(l)} + \epsilon_{xy}^{(l)} & \epsilon_{yy}^{(l)} \end{pmatrix}. \tag{4.1}$$

The $\mathcal{E}^{(l)}$ represents a deformation such that a carbon atom at a position r in a non-distorted system is shifted to $r + \mathcal{E}^{(l)}r$. Here $\epsilon_{xx}^{(l)}$ and $\epsilon_{yy}^{(l)}$ represent normal strains in x and y directions, respectively, $\epsilon_{xy}^{(l)}$ is a shear strain, and $\Omega^{(l)}$ is a rotation from the original twist angle. For later arguments, we also define the isotropic/anisotropic components of the normal strain by

$$\epsilon_{\pm}^{(l)} = \frac{1}{2}(\epsilon_{xx}^{(l)} \pm \epsilon_{yy}^{(l)}), \tag{4.2}$$

77

and the interlayer difference of each strain/rotation component as

$$\epsilon_\pm = \epsilon_\pm^{(1)} - \epsilon_\pm^{(2)},$$

$$\epsilon_{xy} = \epsilon_{xy}^{(1)} - \epsilon_{xy}^{(2)},$$

$$\Omega = \Omega^{(1)} - \Omega^{(2)}. \tag{4.3}$$

In the presence of distortion, the lattice vectors change to $\boldsymbol{a}_j^{(l)} = (1+\mathcal{E}^{(l)})R(\mp\theta/2)\boldsymbol{a}_j$. In the following, we assume the original twist angle and the distortion is sufficiently small $(\theta, \Omega^{(l)}, \epsilon_{\mu\nu}^{(l)} \ll 1)$, so that

$$\boldsymbol{a}_j^{(l)} \approx \left[R\left(\mp\theta/2\right) + \mathcal{E}^{(l)}\right]\boldsymbol{a}_j. \tag{4.4}$$

Similarly, the reciprocal lattice vectors are written as

$$\boldsymbol{b}_j^{(l)} \approx \left[R\left(\mp\theta/2\right) - \mathcal{E}^{(l)\mathrm{T}}\right]\boldsymbol{b}_j, \tag{4.5}$$

where $\boldsymbol{T}$ is the matrix transpose.

In an intrinsic monolayer graphene, six corner points of the Brillouin zone (BZ) are given by $\xi\boldsymbol{K}_j$ ($j = 1, 2, 3$), where $\xi = \pm 1$ label the valley degree of freedom, and

$$\boldsymbol{K}_j = R\left(\phi_j\right)\frac{4\pi}{3a}(-1, 0), \quad \phi_j = \frac{2\pi}{3}(j - 1), \tag{4.6}$$

are equivalent points in the BZ. Corresponding vectors for the distorted TBG are written as

$$\boldsymbol{K}_j^{(l)} \approx \left[R\left(\mp\theta/2\right) - \mathcal{E}^{(l)\mathrm{T}}\right]\boldsymbol{K}_j. \tag{4.7}$$

Figure 4.2 illustrates the schematics of BZ for (a) a non-distorted TBG and (b) a distorted TBG. In each panel, blue and orange hexagons on the left represent the first BZ of graphene layer $l = 1$ and 2, respectively, where the corner points

78

are given by $\xi \boldsymbol{K}_j^{(l)}$. We define interlayer shift of the corner points by

$$\boldsymbol{q}_j = \boldsymbol{K}_j^{(1)} - \boldsymbol{K}_j^{(2)} \quad (j = 1, 2, 3), \tag{4.8}$$

as shown in Fig. 4.2. The $\boldsymbol{q}_j$'s can be expressed only by the interlayer rotation and strain components as

$$\boldsymbol{q}_j = \frac{4\pi}{3a} \left[R\left(\phi_j\right) \begin{pmatrix} \epsilon_+ \\ \theta - \Omega \end{pmatrix} + R\left(-\phi_j\right) \begin{pmatrix} \epsilon_- \\ \epsilon_{xy} \end{pmatrix} \right]. \tag{4.9}$$

The reciprocal lattice vectors of the moiré pattern are given by $\boldsymbol{G}_j^M = \boldsymbol{b}_j^{(1)} - \boldsymbol{b}_j^{(2)}$, which are also written as $\boldsymbol{G}_1^{\mathrm{M}} = \boldsymbol{q}_2 - \boldsymbol{q}_1$, $\boldsymbol{G}_2^{\mathrm{M}} = \boldsymbol{q}_3 - \boldsymbol{q}_2$. In Fig. 4.2, a green hexagon on the right side represents the moiré Brillouin zone defined by $\boldsymbol{G}_j^{\mathrm{M}}$'s.

4.1.2 Continuum model and Band calculation

We use the continuum model[1, 41, 42, 56, 57, 101, 125, 132, 140, 141, 142, 143, 144, 145, 146, 147, 148, 149, 150, 151, 152, 153, 154, 155, 156] to describe a strained TBG. The effective Hamiltonian for valley ξ is written as

$$\mathcal{H}^{(\xi)}(\boldsymbol{k}) = \begin{pmatrix} H_1(\boldsymbol{k}) & U^\dagger \\ U & H_2(\boldsymbol{k}) \end{pmatrix}, \tag{4.10}$$

where $H_l(\boldsymbol{k})$ is the 2×2 Hamiltonian of distorted monolayer graphene, and U is the interlayer coupling matrix. The Hamiltonian[Eq. (4.10)] works on the four-component wave function $(\psi_A^{(1)}, \psi_B^{(1)}, \psi_A^{(2)}, \psi_B^{(2)})$, where $\psi_X^{(l)}$ represents the envelope function of sublattice $X(= A, B)$ on layer $l(= 1, 2)$.

The $H_l(\boldsymbol{k})$ is given by [Eq. 2.50]

$$H_l(\boldsymbol{k}) = -\hbar v \left[\left(R\left(\mp\theta/2\right) + \mathcal{E}^{(l)} \right)^{-1} \left(\boldsymbol{k} + \frac{e}{\hbar} \boldsymbol{A}^{(l)} \right) \right] \cdot \boldsymbol{\sigma}, \tag{4.11}$$

where $\mp$ is for $l = 1$ and 2, respectively, v is the graphene's band velocity, $\boldsymbol{\sigma} = (\xi\sigma_x, \sigma_y)$ and σ_x, σ_y are the Pauli matrices in the sublattice space (A, B). For simplifying, we change the notation. We take $\hbar v/a = 2.14$ eV [57]. The $\boldsymbol{A}^{(l)}$ is the strain-induced vector potential that is given by [Eq. (2.51)]

$$\boldsymbol{A}^{(l)} = \xi \frac{3}{2} \frac{\beta\gamma_0}{ev} \begin{pmatrix} \epsilon_-^{(l)} \\ -\epsilon_{xy}^{(l)} \end{pmatrix}, \tag{4.12}$$

where $\gamma_0 = 2.7$ eV is the nearest neighbor transfer energy of intrinsic graphene and $\beta \approx 3.14$. Note that the strain-induced vector potential $\boldsymbol{A}^{(l)}$ depends only on $\epsilon_-^{(l)}$ and $\epsilon_{xy}^{(l)}$, while not on $\epsilon_+^{(l)}$ or $\Omega^{(l)}$. This is because $\boldsymbol{A}^{(l)}$ originates from a change of the tight-binding hopping energies between carbon atoms due to a lattice distortion, and it arises only when the hopping energies from a single carbon atom to three neighboring atoms are inequivalent. The $\Omega^{(l)}$ (rotation) and $\epsilon_+^{(l)}$ (isotropic expansion) obviously keep the three-fold rotational symmetry and hence do not contribute to $\boldsymbol{A}^{(l)}$.

The interlayer coupling matrix U is given by

$$U = \sum_{j=1}^{3} U_j e^{i\xi \boldsymbol{q}_j \cdot \boldsymbol{r}}. \tag{4.13}$$

The interlayer matrix U depends on the strain via $\boldsymbol{q}_j$'s [Eq. (4.9)].

Below we investigate the effect of lattice distortion on the energy bands using the effective Hamiltonian, Eq. (4.10). In fact, the electronic structure is mainly affected by the interlayer asymmetric components of the strain tensor [Eq. (4.3)], and in particular, the flat band is highly sensitive to ϵ_- and ϵ_{xy}. To demonstrate this, we calculate the energy bands of the magic-angle TBG ($\theta = 1.05°$) in the presence of asymmetric strain $\mathcal{E}^{(1)} = -\mathcal{E}^{(2)} = \mathcal{E}/2$, where different types of strain components $\Omega, \epsilon_+, \epsilon_-, \epsilon_{xy}$ are considered independently. Figure 4.3 shows the band dispersion and the density of state (DOS) in individual strain components, where black, green, red, and blue lines represent the strain amplitude (i.e., value of
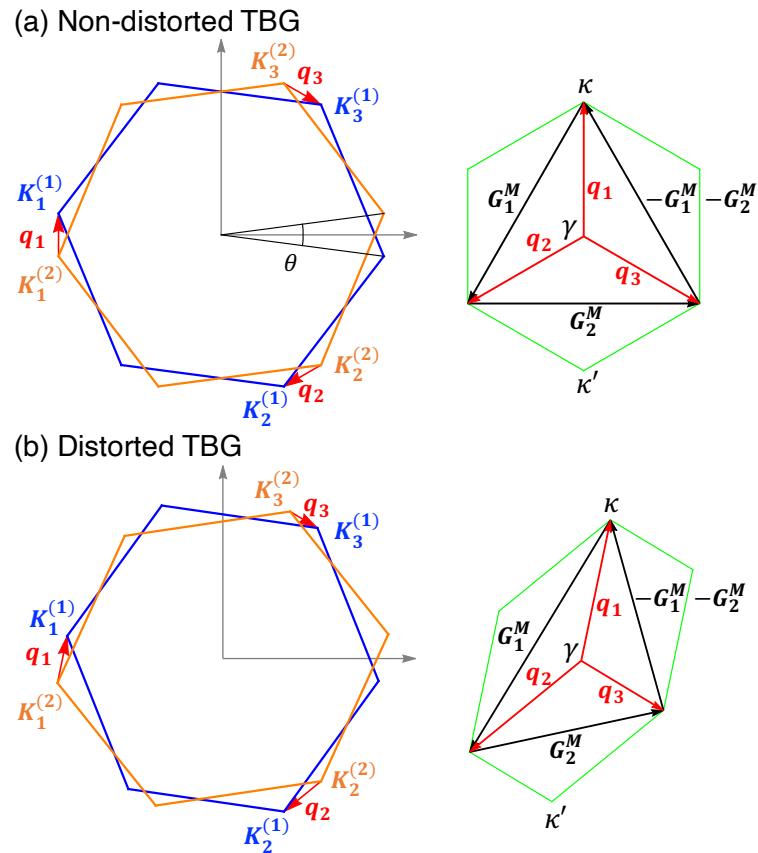
Figure 4.2: Brillouin zones of (a) a non-distorted TBG and (b) a distorted TBG. Blue and orange hexagons on the left represent the first Brillouin zone of graphene layer 1 and 2 (twisted by $\mp\theta/2$), respectively, and red arrows are the displacement vectors from the layer 2's K_+ point to layer 1's. A green hexagon on the right side is the moiré Brillouin zone.

$\Omega, \epsilon_+, \epsilon_-, \epsilon_{xy}$) of $0, 0.001, 0.002$ and 0.004, respectively.

We clearly observe that the central flat band is particularly sensitive to ϵ_- and ϵ_{xy}, where a small distortion of 0.001 leads to a significant split of the flat band about 20 meV. In contrast, ϵ_+ and Ω gives relatively minor effects. ϵ_+ moves the Dirac points at κ and κ' in the opposite directions in energy, resulting in a smaller DOS split. Ω shifts the twist angle from the magic angle and slightly broadens the flat band. The strain-induced flat band splitting was also found the previous work, which considered the effect of uniaxial heterostrain in TBG [143, 6, 148, 149, 150], which corresponds to ϵ_- and ϵ_{xy} in our notation.

It should also be noted that the split flat bands in Fig. 4.3 are not completely separated, but stick together at certain points near γ (off the path shown in Fig. 4.3) [143]. These Dirac points are originally located at κ and κ' in the non-distorted TBG, and when a uniform distortion is applied, they move without gap opening under the protection of the $C_{2z}T$ symmetry. The two Dirac points cannot pair-annihilate because they have the same Berry phase [157].

4.1.3 Pseudo Landau Level approximation

As shown in the previous section, the flat band is split significantly by anisotropic normal strain ϵ_- and shear strain ϵ_{xy}, while not much by other components. We explain this by using the pseudo Landau level picture of TBG [152], which describes the flat band as the Landau level (LL) under a moiré-induced fictitious magnetic field. We apply the same formulation to the strained TBG, Eq. (4.10), and analytically estimate the flat-band split energy.

The pseudo-LL Hamiltonian is obtained by rewriting the Hamiltonian matrix [Eq. (4.10)] in the basis $(\psi_A^+, \psi_B^+, \psi_A^-, \psi_B^-)$ where $\psi_X^\pm = (\psi_X^{(1)} \pm i\psi_X^{(2)})/\sqrt{2}$, and then expanding it in $\boldsymbol{r}$ with respect to the origin (the AA-point) upto the first order [152]. We ignore $\left(R\left(\mp\theta/2\right) + \mathcal{E}^{(l)}\right)^{-1}$ in Eq. (4.11), which gives only higher order effects. The detailed calculation is presented in Appendix 6.1.
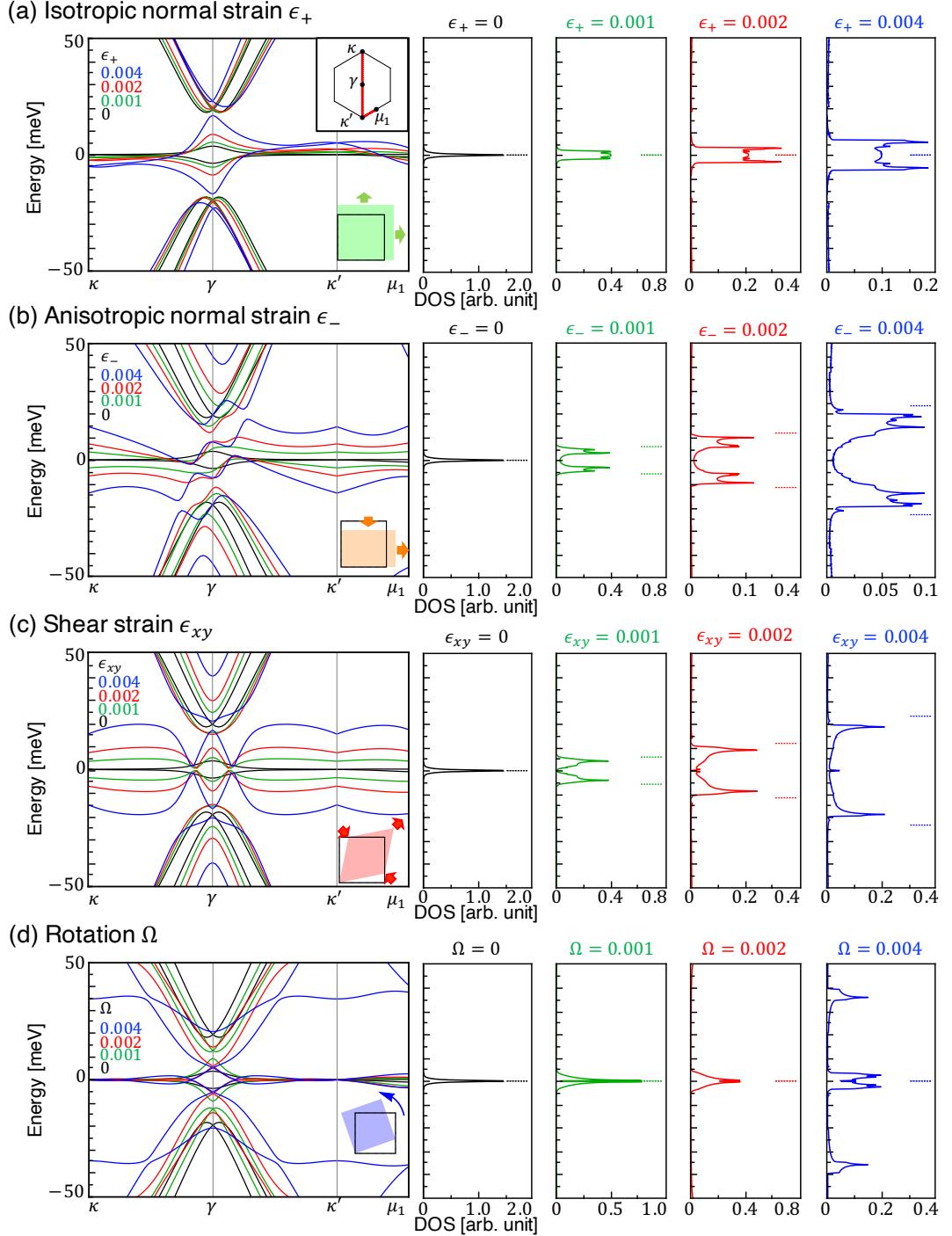
Figure 4.3: Band structure and the DOS of uniformly distorted magic-angle TBGs with different types of strain components, $\epsilon_+, \epsilon_-, \epsilon_{xy}, \Omega$. Different colors represent different amplitudes of strain. horizontal lines in the right panels (DOS) indicate energies of the split levels in the pseudo Landau level picture.

As a result, the effective Hamiltonian is written as

$$H_{\mathrm{PLL}} = \begin{pmatrix} H_+ & V^\dagger \\ V & H_- \end{pmatrix},$$

(4.14)

where

$$H_\pm = -\hbar v \left(\mathbf{k} \pm \frac{e}{\hbar} \mathbf{a}(\mathbf{r}) \right) \cdot \boldsymbol{\sigma},$$

(4.15)

$$\mathbf{a}(\mathbf{r}) = \xi \frac{2\pi u'}{eva} (\theta - \Omega) \begin{pmatrix} -y \\ x \end{pmatrix}.$$

(4.16)

Eq. (4.15) is essentially the Dirac Hamiltonian under a uniform magnetic field $\nabla \times (\pm \mathbf{a}) = (0, 0, \pm b_{\mathrm{eff}})$ with $b_{\mathrm{eff}} = \xi[4\pi u'/(e^2 va)](\theta - \Omega)$. Note that the pseudo vector potential $\mathbf{a}(\mathbf{r})$ originates from the inter-sublattice coupling u' in the moiré interlayer Hamiltonian [Eq. (4.13)], and it should be distinguished from the strain-induced vector potential $\mathbf{A}^{(l)}$.

The off-diagonal matrix V is given by

$$V = \left(-3\mathrm{i} u I_2 - \frac{ev}{2} \mathbf{A} \cdot \boldsymbol{\sigma} \right) \mathrm{e}^{-\mathrm{i}\frac{2e}{\hbar}\chi(\mathbf{r})},$$

(4.17)

where I_2 is a 2×2 identity matrix, u is the intra-sublattice coupling in moiré interlayer Hamiltonian [Eq. (4.13)], and

$$\mathbf{A} = \mathbf{A}^{(1)} - \mathbf{A}^{(2)} = \xi \frac{3}{2} \frac{\beta \gamma_0}{ev} \begin{pmatrix} \epsilon_- \\ -\epsilon_{xy} \end{pmatrix},$$

(4.18)

$$\chi(\mathbf{r}) = \xi \frac{\pi u'}{eva} \left[(x^2 + y^2)\epsilon_+ + (x^2 - y^2)\epsilon_- + xy\epsilon_{xy} \right].$$

(4.19)

Here $\mathbf{A}^{(l)}$ is the strain-induced vector potential argued in the previous section.

In the absence of the off-diagonal matrix V, the eigenstates are given by the

pseudo LLs of sector $H_\pm$. For $\xi = +$ valley, it is explicitly written as

$$|+, 0, m\rangle = \begin{pmatrix} 0 \\ \varphi_{0,m} \\ 0 \\ 0 \end{pmatrix}, \quad |-, 0, m\rangle = \begin{pmatrix} 0 \\ 0 \\ \varphi_{0,m} \\ 0 \end{pmatrix}, \quad (4.20)$$

where $\varphi_{0,m}(\boldsymbol{r}) \propto e^{-im\phi} e^{-r^2/(4l_{\text{eff}}^2)}$ is the 0th LL wavefunction with angular momentum m expressed in the polar coordinate $\boldsymbol{r} = r(\cos\phi, \sin\phi)$, and $l_{\text{eff}} = \sqrt{\hbar/(eb_{\text{eff}})}$. The 0th LLs in Eq. (4.20) have exactly opposite sublattice polarization (i.e., $|+, 0, m\rangle$ on B, and $|-, 0, m\rangle$ on A), because the Dirac Hamiltonians $H_\pm$ have opposite pseudo magnetic fields $\pm b_{\text{eff}}$.

In the absence of distortion ($\boldsymbol{A} = \chi = 0$), the 0th LLs remain the zero-energy eigenstates even we include the off-diagonal terms $-3iuI_2$ [Eq. (4.17)], because I_2 does not mix different sublattices. The flat band of TBG is understood by these degenerate 0th LLs. Since the effective Hamiltonian Eq. (4.20) is based on the linear expansion around $\boldsymbol{r} = 0$ (the AA spot), the approximation is valid for the LL wavefunctions with small angular momenta m's, which are well localized to $\boldsymbol{r} = 0$.

When we switch on the distortion terms, the 0th Landau levels are immediately hybridized by $\boldsymbol{A} \cdot \boldsymbol{\sigma}$ in the off-diagonal matrix V, and split into $E = \pm\Delta E/2$, where

$$\Delta E = ev|\boldsymbol{A}| = \frac{3}{2}\beta\gamma_0\sqrt{\epsilon_-^2 + \epsilon_{xy}^2}. \quad (4.21)$$

Note that the pseudo gauge potential $\chi(\boldsymbol{r})$ only contributes to the phase factor of the coupling matrix elements [Eq. (4.17)], giving a higher order correction to the splitting energy (see, Appendix 6.1). Eq. (4.21) explains the exclusive dependence of the flat band splitting on ϵ_- and ϵ_{xy}. Considering $(3/2)\beta\gamma_0 \approx 13\,\text{eV}$, a distortion $(\epsilon_-, \epsilon_{xy})$ of the order of 10^{-3} corresponds to a split width $\Delta E \sim 10\,\text{meV}$.

In Fig. 4.3, horizontal red lines represent $\pm\Delta E/2$ of Eq. (4.21), showing a good agreement with the actual split width of the DOS. In the energy bands, the structures at κ, κ' and μ_i are nicely explained by this simple splitting picture. On the other hand, the energy bands around γ point is rather complicated and cannot be captured by the same approximation. This is consistent with the fact that the wavefunction at γ is extended over the entire moiré pattern unlike those at κ, κ' and μ_i concentrating on AA points [158, 159, 160, 161], and hence the pseudo LL approximation (assuming the localization at AA point) fails. The Dirac band touching mentioned above actually occurs near γ.

4.2 TBG with non-uniform distortion

4.2.1 Theoretical modelling

In this section, we construct a theoretical model to simulate a non-uniform distortion in TBG. We consider a super moiré unit cell composed of $n_{\mathrm{SM}} \times n_{\mathrm{SM}}$ original moiré units (n_{SM}: integer), and assume that the lattice distortion is periodic with the super period as illustrated in Fig. 4.1. The primitive lattice vectors for the super unit cell are given by $\boldsymbol{L}_j^{\mathrm{SM}} = n_{\mathrm{SM}}\boldsymbol{L}_j^{\mathrm{M}}$ and the corresponding reciprocal lattice vectors are $\boldsymbol{G}_j^{\mathrm{SM}} = \boldsymbol{G}_j^{\mathrm{M}}/n_{\mathrm{SM}}$.

We define the in-plane displacement vector of layer $l = 1, 2$ as

$$\boldsymbol{u}^{(l)}(\boldsymbol{r}) = \sum_{\boldsymbol{p}} \boldsymbol{C}_{\boldsymbol{p}}^{(l)} \mathrm{e}^{-(\lambda|\boldsymbol{p}|/2\pi)^2} \mathrm{e}^{\mathrm{i}\boldsymbol{p}\cdot\boldsymbol{r}}, \tag{4.22}$$

which represents a deformation such that a carbon atom of layer l at a position $\boldsymbol{r}$ is shifted to $\boldsymbol{r} + \boldsymbol{u}^{(l)}(\boldsymbol{r})$. Here $\boldsymbol{p}$ runs over $\boldsymbol{p} = m_1\boldsymbol{G}_1^{\mathrm{SM}} + m_2\boldsymbol{G}_2^{\mathrm{SM}}$, and λ is the characteristic wave length of the spatial dependence of $\boldsymbol{u}^{(l)}(\boldsymbol{r})$. The amplitude $\boldsymbol{C}_{\boldsymbol{p}}^{(l)} = (C_{\boldsymbol{p},x}^{(l)}, C_{\boldsymbol{p},y}^{(l)})$ is a two-dimensional random vector which satisfy $\boldsymbol{C}_{-\boldsymbol{p}}^{(l)} = \boldsymbol{C}_{\boldsymbol{p}}^{(l)*}$ for real-valued $\boldsymbol{u}^{(l)}(\boldsymbol{r})$. We assume that different components of $\boldsymbol{C}_{\boldsymbol{p}}^{(l)}$ are totally

uncorrelated such that

$$\langle C_{\boldsymbol{p},i}^{(l)} C_{\boldsymbol{p}',j}^{(l')*} \rangle = \delta_{l,l'} \delta_{\boldsymbol{p},-\boldsymbol{p}'} \delta_{i,j} C_0^2, \tag{4.23}$$

where $\langle \rangle$ is the sampling average and C_0 is a length parameter to characterize the amplitude of the random displacement field.

The local strain tensors and the rotation angle can be expressed in terms of $\boldsymbol{u}^{(l)}(\boldsymbol{r})$ as

$$\epsilon_{ij}^{(l)}(\boldsymbol{r}) = \frac{1}{2} \left(\partial_i u_j^{(l)} + \partial_j u_i^{(l)} \right) \tag{4.24}$$

$$\Omega^{(l)}(\boldsymbol{r}) = \frac{1}{2} \left(\partial_x u_y^{(l)} - \partial_y u_x^{(l)} \right). \tag{4.25}$$

As in the uniform case, we define $\epsilon_{\pm}^{(l)}(\boldsymbol{r})$ by Eq. (4.2), and relative strain components $\epsilon_{\pm}(\boldsymbol{r}), \epsilon_{xy}(\boldsymbol{r}), \Omega(\boldsymbol{r})$ by Eq. (4.3). We introduce the magnitude of distortion, ϵ, as the root mean square of the interlayer difference of the strain tensor elements [Eq. (4.3)], or,

$$\epsilon \equiv \sqrt{\langle |\epsilon_{\pm}|^2 \rangle} = \sqrt{\langle |\epsilon_{xy}|^2 \rangle} = \sqrt{\langle |\Omega|^2 \rangle} = \sqrt{\frac{\pi^3}{2} \frac{C_0^2 S_{\mathrm{SM}}}{\lambda^4}}, \tag{4.26}$$

where $S_{\mathrm{SM}} = |\boldsymbol{L}_1^{\mathrm{SM}} \times \boldsymbol{L}_2^{\mathrm{SM}}|$ is the area of the super moiré unit cell.

Figure 4.1 show examples of distorted moiré patterns in the magic-angle TBG($\theta = 1.05°$) with different values of $\epsilon = 0, 0.0006, 0.0012, 0.0018$, where $n_{\mathrm{SM}} = 8$ (indicated by a big parallelogram) and $\lambda = 7L_M$. We adopted a continuous color code to express the stacking sequence [37], where the bright region represents local AA stack and the dark region represents AB/BA stack. The red dots are the AA spots of the non-distorted TBG for reference. It should be noted that a small distortion in graphene lattice of the order of ϵ is magnified to the moiré disorder of $\epsilon/\theta \sim 60\epsilon$.

We calculate the energy spectrum by using an extended continuum model incorporating non-uniform lattice distortion [42]. The Hamiltonian is given by

Eq. (4.10), where the diagonal blocks are replaced by

$$H_l(\mathbf{k}) = -\hbar v \left(\mathbf{k} + \frac{e}{\hbar} \mathbf{A}^{(l)}(\mathbf{r}) \right) \cdot \boldsymbol{\sigma}, \tag{4.27}$$

with the local strain-induced vector potential

$$\mathbf{A}^{(l)}(\mathbf{r}) = \xi \frac{3}{2} \frac{\beta \gamma_0}{ev} \begin{pmatrix} \epsilon_-^{(l)}(\mathbf{r}) \\ -\epsilon_{xy}^{(l)}(\mathbf{r}) \end{pmatrix}, \tag{4.28}$$

and the interlayer coupling U is replaced with,

$$U = \sum_{j=1}^{3} U_j \, \mathrm{e}^{\mathrm{i}\xi[\mathbf{q}_j \cdot \mathbf{r} + \mathbf{K}_j \cdot (\mathbf{u}^{(2)}(\mathbf{r}) - \mathbf{u}^{(1)}(\mathbf{r}))]}. \tag{4.29}$$

Here U_j are defined in Eq. (4.13), $\mathbf{K}_j$ are the corner points of an intrinsic graphene [Eq. (4.6)] and $\mathbf{q}_j$ are interlayer corner-point shifts [Eq. (4.8)] of non-distorted TBG. In the diagonal matrix, we neglected the rotation matrix $\left(R\left(\mp\theta\right) + \mathcal{E}^{(l)} \right)^{-1}$ in Eq. (4.11), which gives a minor effect in the uniform distortion case.

While in this thesis we focus on the in-plane components of lattice displacement, real TBG samples also contain out-of-plane corrugations [32, 33, 39]. The primary effect of the corrugation is to differentiate the lattice spacing of AA-stacking and AB-stacking regions, which is effectively incorporated by the difference between u and u' parameters in the matrix U [57, 42], as already mentioned. We may also have an additional effect from non-uniform corrugation, which is left for future work.

4.2.2   Energy spectrum and flat-band splitting

Using the model obtained above, we calculate the local density of states (LDOS) for the magic-angle TBG ($\theta = 1.05°$) with a randomly-generated displacement configuration $\mathbf{u}^{(l)}(\mathbf{r})$. First, we take $\epsilon = 0.0004$, $\lambda = 7L_M$, and $n_{\mathrm{SM}} = 12$. Figure 4.4(a) illustrates the moiré structure, where the distortion is barely observed as
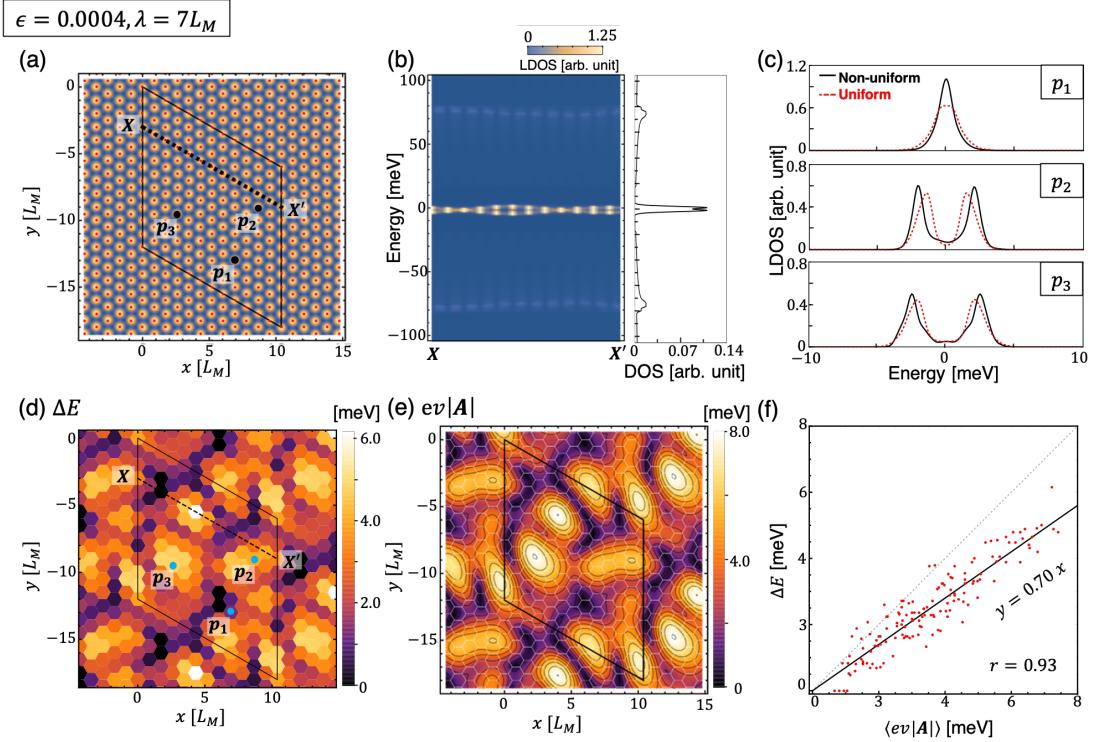
Figure 4.4: (a) Moiré pattern of a disordered magic-angle TBG with $\epsilon = 0.0004, \lambda = 7L_{\mathrm{M}}$. The distortion is observed as slight shifts of AA points (yellow spots) relative to the regular red dots. (b) LDOS along line XX' [defined by a broken line in (a)]. (c) (Black, solid) LDOS at the points of p_1, p_2, p_3 in (a). (Red, dashed) LDOS at the AA point of the corresponding uniform TBG with the strain tensors fixed to the local value. (d) The spatial distribution of the splitting energy ΔE, or the energy distance between the two LDOS peaks. A hexagonal tile corresponds to a single moiré unit cell, and its color represents ΔE at the center of the hexagon (the AA point). (e) A contour plot of the interlayer difference of the strain-induced vector potential, $ev|A(r)|$. (f) A scattered plot of ΔE and $ev|A|$ (averaged in every moiré unit cell).

a slight shift of AA points (yellow spots) with respect to the regular red dots. In Fig. 4.4(b), we plot the LDOS along line XX', which is defined by a broken line in Fig. 4.4(a). We can see that the LDOS of the flat band separates into upper and lower parts by a splitting energy depending on the position. This is quite different from the case of a random electrostatic potential which simply broadens the band width. Figure 4.4(d) shows the spatial distribution of the splitting energy ΔE, which is defined by the energy distance between the two LDOS peaks. Here a hexagonal tile corresponds to a single moiré unit cell, and its color represents ΔE at the center of the hexagon (the AA point).

Actually, the local split width of the flat band is almost solely determined by the local value of the interlayer difference of the strain-induced vector potential,

$$A(r) = A^{(1)}(r) - A^{(2)}(r),\qquad(4.30)$$

and the local splitting energy is approximately given by $\Delta E \sim ev|A(r)|$ as in the uniform case [Eq. (4.18)]. To demonstrate this, we show a contour plot of $ev|A(r)|$ in Fig. 4.4(e). We observe a nearly perfect agreement with the distribution of ΔE in Fig. 4.4(d). We also present a scattered plot of ΔE and $ev|A|$ (averaged in every moiré unit cell) in Fig. 4.4(f), where we have a high correlation coefficient $r \approx 0.93$, and a fitted line is given by $\Delta E \approx 0.7ev|A|$. The strong correlation between the splitting width and the strain-induced vector potential is a special property of the magic-angle flat band, as it relies on its peculiar Landau level like wavefunction. On the other hand, the position of the satellite peaks (around ± 80 meV in Fig. 4.4) is totally uncorrelated with $ev|A|$ (the correlation coefficient about $r \sim 0.1$), but it is weakly correlated with the local twist angle Ω ($r \sim 0.5$).

These results suggest that the local electronic structure in the flat band region of non-uniform TBG is well described by a uniform Hamiltonian with the strain tensors fixed to the local value. In Fig. 4.4(c), we plot the LDOS of the non-uniform TBG at the points of p_1, p_2, p_3 in Fig. 4.4(a), and the local density of states of the corresponding uniform TBGs at AA point. Indeed, we see a nice agreement between the two curves. We also note that the LDOS is never completely gapped out at $E = 0$, in accordance with the calculation of uniformly-strained TBGs where the two flat bands are always connected by the Dirac points.

The approximation with the local Hamiltonian is usually expected to be valid in a long-range limit with $\lambda \gg L_M$, but actually it works fairly well down to a short-ranged distortion. Figure 4.5 shows the plots similar to Fig. 4.4 calculated for different characteristic wave lengths, $\lambda = 5L_M, 3L_M, L_M$. The correlation coefficient between ΔE and $ev|A|$ is found to be 0.90 at $\lambda = 3L_M$, and it is still 0.73 at $\lambda = L_M$. We presume that it reflects the strongly localized feature of the
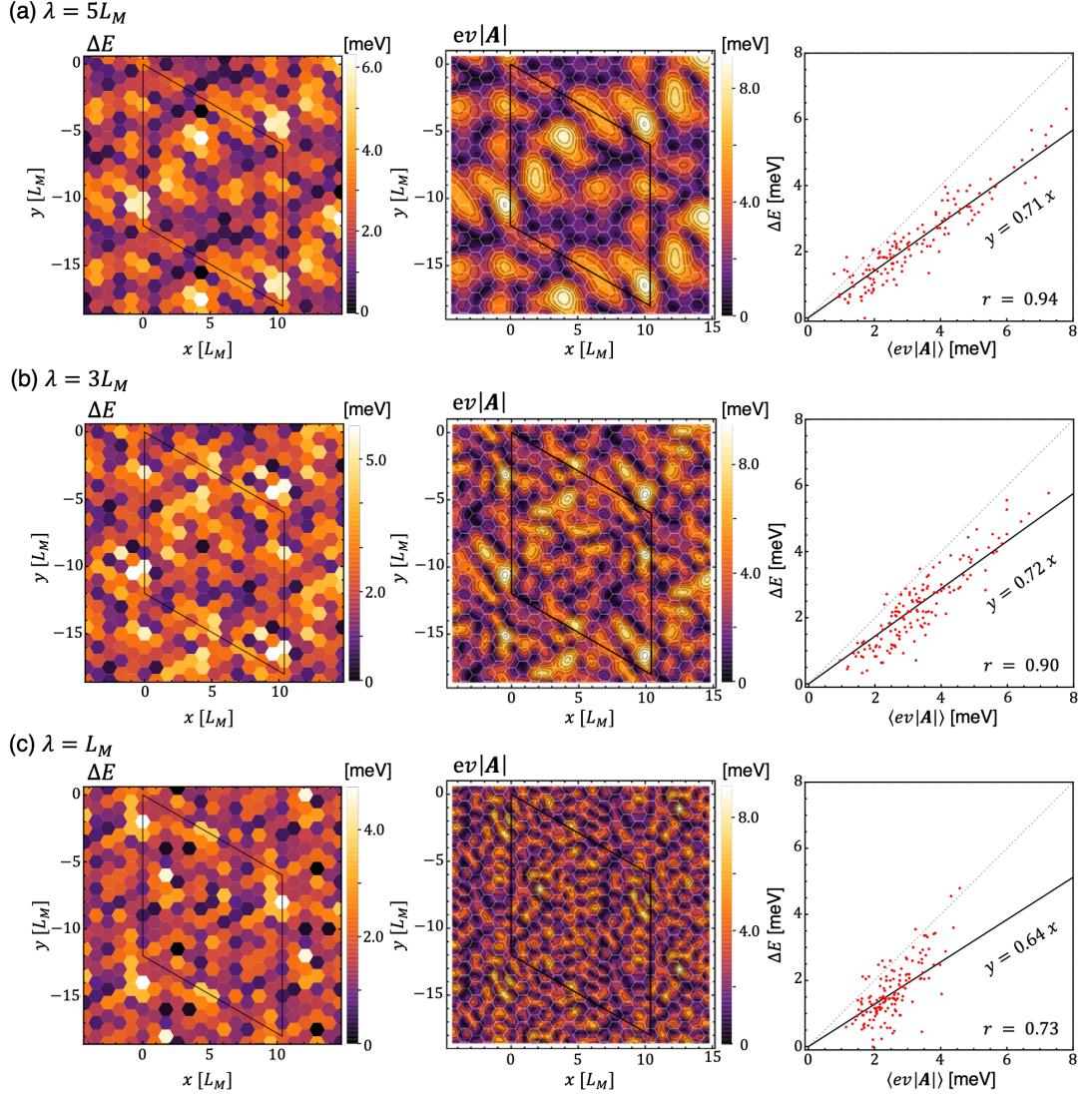
Figure 4.5: Plots similar to Figs. 4.4(d)-(f) calculated for different characteristic wave lengths $\lambda = 5L_M, 3L_M, L_M$.

flat-band wavefunctions.

Figure 4.6 plots the total DOS of non-uniform TBG in different distortion amplitudes ϵ with $\lambda = 7L_M$, For each curve, we take an overage over different random configurations. We see that the two-level splitting feature in the LDOS still remains as a double peak structure in the total DOS. In increasing ϵ, the curve is simply extended horizontally, as expected the relationship $\Delta E \sim ev|\mathbf{A}|$. The form of the DOS curve is roughly determined by the distribution function $D(|\mathbf{A}|)$, which is plotted as broken line in Fig. 4.6 for the current model. Here we scale the horizontal axis by $E = 0.7ev|\mathbf{A}|$ in accordance with Fig. 4.4(f).
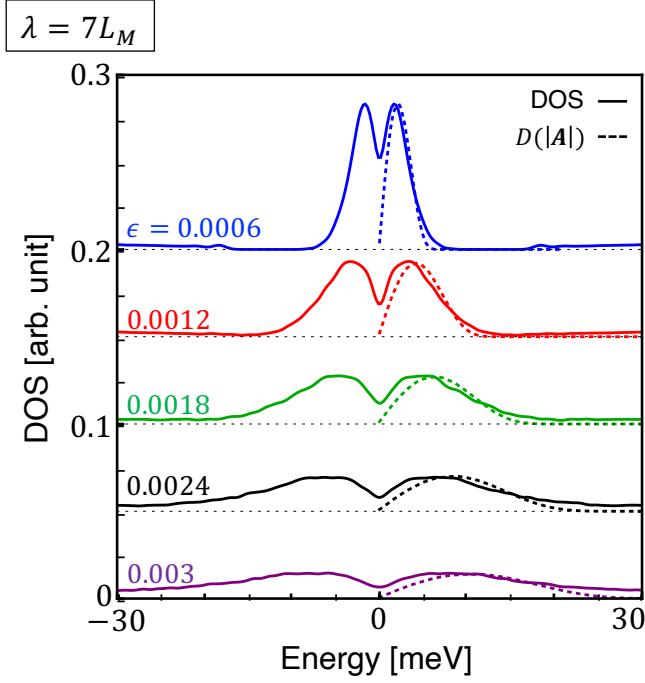
Figure 4.6: The total DOS of disordered magic-angle TBGs with different distortion amplitudes ϵ. For each curve, we take an average over different random configurations. Broken lines are the distribution function $D(|A|)$ with horizontal axis scaled by $E = 0.7ev|A|$.

By using the formula Eq. (4.21), we can roughly estimate the flat band split energy in real TBG samples. A recent local measurement of the magic-angle TBG [113] has shown that the local twist angle slowly varies from $\theta = 1.05°$ to $1.18°$ (amounts to $\Omega \simeq 0.001$ (rad)) in a length scale of μm. The system can be viewed as a part of a disordered moiré pattern as in Fig. 4.1, but with a greater length scale. Here the twist angle variation Ω does not stand alone, but it is always accompanied by other strain components $\epsilon_+, \epsilon_-, \epsilon_{xy}$ with similar amplitudes, because they stem from the same lattice displacement $\mathbf{u}(\mathbf{r})$. It is then expected that the spatial variation of Ω gives a relatively minor effect, while the ϵ_- and ϵ_{xy} give rise to a flat band splitting just as in our simulation. If we assume $\epsilon_-, \epsilon_{xy} \simeq 0.001$, the typical value of the flat band split width on this sample is estimated at $\Delta E \simeq 10$ meV by using Eq. (4.21). The result suggests that, in realistic magic-angle TBGs with non-uniform moiré disorder, the flat band is not actually a single band cluster but it splits by a sizable energy in most places.

It is consistent with the STM measurements of TBGs near the magic angle [5, 8], where a significant separation of the LDOS was observed. The local flat-band separation may also be responsible for the pronounced Landau fan at the charge neutral point which is commonly observed in the transport experiments [3, 4, 11, 113], since the two separate bands are always touching as argued in Sec. 4.1. The splitting of the flat band would affect the ground state properties in the presence of the electron-electron interaction, since the Hilbert space of the half-split flat band is different from the original full flat band.

While we focus on the strain effect in this calculation, the distortion of the moiré pattern should also give rise to a non-uniform electrostatic potential via an inhomogeneous charge distribution[158, 140, 162, 154]. We expect that the effect is roughly captured by including a local shift of the energy in the present calculation. At the filling factor $\nu = 2$ (i.e. half-filling of the upper flat band), for instance, the upper LDOS peak would be aligned to the Fermi energy without changing the local splitting width, to achieve the homogeneous electron density of $\nu = 2$. We leave a detailed calculation including the electrostatic potential for future works.

Our results suggest that moiré disorder should have significant effects in other moiré systems, such as twisted trilayer graphene (TTG)[163, 60, 72, 71, 64, 73, 164, 165, 69] and twisted double bilayer graphene (TDBG)[166, 167, 168, 169, 170, 171]. Compared to TBG, these multilayer systems have greater degree of freedom in relative lattice displacement and it may give rise to more complex phenomena. In TTG, for instance, the interlayer displacement can be classified by mirror reflection symmetry, where we expect that the mirror-symmetric component splits the flat band as in TBG, while the asymmetric part contributes to a hybridization of the flat band and the Dirac-like band, which have different mirror eigenvalues[163, 69]. The application of the moiré disorder theory to these multilayer moiré systems will be presented elsewhere.

Chapter 5

Conclusion

In this thesis, we present conprehensive studies on lattice distortion and electronic structures in non-periodic moiré systems. Specifically, we investigated trilayer moiré systems as well as disordered moiré systems, both of which pose theoretical challenges due to their vast structural length scales.

In Chapter 3, we have presented a systematic investigation on general non-symmetric twisted trilayer graphenes (TTGs). For various chiral and alternating TTGs with different twist angle combinations, we employed an effective continuum approach similar to twisted bilayer graphene, to obtain the optimized lattice structure. we found that there are two distinct length-scale relaxations in the moiré-of-moiré scale and moiré scale. This leads to a formation of a patchwork of moiré-of-moiré domains, where the two moiré patterns become locally commensurate. Specifically, the chiral TTGs prefer a shifted stacking to avoid the overlap of AA spots in the individual moiré patterns. In contrast, the alternating TTGs exhibits a completely opposite behavior where AA spots are perfectly overlapped. The preferred structure of moiré-of-moiré domains can be explained by an intuitive picture based on the frustration of the lattice relaxation, where the AA spots in the competing moiré patterns interact with each other with attractive or repulsive force. This insight offers valuable guidance for estimating the preferred domain structures in general twisted multilayers without the need for extensive numerical calculations.

We also computed the electronic band structure of TTGs by using a continuum band calculation method incorporating lattice relaxation effects. We found that the chiral TTG exhibits an energy window where highly one-dimensional electron

bands are sparsely distributed. By calculating the Chern number of the local band structure within the commensurate domains, we identify one-dimensional domain boundary states as topological boundary states between distinct Chern insulators. The alternating TTG exhibits a clear separation of the flat bands and a monolayer-like Dirac cone, as a consequence of the formation of commensurate domains equivalent to the symmetric TTG.

In Chapter 4, we have studied the electronic structure of the twisted bilayer graphene with non-uniform moiré distortion. Using an extended continuum model that incorporates nonuniform lattice distortion, we have demonstrated that the local density of states (LDOS) within the flat band remains relatively unchanged but splits into upper and lower subbands. We found that the flat-band splitting is mainly caused by the local interlayer difference of anisotropic normal strain and shear strain, while isotropic strain and rotation give relatively minor effects. The splitting of the flat band can well be described by a pseudo landau level picture for the magic-angle flat band, and an analytical expression of the splitting energy is obtained. Even in cases of short-ranged distortion with a characteristic length scale smaller than the moiré period, the alignment between the splitting energy of the LDOS and the local strain persists. This observation highlights the highly localized nature of the flat band wave function.

Finally, the theoretical model presented in this thesis holds significant potential for applications in a wide range of moiré systems composed of various 2D materials. The complex lattice relaxation can be determined by just a small number of parameters, such as the elastic constants and the registry-dependent interlayer potential between neighboring layers (i.e., interlayer binding energy at AA, AB and BA stacking), which are already known for most two-dimensional materials. Once these parameters are determined, we can optimize the domain structure and predict the geometric shape of the domains. Subsequently, we can calculate the electronic structure to examine the topological properties of the system. As a result, our theoretical scheme serves as a fundamental tool and

guiding principle for topological band engineering in twisted multilayers beyond graphene bilayers. Studying super-moiré multilayer systems, which offer numerous configuration possibilities, presents an opportunity to explore a new realm beyond traditional moiré bilayers, expanding the scope of research in the field of materials science.

Chapter 6

Appendix

6.1 Pseudo Landau Level Hamiltonian

In this appendix, we derive the pseudo landau level Hamiltonian Eq. (4.14) by applying the method of Ref. [152] to the disordered TBG. By defining

$$\psi_X^{\pm} = (\psi_X^{(1)} \pm i\psi_X^{(2)})/\sqrt{2} \quad (X = A, B), \tag{6.1}$$

the Hamiltonian matrix of Eq. (4.10) is written in the basis $(\psi_A^+, \psi_B^+, \psi_A^-, \psi_B^-)$ as

$$H = \begin{pmatrix} h_+ + \dfrac{i}{2}(U - U^\dagger) & h_- + \dfrac{i}{2}(U + U^\dagger) \\ h_- - \dfrac{i}{2}(U + U^\dagger) & h_+ - \dfrac{i}{2}(U - U^\dagger) \end{pmatrix}, \tag{6.2}$$

where

$$h_+ = -\left(\hbar v \boldsymbol{k} + ev\frac{\boldsymbol{A}^{(1)} + \boldsymbol{A}^{(2)}}{2}\right) \cdot \boldsymbol{\sigma}$$

$$h_- = -ev\frac{\boldsymbol{A}^{(1)} - \boldsymbol{A}^{(2)}}{2} \cdot \boldsymbol{\sigma}. \tag{6.3}$$

In the following, we neglect the homostrain component $\boldsymbol{A}^{(1)} + \boldsymbol{A}^{(2)}$, and focus on the heterostrain part $\boldsymbol{A} = \boldsymbol{A}^{(1)} - \boldsymbol{A}^{(2)}$.

Since the wavefuncton of the flat band is localized around the AA region, we expand the interlayer coupling matrix $U(\boldsymbol{r})$ around the AA stacking point ($\boldsymbol{r} = 0$)

to the linear order of r/L_M. As a result, we have

$$\frac{U + U^\dagger}{2} = \sum_{j=1}^{3} U_j \cos\boldsymbol{q}_j \cdot \boldsymbol{r} \approx 3uI_2 \tag{6.4}$$

$$\mathrm{i}\frac{U - U^\dagger}{2} = \sum_{j=1}^{3} U_j \sin\boldsymbol{q}_j \cdot \boldsymbol{r} \approx \sum_{j=1}^{3} U_j \boldsymbol{q}_j \cdot \boldsymbol{r}. \tag{6.5}$$

By using Eqs. (6.5) and (4.9), the diagonal part of the Hamiltonian (6.2) is written as

$$h_+ \pm \frac{\mathrm{i}}{2}(U - U^\dagger) = -\hbar v \left[\boldsymbol{k} \pm \frac{e}{\hbar}\left(\boldsymbol{a}(\boldsymbol{r}) + \nabla\chi(\boldsymbol{r})\right)\right] \cdot \boldsymbol{\sigma} \tag{6.6}$$

where $\boldsymbol{a}(\boldsymbol{r})$ is the pseudo vector potential of Eq. (4.16) and the $\chi(\boldsymbol{r})$ is the gauge potential of Eq. (4.19). Finally, the effective Hamiltonian Eq. (4.14) is obtained by applying a gauge transformation,

$$\begin{pmatrix} \tilde{\psi}_X^{(+)} \\ \tilde{\psi}_X^{(-)} \end{pmatrix} = \begin{pmatrix} \mathrm{e}^{-\mathrm{i}\frac{e}{\hbar}\chi} & 0 \\ 0 & \mathrm{e}^{+\mathrm{i}\frac{e}{\hbar}\chi} \end{pmatrix} \begin{pmatrix} \psi_X^{(+)} \\ \psi_X^{(-)} \end{pmatrix}. \tag{6.7}$$

The coupling matrix elements in the 0th LLs are given by

$$\langle -, 0, m'|V|+, 0, m\rangle = \frac{ev}{2}\boldsymbol{A} \cdot \boldsymbol{\sigma}\langle\varphi_{0,m'}|\mathrm{e}^{-\mathrm{i}\frac{2e}{\hbar}\chi(\boldsymbol{r})}|\varphi_{0,m}\rangle$$

$$\approx \frac{ev}{2}\boldsymbol{A} \cdot \boldsymbol{\sigma}\left[\delta_{m,m'} - 2\mathrm{i}\frac{e}{\hbar}\langle\varphi_{0,m'}|\chi(\boldsymbol{r})|\varphi_{0,m}\rangle\right]. \tag{6.8}$$

Therefore, the gauge potential χ only contributes to a higher order correction in the 0th LL splitting.

Bibliography

[1] R. Bistritzer and A. MacDonald, "Moiré bands in twisted double-layer graphene," *Proc. Natl. Acad. Sci.*, vol. 108, no. 30, p. 12233, 2011.

[2] Y. Cao, V. Fatemi, A. Demir, S. Fang, S. L. Tomarken, J. Y. Luo, J. D. Sanchez-Yamagishi, K. Watanabe, T. Taniguchi, E. Kaxiras, R. C. Ashoori, and P. Jarillo-Herrero, "Correlated insulator behaviour at half-filling in magic-angle graphene superlattices," *Nature*, vol. 556, no. 7699, pp. 80–84, 2018. [Online]. Available: https://doi.org/10.1038/nature26154

[3] Y. Cao, V. Fatemi, S. Fang, K. Watanabe, T. Taniguchi, E. Kaxiras, and P. Jarillo-Herrero, "Unconventional superconductivity in magic-angle graphene superlattices," *Nature*, vol. 556, no. 7699, pp. 43–50, 2018. [Online]. Available: https://doi.org/10.1038/nature26160

[4] M. Yankowitz, S. Chen, H. Polshyn, Y. Zhang, K. Watanabe, T. Taniguchi, D. Graf, A. F. Young, and C. R. Dean, "Tuning superconductivity in twisted bilayer graphene," *Science*, vol. 363, no. 6431, pp. 1059–1064, 2019. [Online]. Available: https://www.science.org/doi/abs/10.1126/science.aav1910

[5] A. Kerelsky, L. J. McGilly, D. M. Kennes, L. Xian, M. Yankowitz, S. Chen, K. Watanabe, T. Taniguchi, J. Hone, C. Dean, A. Rubio, and A. N. Pasupathy, "Maximized electron interactions at the magic angle in twisted bilayer graphene," *Nature*, vol. 572, no. 7767, pp. 95–100, 2019. [Online]. Available: https://doi.org/10.1038/s41586-019-1431-9

[6] Y. Xie, B. Lian, B. Jäck, X. Liu, C.-L. Chiu, K. Watanabe, T. Taniguchi, B. A. Bernevig, and A. Yazdani, "Spectroscopic signatures of many-body correlations in magic-angle twisted bilayer graphene," *Nature*, vol. 572, no. 7767, pp. 101–105, 2019.

[7] Y. Jiang, X. Lai, K. Watanabe, T. Taniguchi, K. Haule, J. Mao, and E. Y. Andrei, "Charge order and broken rotational symmetry in magic-angle twisted bilayer graphene," *Nature*, vol. 573, no. 7772, pp. 91–95, 2019.

[8] Y. Choi, J. Kemmer, Y. Peng, A. Thomson, H. Arora, R. Polski, Y. Zhang, H. Ren, J. Alicea, G. Refael, F. von Oppen, K. Watanabe, T. Taniguchi, and S. Nadj-Perge, "Electronic correlations in twisted bilayer graphene near the magic angle," *Nature Physics*, vol. 15, no. 11, pp. 1174–1180, 2019. [Online]. Available: https://doi.org/10.1038/s41567-019-0606-5

[9] A. L. Sharpe, E. J. Fox, A. W. Barnard, J. Finney, K. Watanabe, T. Taniguchi, M. A. Kastner, and D. Goldhaber-Gordon, "Emergent ferromagnetism near three-quarters filling in twisted bilayer graphene," *Science*, vol. 365, no. 6453, pp. 605–608, 2019. [Online]. Available: https://www.science.org/doi/abs/10.1126/science.aaw3780

[10] H. Polshyn, M. Yankowitz, S. Chen, Y. Zhang, K. Watanabe, T. Taniguchi, C. R. Dean, and A. F. Young, "Large linear-in-temperature resistivity in twisted bilayer graphene," *Nature Physics*, vol. 15, no. 10, pp. 1011–1016, 2019.

[11] X. Lu, P. Stepanov, W. Yang, M. Xie, M. A. Aamir, I. Das, C. Urgell, K. Watanabe, T. Taniguchi, G. Zhang, A. Bachtold, A. H. MacDonald, and D. K. Efetov, "Superconductors, orbital magnets and correlated states in magic-angle bilayer graphene," *Nature*, vol. 574, no. 7780, pp. 653–657, 2019.

[12] Y. Cao, D. Chowdhury, D. Rodan-Legrain, O. Rubies-Bigorda, K. Watanabe, T. Taniguchi, T. Senthil, and P. Jarillo-Herrero, "Strange metal in magic-angle graphene with near planckian dissipation," *Phys. Rev. Lett.*, vol. 124, p. 076801, Feb 2020. [Online]. Available: https://link.aps.org/doi/10.1103/PhysRevLett.124.076801

[13] M. Serlin, C. L. Tschirhart, H. Polshyn, Y. Zhang, J. Zhu, K. Watanabe, T. Taniguchi, L. Balents, and A. F. Young, "Intrinsic quantized anomalous hall effect in a moiré heterostructure," *Science*, vol. 367, no. 6480, pp. 900–903, 2020. [Online]. Available: https://www.science.org/doi/abs/10.1126/science.aay5533

[14] G. Chen, A. L. Sharpe, E. J. Fox, Y.-H. Zhang, S. Wang, L. Jiang, B. Lyu, H. Li, K. Watanabe, T. Taniguchi *et al.*, "Tunable correlated chern insulator and ferromagnetism in a moiré superlattice," *Nature*, vol. 579, no. 7797, pp. 56–61, 2020.

[15] Y. Saito, J. Ge, K. Watanabe, T. Taniguchi, and A. F. Young, "Independent superconductors and correlated insulators in twisted bilayer graphene," *Nature Physics*, vol. 16, no. 9, pp. 926–930, 2020.

[16] U. Zondiner, A. Rozen, D. Rodan-Legrain, Y. Cao, R. Queiroz, T. Taniguchi, K. Watanabe, Y. Oreg, F. von Oppen, A. Stern *et al.*, "Cascade of phase transitions and dirac revivals in magic-angle graphene," *Nature*, vol. 582, no. 7811, pp. 203–208, 2020.

[17] D. Wong, K. P. Nuckolls, M. Oh, B. Lian, Y. Xie, S. Jeon, K. Watanabe, T. Taniguchi, B. A. Bernevig, and A. Yazdani, "Cascade of electronic transitions in magic-angle twisted bilayer graphene," *Nature*, vol. 582, no. 7811, pp. 198–202, 2020.

[18] P. Stepanov, I. Das, X. Lu, A. Fahimniya, K. Watanabe, T. Taniguchi, F. H. Koppens, J. Lischner, L. Levitov, and D. K. Efetov, "Untying the insulating and superconducting orders in magic-angle graphene," *Nature*, vol. 583, no. 7816, pp. 375–378, 2020.

[19] H. S. Arora, R. Polski, Y. Zhang, A. Thomson, Y. Choi, H. Kim, Z. Lin, I. Z. Wilson, X. Xu, J.-H. Chu *et al.*, "Superconductivity in metallic twisted bilayer graphene stabilized by wse2," *Nature*, vol. 583, no. 7816, pp. 379–384, 2020.

[20] P. Stepanov, M. Xie, T. Taniguchi, K. Watanabe, X. Lu, A. H. MacDonald, B. A. Bernevig, and D. K. Efetov, "Competing zero-field chern insulators in superconducting twisted bilayer graphene," *Phys. Rev. Lett.*, vol. 127, p. 197701, Nov 2021. [Online]. Available: https://link.aps.org/doi/10.1103/PhysRevLett.127.197701

[21] Z. Zhu, P. Cazeaux, M. Luskin, and E. Kaxiras, "Modeling mechanical relaxation in incommensurate trilayer van der waals heterostructures," *Phys. Rev. B*, vol. 101, p. 224107, Jun 2020. [Online]. Available: https://link.aps.org/doi/10.1103/PhysRevB.101.224107

[22] F. Lin, J. Qiao, J. Huang, J. Liu, D. Fu, A. S. Mayorov, H. Chen, P. Mukherjee, T. Qu, C.-H. Sow *et al.*, "Heteromoiré engineering on magnetic bloch transport in twisted graphene superlattices," *Nano Letters*, vol. 20, no. 10, pp. 7572–7579, 2020.

[23] X. Zhang, K.-T. Tsai, Z. Zhu, W. Ren, Y. Luo, S. Carr, M. Luskin, E. Kaxiras, and K. Wang, "Correlated insulating states and transport signature of superconductivity in twisted trilayer graphene superlattices," *Phys. Rev. Lett.*, vol. 127, p. 166802, Oct 2021. [Online]. Available: https://link.aps.org/doi/10.1103/PhysRevLett.127.166802

[24] Z. Zhu, S. Carr, D. Massatt, M. Luskin, and E. Kaxiras, "Twisted trilayer graphene: A precisely tunable platform for correlated electrons," *Phys. Rev. Lett.*, vol. 125, p. 116404, Sep 2020. [Online]. Available: https://link.aps.org/doi/10.1103/PhysRevLett.125.116404

[25] S. Turkel, J. Swann, Z. Zhu, M. Christos, K. Watanabe, T. Taniguchi, S. Sachdev, M. S. Scheurer, E. Kaxiras, C. R. Dean, and A. N. Pasupathy, "Orderly disorder in magic-angle twisted trilayer graphene," *Science*, vol. 376, no. 6589, pp. 193–199, 2022. [Online]. Available: https://www.science.org/doi/abs/10.1126/science.abk1895

[26] I. M. Craig, M. V. Winkle, C. Groschner, K. Zhang, N. Dowlatshahi, Z. Zhu, T. Taniguchi, K. Watanabe, S. M. Griffin, and D. K. Bediako, "Local atomic stacking and symmetry in twisted graphene trilayers," 2023.

[27] A. Uri, S. C. de la Barrera, M. T. Randeria, D. Rodan-Legrain, T. Devakul, P. J. D. Crowley, N. Paul, K. Watanabe, T. Taniguchi, R. Lifshitz, L. Fu, R. C. Ashoori, and P. Jarillo-Herrero, "Superconductivity and strong interactions in a tunable moiré quasiperiodic crystal," 2023.

[28] A. M. Popov, I. V. Lebedeva, A. A. Knizhnik, Y. E. Lozovik, and B. V. Potapkin, "Commensurate-incommensurate phase transition in bilayer graphene," *Phys. Rev. B*, vol. 84, no. 4, p. 045404, 2011.

[29] L. Brown, R. Hovden, P. Huang, M. Wojcik, D. A. Muller, and J. Park, "Twinning and twisting of tri-and bilayer graphene," *Nano Lett.*, vol. 12, no. 3, pp. 1609–1615, 2012.

[30] J. Lin, W. Fang, W. Zhou, A. R. Lupini, J. C. Idrobo, J. Kong, S. J. Pennycook, and S. T. Pantelides, "Ac/ab stacking boundaries in bilayer graphene," *Nano letters*, vol. 13, no. 7, pp. 3262–3268, 2013.

[31] J. S. Alden, A. W. Tsen, P. Y. Huang, R. Hovden, L. Brown, J. Park, D. A. Muller, and P. L. McEuen, "Strain solitons and topological defects in bilayer graphene," *Proc. Natl. Acad. Sci. USA*, vol. 110, no. 28, pp. 11 256–11 260, 2013.

[32] K. Uchida, S. Furuya, J.-I. Iwata, and A. Oshiyama, "Atomic corrugation and electron localization due to moiré patterns in twisted bilayer graphenes," *Phys. Rev. B*, vol. 90, no. 15, p. 155451, 2014.

[33] M. van Wijk, A. Schuring, M. Katsnelson, and A. Fasolino, "Relaxation of moiré patterns for slightly misaligned identical lattices: graphene on graphite," *2D Mater.*, vol. 2, no. 3, p. 034010, 2015.

[34] S. Dai, Y. Xiang, and D. J. Srolovitz, "Twisted bilayer graphene: Moiré with a twist," *Nano Lett.*, vol. 16, no. 9, pp. 5923–5927, 2016.

[35] J. Jung, A. M. DaSilva, A. H. MacDonald, and S. Adam, "Origin of band gaps in graphene on hexagonal boron nitride," *Nat. Commun.*, vol. 6, p. 6308, 2015.

[36] S. K. Jain, V. Juričić, and G. T. Barkema, "Structure of twisted and buckled bilayer graphene," *2D Mater.*, vol. 4, no. 1, p. 015018, 2016.

[37] N. N. T. Nam and M. Koshino, "Lattice relaxation and energy band modulation in twisted bilayer graphene," *Phys. Rev. B*, vol. 96, no. 7, p. 075311, 2017, errata ibid **101**, 099901 (2020).

[38] S. Carr, D. Massatt, S. B. Torrisi, P. Cazeaux, M. Luskin, and E. Kaxiras, "Relaxation and domain formation in incommensurate two-dimensional heterostructures," *Phys. Rev. B*, vol. 98, p. 224102, Dec 2018. [Online]. Available: https://link.aps.org/doi/10.1103/PhysRevB.98.224102

[39] X. Lin, D. Liu, and D. Tománek, "Shear instability in twisted bilayer graphene," *Phys. Rev. B*, vol. 98, p. 195432, Nov 2018. [Online]. Available: https://link.aps.org/doi/10.1103/PhysRevB.98.195432

[40] H. Yoo, R. Engelke, S. Carr, S. Fang, K. Zhang, P. Cazeaux, S. H. Sung, R. Hovden, A. W. Tsen, T. Taniguchi, G.-C. Watanabe, Kenji Yi, M. Kim, L. Mitchell, E. B. Tadmor, E. Kaxiras, and P. Kim, "Atomic and electronic reconstruction at the van der waals interface in twisted bilayer graphene," *Nat. Mater.*, vol. 18, no. 5, p. 448, 2019.

[41] F. Guinea and N. R. Walet, "Continuum models for twisted bilayer graphene: Effect of lattice deformation and hopping parameters," *Phys. Rev. B*, vol. 99, no. 20, p. 205134, 2019.

[42] M. Koshino and N. N. Nam, "Effective continuum model for relaxed twisted bilayer graphene and moiré electron-phonon interaction," *Phys. Rev. B*, vol. 101, no. 19, p. 195425, 2020.

[43] L. P. A. Krisna and M. Koshino, "Moiré phonons in graphene/hexagonal boron nitride moiré superlattice," *Phys. Rev. B*, vol. 107, p. 115301, Mar 2023. [Online]. Available: https://link.aps.org/doi/10.1103/PhysRevB.107.115301

[44] F. Ferreira, S. Magorrian, V. Enaldiev, D. Ruiz-Tijerina, and V. Fal'ko, "Band energy landscapes in twisted homobilayers of transition metal dichalcogenides," *Applied Physics Letters*, vol. 118, no. 24, 2021.

[45] N. Mao, C. Xu, J. Li, T. Bao, P. Liu, Y. Xu, C. Felser, L. Fu, and Y. Zhang, "Lattice relaxation, electronic structure and continuum model for twisted bilayer mote $_2$," *arXiv preprint arXiv:2311.07533*, 2023.

[46] I. Soltero, M. A. Kaliteevski, J. G. McHugh, V. V. Enaldiev, and V. I. Fal'ko, "Competition of moir\'e network sites to form electronic quantum dots in reconstructed mox

{

}$_2$/wx

{

}$_2$ heterostructures," *arXiv preprint arXiv:2311.17710*, 2023.

[47] S. Shallcross, S. Sharma, and O. A. Pankratov, "Quantum interference at the twist boundary in graphene," *Phys. Rev. Lett.*, vol. 101, p. 056803, Aug 2008. [Online]. Available: https://link.aps.org/doi/10.1103/PhysRevLett.101.056803

[48] G. Trambly de Laissardière, D. Mayou, and L. Magaud, "Localization of dirac electrons in rotated graphene bilayers," *Nano letters*, vol. 10, no. 3, pp. 804–808, 2010.

[49] E. Suárez Morell, J. D. Correa, P. Vargas, M. Pacheco, and Z. Barticevic, "Flat bands in slightly twisted bilayer graphene: Tight-binding calculations," *Phys. Rev. B*, vol. 82, p. 121407, Sep 2010. [Online]. Available: https://link.aps.org/doi/10.1103/PhysRevB.82.121407

[50] L. Xian, S. Barraza-Lopez, and M. Y. Chou, "Effects of electrostatic fields and charge doping on the linear bands in twisted graphene bilayers," *Phys. Rev. B*, vol. 84, p. 075425, Aug 2011. [Online]. Available: https://link.aps.org/doi/10.1103/PhysRevB.84.075425

[51] G. Trambly de Laissardière, D. Mayou, and L. Magaud, "Numerical studies of confined states in rotated bilayers of graphene," *Phys. Rev. B*, vol. 86, p. 125413, Sep 2012. [Online]. Available: https://link.aps.org/doi/10.1103/PhysRevB.86.125413

[52] S. Latil, V. Meunier, and L. Henrard, "Massless fermions in multilayer graphitic systems with misoriented layers: Ab initio calculations and experimental fingerprints," *Phys. Rev. B*, vol. 76, p. 201402, Nov 2007. [Online]. Available: https://link.aps.org/doi/10.1103/PhysRevB.76.201402

[53] S. Shallcross, S. Sharma, E. Kandelaki, and O. A. Pankratov, "Electronic structure of turbostratic graphene," *Phys. Rev. B*, vol. 81, p. 165105, Apr 2010. [Online]. Available: https://link.aps.org/doi/10.1103/PhysRevB.81.165105

[54] J. M. B. Lopes dos Santos, N. M. R. Peres, and A. H. Castro Neto, "Graphene bilayer with a twist: Electronic structure," *Phys. Rev. Lett.*, vol. 99, p. 256802, Dec 2007. [Online]. Available: https://link.aps.org/doi/10.1103/PhysRevLett.99.256802

[55] E. J. Mele, "Commensuration and interlayer coherence in twisted bilayer graphene," *Phys. Rev. B*, vol. 81, p. 161405, Apr 2010. [Online]. Available: https://link.aps.org/doi/10.1103/PhysRevB.81.161405

[56] M. Koshino, "Interlayer interaction in general incommensurate atomic layers," *New J. Phys.*, vol. 17, no. 1, p. 015014, 2015. [Online]. Available: http://stacks.iop.org/1367-2630/17/i=1/a=015014

[57] M. Koshino, N. F. Q. Yuan, T. Koretsune, M. Ochi, K. Kuroki, and L. Fu, "Maximally localized wannier orbitals and the extended hubbard model for twisted bilayer graphene," *Phys. Rev. X*, vol. 8, p. 031087, Sep 2018. [Online]. Available: https://link.aps.org/doi/10.1103/PhysRevX.8.031087

[58] C. Mora, N. Regnault, and B. A. Bernevig, "Flatbands and perfect metal in trilayer moiré graphene," *Phys. Rev. Lett.*, vol. 123, p. 026402, Jul 2019. [Online]. Available: https://link.aps.org/doi/10.1103/PhysRevLett.123.026402

[59] X. Li, F. Wu, and A. H. MacDonald, "Electronic structure of single-twist trilayer graphene," 2019.

[60] S. Carr, C. Li, Z. Zhu, E. Kaxiras, S. Sachdev, and A. Kruchkov, "Ultra-heavy and ultrarelativistic dirac quasiparticles in sandwiched graphenes," *Nano letters*, vol. 20, no. 5, pp. 3030–3038, 2020.

[61] G. A. Tritsaris, S. Carr, Z. Zhu, Y. Xie, S. B. Torrisi, J. Tang, M. Mattheakis, D. T. Larson, and E. Kaxiras, "Electronic structure calculations of twisted multi-layer graphene superlattices," *2D Materials*, vol. 7, no. 3, p. 035028, 2020.

[62] A. Lopez-Bezanilla and J. L. Lado, "Electrical band flattening, valley flux, and superconductivity in twisted trilayer graphene," *Phys. Rev. Res.*, vol. 2, p. 033357, Sep 2020. [Online]. Available: https://link.aps.org/doi/10.1103/PhysRevResearch.2.033357

[63] A. Ramires and J. L. Lado, "Emulating heavy fermions in twisted trilayer graphene," *Phys. Rev. Lett.*, vol. 127, p. 026401, Jul 2021. [Online]. Available: https://link.aps.org/doi/10.1103/PhysRevLett.127.026401

[64] C. Lei, L. Linhart, W. Qin, F. Libisch, and A. H. MacDonald, "Mirror symmetry breaking and lateral stacking shifts in twisted trilayer graphene," *Phys. Rev. B*, vol. 104, p. 035139, Jul 2021. [Online]. Available: https://link.aps.org/doi/10.1103/PhysRevB.104.035139

[65] V. o. T. Phong, P. A. Pantaleón, T. Cea, and F. Guinea, "Band structure and superconductivity in twisted trilayer graphene," *Phys. Rev. B*, vol. 104, p. L121116, Sep 2021. [Online]. Available: https://link.aps.org/doi/10.1103/PhysRevB.104.L121116

[66] D. Călugăru, F. Xie, Z.-D. Song, B. Lian, N. Regnault, and B. A. Bernevig, "Twisted symmetric trilayer graphene: Single-particle and many-body hamiltonians and hidden nonlocal symmetries of trilayer moiré systems with and without displacement field," *Phys. Rev. B*, vol. 103, p. 195411, May 2021. [Online]. Available: https://link.aps.org/doi/10.1103/PhysRevB.103.195411

[67] F. Xie, N. Regnault, D. Călugăru, B. A. Bernevig, and B. Lian, "Twisted symmetric trilayer graphene. ii. projected hartree-fock study," *Phys. Rev. B*, vol. 104, p. 115167, Sep 2021. [Online]. Available: https://link.aps.org/doi/10.1103/PhysRevB.104.115167

[68] D. Guerci, P. Simon, and C. Mora, "Higher-order van hove singularity in magic-angle twisted trilayer graphene," *Phys. Rev. Res.*, vol. 4, p. L012013, Feb 2022. [Online]. Available: https://link.aps.org/doi/10.1103/PhysRevResearch.4.L012013

[69] M. Christos, S. Sachdev, and M. S. Scheurer, "Correlated insulators, semimetals, and superconductivity in twisted trilayer graphene," *Phys. Rev. X*, vol. 12, p. 021018, Apr 2022. [Online]. Available: https://link.aps.org/doi/10.1103/PhysRevX.12.021018

[70] Y. Zhang, R. Polski, C. Lewandowski, A. Thomson, Y. Peng, Y. Choi, H. Kim, K. Watanabe, T. Taniguchi, J. Alicea, F. von Oppen, G. Refael, and S. Nadj-Perge, "Promotion of superconductivity in magic-angle graphene multilayers," *Science*, vol. 377, no. 6614, pp. 1538–1543, 2022. [Online]. Available: https://www.science.org/doi/abs/10.1126/science.abn8585

[71] Z. Hao, A. M. Zimmerman, P. Ledwith, E. Khalaf, D. H. Najafabadi, K. Watanabe, T. Taniguchi, A. Vishwanath, and P. Kim, "Electric field–tunable superconductivity in alternating-twist magic-angle trilayer graphene," *Science*, vol. 371, no. 6534, pp. 1133–1138, 2021. [Online]. Available: https://www.science.org/doi/abs/10.1126/science.abg0399

[72] J. M. Park, Y. Cao, K. Watanabe, T. Taniguchi, and P. Jarillo-Herrero, "Tunable strongly coupled superconductivity in magic-angle twisted trilayer graphene," *Nature*, vol. 590, no. 7845, pp. 249–255, 2021.

[73] Y. Cao, J. M. Park, K. Watanabe, T. Taniguchi, and P. Jarillo-Herrero, "Pauli-limit violation and re-entrant superconductivity in moiré graphene," *Nature*, vol. 595, no. 7868, pp. 526–531, 2021.

[74] H. Kim, Y. Choi, C. Lewandowski, A. Thomson, Y. Zhang, R. Polski, K. Watanabe, T. Taniguchi, J. Alicea, and S. Nadj-Perge, "Evidence

for unconventional superconductivity in twisted trilayer graphene," *Nature*, vol. 606, no. 7914, pp. 494–500, Jun 2022. [Online]. Available: https://doi.org/10.1038/s41586-022-04715-z

[75] Q. Gao and E. Khalaf, "Symmetry origin of lattice vibration modes in twisted multilayer graphene: Phasons versus moiré phonons," *Physical Review B*, vol. 106, no. 7, p. 075420, 2022.

[76] Z. Ma, S. Li, M. Lu, D.-H. Xu, J.-H. Gao, and X. Xie, "Doubled moiré flat bands in double-twisted few-layer graphite," *Science China Physics, Mechanics & Astronomy*, vol. 66, no. 2, p. 227211, Dec 2022. [Online]. Available: https://doi.org/10.1007/s11433-022-1993-7

[77] M. Liang, M.-M. Xiao, Z. Ma, and J.-H. Gao, "Moiré band structures of the double twisted few-layer graphene," *Phys. Rev. B*, vol. 105, p. 195422, May 2022. [Online]. Available: https://link.aps.org/doi/10.1103/PhysRevB.105.195422

[78] Y. Mao, D. Guerci, and C. Mora, "Supermoiré low-energy effective theory of twisted trilayer graphene," *Phys. Rev. B*, vol. 107, p. 125423, Mar 2023. [Online]. Available: https://link.aps.org/doi/10.1103/PhysRevB.107.125423

[79] F. K. Popov and G. Tarnopolsky, "Magic angles in equal-twist trilayer graphene," 2023.

[80] X. Lin, C. Li, K. Su, and J. Ni, "Energetic stability and spatial inhomogeneity in the local electronic structure of relaxed twisted trilayer graphene," *Phys. Rev. B*, vol. 106, p. 075423, Aug 2022. [Online]. Available: https://link.aps.org/doi/10.1103/PhysRevB.106.075423

[81] H. Meng, Z. Zhan, and S. Yuan, "Commensurate and incommensurate double moiré interference in twisted trilayer graphene," *Phys. Rev. B*, vol. 107, no. 3, p. 035109, 2023.

[82] A. Dunbrack and J. Cano, "Intrinsically multilayer moiré heterostructures," *Phys. Rev. B*, vol. 107, p. 235425, Jun 2023.

[83] H. Oka and M. Koshino, "Fractal energy gaps and topological invariants in hbn/graphene/hbn double moiré systems," *Physical Review B*, vol. 104, no. 3, p. 035306, 2021.

[84] M. Koshino and H. Oka, "Topological invariants in two-dimensional quasicrystals," *Physical Review Research*, vol. 4, no. 1, p. 013028, 2022.

[85] N. R. Finney, M. Yankowitz, L. Muraleetharan, K. Watanabe, T. Taniguchi, C. R. Dean, and J. Hone, "Tunable crystal symmetry in graphene–boron nitride heterostructures with coexisting moiré superlattices," *Nature nanotechnology*, vol. 14, no. 11, pp. 1029–1034, 2019.

[86] L. Wang, S. Zihlmann, M.-H. Liu, P. Makk, K. Watanabe, T. Taniguchi, A. Baumgartner, and C. Schönenberger, "New generation of moiré superlattices in doubly aligned hbn/graphene/hbn heterostructures," *Nano letters*, vol. 19, no. 4, pp. 2371–2376, 2019.

[87] Z. Wang, Y. B. Wang, J. Yin, E. Tóvári, Y. Yang, L. Lin, M. Holwill, J. Birkbeck, D. Perello, S. Xu *et al.*, "Composite super-moiré lattices in double-aligned graphene heterostructures," *Science advances*, vol. 5, no. 12, p. eaay8897, 2019.

[88] Y. Yang, J. Li, J. Yin, S. Xu, C. Mullan, T. Taniguchi, K. Watanabe, A. K. Geim, K. S. Novoselov, and A. Mishchenko, "In situ twistronics of van der waals heterostructures," *arXiv preprint arXiv:2010.03798*, 2020.

[89] M. Andelkovic, S. P. Milovanovic, L. Covaci, and F. M. Peeters, "Double moiré with a twist: Supermoiré in encapsulated graphene," *Nano letters*, vol. 20, no. 2, pp. 979–988, 2020.

[90] N. Leconte and J. Jung, "Commensurate and incommensurate double moire interference in graphene encapsulated by hexagonal boron nitride," *2D Materials*, vol. 7, no. 3, p. 031005, 2020.

[91] M. Onodera, K. Kinoshita, R. Moriya, S. Masubuchi, K. Watanabe, T. Taniguchi, and T. Machida, "Cyclotron resonance study of monolayer graphene under double moiré potentials," *Nano letters*, vol. 20, no. 6, pp. 4566–4572, 2020.

[92] M. Kuiri, S. K. Srivastav, S. Ray, K. Watanabe, T. Taniguchi, T. Das, and A. Das, "Enhanced electron-phonon coupling in doubly aligned hexagonal boron nitride bilayer graphene heterostructure," *Physical Review B*, vol. 103, no. 11, p. 115419, 2021.

[93] J. Shi, J. Zhu, and A. MacDonald, "Moiré commensurability and the quantum anomalous hall effect in twisted bilayer graphene on hexagonal boron nitride," *Physical Review B*, vol. 103, no. 7, p. 075122, 2021.

[94] J. Shin, Y. Park, B. L. Chittari, J.-H. Sun, and J. Jung, "Electron-hole asymmetry and band gaps of commensurate double moire patterns in twisted bilayer graphene on hexagonal boron nitride," *Physical Review B*, vol. 103, no. 7, p. 075423, 2021.

[95] J. Shin, B. L. Chittari, and J. Jung, "Stacking and gate-tunable topological flat bands, gaps, and anisotropic strip patterns in twisted trilayer graphene," *Physical Review B*, vol. 104, no. 4, p. 045413, 2021.

[96] X. Huang, L. Chen, S. Tang, C. Jiang, C. Chen, H. Wang, Z.-X. Shen, H. Wang, and Y.-T. Cui, "Moir\'e imaging in twisted bilayer graphene aligned on hexagonal boron nitride," *arXiv preprint arXiv:2102.08594*, 2021.

[97] I. V. Lebedeva, A. A. Knizhnik, A. M. Popov, Y. E. Lozovik, and B. V. Potapkin, "Interlayer interaction and relative vibrations of bilayer graphene," *Physical Chemistry Chemical Physics*, vol. 13, no. 13, pp. 5687–5695, 2011.

[98] T. Gould, S. Lebègue, and J. F. Dobson, "Dispersion corrections in graphenic systems: a simple and effective model of binding," *Journal of Physics: Condensed Matter*, vol. 25, no. 44, p. 445010, 2013.

[99] F. Guinea and N. R. Walet, "Continuum models for twisted bilayer graphene: Effect of lattice deformation and hopping parameters," *Phys. Rev. B*, vol. 99, p. 205134, May 2019. [Online]. Available: https://link.aps.org/doi/10.1103/PhysRevB.99.205134

[100] P. Lucignano, D. Alfè, V. Cataudella, D. Ninno, and G. Cantele, "Crucial role of atomic corrugation on the flat bands and energy gaps of twisted bilayer graphene at the magic angle $\theta \sim 1.08°$," *Phys. Rev. B*, vol. 99, p. 195419, May 2019. [Online]. Available: https://link.aps.org/doi/10.1103/PhysRevB.99.195419

[101] S. Carr, S. Fang, Z. Zhu, and E. Kaxiras, "Exact continuum model for low-energy electronic states of twisted bilayer graphene," *Phys. Rev. Research*, vol. 1, no. 1, p. 013001, 2019.

[102] N. Nakatsuji and M. Koshino, "Moiré disorder effect in twisted bilayer graphene," *Phys. Rev. B*, vol. 105, p. 245408, Jun 2022. [Online]. Available: https://link.aps.org/doi/10.1103/PhysRevB.105.245408

[103] H. Suzuura and T. Ando, "Phonons and electron-phonon scattering in carbon nanotubes," *Phys. Rev. B*, vol. 65, p. 235412, May 2002. [Online]. Available: https://link.aps.org/doi/10.1103/PhysRevB.65.235412

[104] V. M. Pereira and A. H. Castro Neto, "Strain engineering of graphene's electronic structure," *Phys. Rev. Lett.*, vol. 103, p. 046801, Jul 2009. [Online]. Available: https://link.aps.org/doi/10.1103/PhysRevLett.103.046801

[105] F. Guinea, M. I. Katsnelson, and A. K. Geim, "Energy gaps and a zero-field quantum hall effect in graphene by strain engineering," *Nature Physics*, vol. 6, no. 1, pp. 30–33, 2010. [Online]. Available: https://doi.org/10.1038/nphys1420

[106] J. A. Crosse, N. Nakatsuji, M. Koshino, and P. Moon, "Hofstadter butterfly and the quantum hall effect in twisted double bilayer graphene," *Phys. Rev. B*, vol. 102, p. 035421, Jul 2020. [Online]. Available: https://link.aps.org/doi/10.1103/PhysRevB.102.035421

[107] G. Li, A. Luican, J. M. B. Lopes dos Santos, A. H. Castro Neto, A. Reina, J. Kong, and E. Y. Andrei, "Observation of van hove singularities in twisted graphene layers," *Nat. Phys.*, vol. 6, no. 2, pp. 109–113, 2010.

[108] A. Luican, G. Li, A. Reina, J. Kong, R. R. Nair, K. S. Novoselov, A. K. Geim, and E. Y. Andrei, "Single-layer behavior and its breakdown in twisted graphene layers," *Phys. Rev. Lett.*, vol. 106, p. 126802, Mar 2011. [Online]. Available: https://link.aps.org/doi/10.1103/PhysRevLett.106.126802

[109] I. Brihuega, P. Mallet, H. González-Herrero, G. Trambly de Laissardière, M. M. Ugeda, L. Magaud, J. M. Gómez-Rodr´iguez, F. Ynduráin, and J.-Y. Veuillen, "Unraveling the intrinsic and robust nature of van hove singularities in twisted bilayer graphene by scanning tunneling microscopy and theoretical analysis," *Phys. Rev. Lett.*, vol. 109, p. 196802, Nov 2012. [Online]. Available: https://link.aps.org/doi/10.1103/PhysRevLett.109.196802

[110] D. Wong, Y. Wang, J. Jung, S. Pezzini, A. M. DaSilva, H.-Z. Tsai, H. S. Jung, R. Khajeh, Y. Kim, J. Lee, S. Kahn, S. Tollabimazraehno, H. Rasool, K. Watanabe, T. Taniguchi, A. Zettl, S. Adam, A. H. MacDonald, and M. F. Crommie, "Local spectroscopy of moiré-induced electronic structure in gate-tunable twisted bilayer graphene," *Phys. Rev. B*, vol. 92, p. 155409, Oct 2015. [Online]. Available: https://link.aps.org/doi/10.1103/PhysRevB.92.155409

[111] J.-B. Qiao, L.-J. Yin, and L. He, "Twisted graphene bilayer around the first magic angle engineered by heterostrain," *Phys. Rev. B*, vol. 98, p. 235402, Dec 2018. [Online]. Available: https://link.aps.org/doi/10.1103/PhysRevB.98.235402

[112] H. Shi, Z. Zhan, Z. Qi, K. Huang, E. v. Veen, J. Á. Silva-Guillén, R. Zhang, P. Li, K. Xie, H. Ji, M. I. Katsnelson, S. Yuan, S. Qin, and Z. Zhang, "Large-area, periodic, and tunable intrinsic pseudo-magnetic fields in low-angle twisted bilayer graphene," *Nature Communications*, vol. 11, no. 1, p. 371, 2020. [Online]. Available: https://doi.org/10.1038/s41467-019-14207-w

[113] A. Uri, S. Grover, Y. Cao, J. A. Crosse, K. Bagani, D. Rodan-Legrain, Y. Myasoedov, K. Watanabe, T. Taniguchi, P. Moon, M. Koshino, P. Jarillo-Herrero, and E. Zeldov, "Mapping the twist-angle disorder and landau levels in magic-angle graphene," *Nature*, vol. 581, no. 7806, pp. 47–52, 2020. [Online]. Available: https://doi.org/10.1038/s41586-020-2255-3

[114] L. J. McGilly, A. Kerelsky, N. R. Finney, K. Shapovalov, E.-M. Shih, A. Ghiotto, Y. Zeng, S. L. Moore, W. Wu, Y. Bai, K. Watanabe, T. Taniguchi, M. Stengel, L. Zhou, J. Hone, X. Zhu, D. N. Basov, C. Dean, C. E. Dreyer, and A. N. Pasupathy, "Visualization of moirésuperlattices," *Nature Nanotechnology*, vol. 15, no. 7, pp. 580–584, 2020. [Online]. Available: https://doi.org/10.1038/s41565-020-0708-3

[115] A. C. Gadelha, D. A. Ohlberg, C. Rabelo, E. G. Neto, T. L. Vasconcelos, J. L. Campos, J. S. Lemos, V. Ornelas, D. Miranda, R. Nadas *et al.*, "Localization of lattice dynamics in low-angle twisted bilayer graphene," *Nature*, vol. 590, no. 7846, pp. 405–409, 2021.

[116] N. P. Kazmierczak, M. Van Winkle, C. Ophus, K. C. Bustillo, S. Carr, H. G. Brown, J. Ciston, T. Taniguchi, K. Watanabe, and D. K. Bediako, "Strain fields in twisted bilayer graphene," *Nature materials*, vol. 20, no. 7, pp. 956–963, 2021.

[117] N. Tilak, X. Lai, S. Wu, Z. Zhang, M. Xu, R. d. A. Ribeiro, P. C. Canfield, and E. Y. Andrei, "Flat band carrier confinement in magic-angle twisted bilayer graphene," *Nature communications*, vol. 12, no. 1, pp. 1–7, 2021.

[118] F. Mesple, A. Missaoui, T. Cea, L. Huder, F. Guinea, G. Trambly de Laissardière, C. Chapelier, and V. T. Renard, "Heterostrain determines flat bands in magic-angle twisted graphene layers," *Phys. Rev. Lett.*, vol. 127, p. 126405, Sep 2021. [Online]. Available: https://link.aps.org/doi/10.1103/PhysRevLett.127.126405

[119] A. Schäpers, J. Sonntag, L. Valerius, B. Pestka, J. Strasdas, K. Watanabe, T. Taniguchi, M. Morgenstern, B. Beschoten, R. Dolleman *et al.*, "Raman imaging of twist angle variations in twisted bilayer graphene at intermediate angles," *arXiv:2104.06370*, 2021.

[120] J. H. Wilson, Y. Fu, S. Das Sarma, and J. H. Pixley, "Disorder in twisted bilayer graphene," *Phys. Rev. Research*, vol. 2, p. 023325, Jun 2020. [Online]. Available: https://link.aps.org/doi/10.1103/PhysRevResearch.2.023325

[121] B. Padhi, A. Tiwari, T. Neupert, and S. Ryu, "Transport across twist angle domains in moiré graphene," *Phys. Rev. Research*, vol. 2, p. 033458, Sep 2020. [Online]. Available: https://link.aps.org/doi/10.1103/PhysRevResearch.2.033458

[122] S. Joy, S. Khalid, and B. Skinner, "Transparent mirror effect in twist-angle-disordered bilayer graphene," *Physical Review Research*, vol. 2, no. 4, p. 043416, 2020.

[123] H. Sainz-Cruz, T. Cea, P. A. Pantaleón, and F. Guinea, "High transmission in twisted bilayer graphene with angle disorder," *Phys. Rev. B*, vol. 104, p. 075144, Aug 2021. [Online]. Available: https://link.aps.org/doi/10.1103/PhysRevB.104.075144

[124] A. Thomson and J. Alicea, "Recovery of massless dirac fermions at charge neutrality in strongly interacting twisted bilayer graphene with disorder," *Phys. Rev. B*, vol. 103, p. 125138, Mar 2021. [Online]. Available: https://link.aps.org/doi/10.1103/PhysRevB.103.125138

[125] P. Moon and M. Koshino, "Optical absorption in twisted bilayer graphene," *Phys. Rev. B*, vol. 87, p. 205404, May 2013.

[126] P. San-Jose, A. Gutiérrez-Rubio, M. Sturla, and F. Guinea, "Electronic structure of spontaneously strained graphene on hexagonal boron nitride," *Phys. Rev. B*, vol. 90, p. 115152, Sep 2014. [Online]. Available: https://link.aps.org/doi/10.1103/PhysRevB.90.115152

[127] K. V. Zakharchenko, M. I. Katsnelson, and A. Fasolino, "Finite temperature lattice properties of graphene beyond the quasiharmonic approximation," *Phys. Rev. Lett.*, vol. 102, p. 046808, Jan 2009. [Online]. Available: https://link.aps.org/doi/10.1103/PhysRevLett.102.046808

[128] J. C. Slater and G. F. Koster, "Simplified lcao method for the periodic potential problem," *Phys. Rev.*, vol. 94, pp. 1498–1524, Jun 1954. [Online]. Available: https://link.aps.org/doi/10.1103/PhysRev.94.1498

[129] M. Koshino and Y.-W. Son, "Moiré phonons in twisted bilayer graphene," *Phys. Rev. B*, vol. 100, p. 075416, Aug 2019. [Online]. Available: https://link.aps.org/doi/10.1103/PhysRevB.100.075416

[130] J. Lopes dos Santos, N. Peres, and A. Castro Neto, "Graphene bilayer with a twist: Electronic structure," *Phys. Rev. Lett.*, vol. 99, no. 25, p. 256802, 2007.

[131] M. Kindermann and P. First, "Local sublattice-symmetry breaking in rotationally faulted multilayer graphene," *Phys. Rev. B*, vol. 83, no. 4, p. 045425, 2011.

[132] J. M. B. Lopes dos Santos, N. M. R. Peres, and A. H. Castro Neto, "Continuum model of the twisted graphene bilayer," *Phys. Rev. B*, vol. 86, p. 155449, Oct 2012.

[133] P. San-Jose and E. Prada, "Helical networks in twisted bilayer graphene under interlayer bias," *Phys. Rev. B*, vol. 88, p. 121408, Sep 2013. [Online]. Available: https://link.aps.org/doi/10.1103/PhysRevB.88.121408

[134] A. Ramires and J. L. Lado, "Electrically tunable gauge fields in tiny-angle twisted bilayer graphene," *Phys. Rev. Lett.*, vol. 121, p. 146801, Oct 2018. [Online]. Available: https://link.aps.org/doi/10.1103/PhysRevLett.121.146801

[135] D. K. Efimkin and A. H. MacDonald, "Helical network model for twisted bilayer graphene," *Phys. Rev. B*, vol. 98, p. 035404, Jul 2018. [Online]. Available: https://link.aps.org/doi/10.1103/PhysRevB.98.035404

[136] M. Fleischmann, R. Gupta, F. Wullschläger, S. Theil, D. Weckbecker, V. Meded, S. Sharma, B. Meyer, and S. Shallcross, "Perfect and controllable nesting in minimally twisted bilayer graphene," *Nano Lett.*, vol. 20, no. 2, p. 971, 2020.

[137] N. R. Walet and F. Guinea, "The emergence of one-dimensional channels in marginal-angle twisted bilayer graphene," *2D Materials*, vol. 7, no. 1, p. 015023, 2019.

[138] B. Tsim, N. N. T. Nam, and M. Koshino, "Perfect one-dimensional chiral states in biased twisted bilayer graphene," *Phys. Rev. B*, vol. 101, p. 125409, Mar 2020. [Online]. Available: https://link.aps.org/doi/10.1103/PhysRevB.101.125409

[139] T. Hou, Y. Ren, Y. Quan, J. Jung, W. Ren, and Z. Qiao, "Metallic network of topological domain walls," *Phys. Rev. B*, vol. 101, p. 201403, May 2020. [Online]. Available: https://link.aps.org/doi/10.1103/PhysRevB.101.201403

[140] F. Guinea and N. R. Walet, "Electrostatic effects, band distortions, and superconductivity in twisted graphene bilayers," *Proceedings of the National Academy of Sciences*, vol. 115, no. 52, pp. 13 174–13 179, 2018. [Online]. Available: https://www.pnas.org/doi/abs/10.1073/pnas.1810947115

[141] J. Kang and O. Vafek, "Symmetry, maximally localized wannier states, and a low-energy model for twisted bilayer graphene narrow bands," *Phys. Rev. X*, vol. 8, no. 3, p. 031088, 2018.

[142] H. C. Po, L. Zou, A. Vishwanath, and T. Senthil, "Origin of mott insulating behavior and superconductivity in twisted bilayer graphene," *Phys. Rev. X*, vol. 8, p. 031089, Sep 2018. [Online]. Available: https://link.aps.org/doi/10.1103/PhysRevX.8.031089

[143] Z. Bi, N. F. Q. Yuan, and L. Fu, "Designing flat bands by strain," *Phys. Rev. B*, vol. 100, p. 035448, Jul 2019. [Online]. Available: https://link.aps.org/doi/10.1103/PhysRevB.100.035448

[144] N. Bultinck, E. Khalaf, S. Liu, S. Chatterjee, A. Vishwanath, and M. P. Zaletel, "Ground state and hidden symmetry of magic-angle graphene at even integer filling," *Phys. Rev. X*, vol. 10, p. 031034, Aug 2020. [Online]. Available: https://link.aps.org/doi/10.1103/PhysRevX.10.031034

[145] M. Xie and A. H. MacDonald, "Nature of the correlated insulator states in twisted bilayer graphene," *Phys. Rev. Lett.*, vol. 124, p. 097601, Mar 2020. [Online]. Available: https://link.aps.org/doi/10.1103/PhysRevLett.124.097601

[146] Y. Zhang, K. Jiang, Z. Wang, and F. Zhang, "Correlated insulating phases of twisted bilayer graphene at commensurate filling fractions: A hartree-fock study," *Phys. Rev. B*, vol. 102, p. 035136, Jul 2020. [Online]. Available: https://link.aps.org/doi/10.1103/PhysRevB.102.035136

[147] J. Liu and X. Dai, "Theories for the correlated insulating states and quantum anomalous hall effect phenomena in twisted bilayer graphene," *Phys. Rev. B*, vol. 103, p. 035427, Jan 2021. [Online]. Available: https://link.aps.org/doi/10.1103/PhysRevB.103.035427

[148] M. Manna"i and S. Haddad, "Twistronics versus straintronics in twisted bilayers of graphene and transition metal dichalcogenides," *Physical Review B*, vol. 103, no. 20, p. L201112, 2021.

[149] Z.-B. Dai, Y. He, and Z. Li, "Effects of heterostrain and lattice relaxation on the optical conductivity of twisted bilayer graphene," *Phys. Rev. B*, vol. 104, p. 045403, Jul 2021. [Online]. Available: https://link.aps.org/doi/10.1103/PhysRevB.104.045403

[150] D. Kaplan, T. Holder, and B. Yan, "Twisted photovoltaics at terahertz frequencies from momentum shift current," *Phys. Rev. Research*, vol. 4, p. 013209, Mar 2022. [Online]. Available: https://link.aps.org/doi/10.1103/PhysRevResearch.4.013209

[151] W.-Y. He, D. Goldhaber-Gordon, and K. T. Law, "Giant orbital magnetoelectric effect and current-induced magnetization switching in twisted bilayer graphene," *Nature communications*, vol. 11, no. 1, pp. 1–8, 2020.

[152] J. Liu, J. Liu, and X. Dai, "Pseudo landau level representation of twisted bilayer graphene: Band topology and implications on the correlated insulating phase," *Phys. Rev. B*, vol. 99, p. 155415, Apr 2019. [Online]. Available: https://link.aps.org/doi/10.1103/PhysRevB.99.155415

[153] L. Huder, A. Artaud, T. Le Quang, G. T. de Laissardière, A. G. M. Jansen, G. Lapertot, C. Chapelier, and V. T. Renard, "Electronic spectrum of twisted graphene layers under heterostrain," *Phys. Rev. Lett.*, vol. 120, p. 156405, Apr 2018. [Online]. Available: https://link.aps.org/doi/10.1103/PhysRevLett.120.156405

[154] H. Ochoa, "Strain-induced excitonic instability in twisted bilayer graphene," *Phys. Rev. B*, vol. 102, p. 201107, Nov 2020. [Online]. Available: https://link.aps.org/doi/10.1103/PhysRevB.102.201107

[155] D. E. Parker, T. Soejima, J. Hauschild, M. P. Zaletel, and N. Bultinck, "Strain-induced quantum phase transitions in magic-angle graphene," *Phys. Rev. Lett.*, vol. 127, p. 027601, Jul 2021. [Online]. Available: https://link.aps.org/doi/10.1103/PhysRevLett.127.027601

[156] S. Carr, S. Fang, and E. Kaxiras, "Electronic-structure methods for twisted moiré layers," *Nature Reviews Materials*, vol. 5, no. 10, pp. 748–763, 2020.

[157] S. Liu, E. Khalaf, J. Y. Lee, and A. Vishwanath, "Nematic topological semimetal and insulator in magic-angle bilayer graphene at charge neutrality," *Phys. Rev. Research*, vol. 3, p. 013033, Jan 2021. [Online]. Available: https://link.aps.org/doi/10.1103/PhysRevResearch.3.013033

[158] L. Rademaker and P. Mellado, "Charge-transfer insulation in twisted bilayer graphene," *Phys. Rev. B*, vol. 98, p. 235158, Dec 2018. [Online]. Available: https://link.aps.org/doi/10.1103/PhysRevB.98.235158

[159] S. Carr, S. Fang, H. C. Po, A. Vishwanath, and E. Kaxiras, "Derivation of wannier orbitals and minimal-basis tight-binding hamiltonians for twisted bilayer graphene: First-principles approach," *Phys. Rev. Research*, vol. 1, p. 033072, Nov 2019. [Online]. Available: https://link.aps.org/doi/10.1103/PhysRevResearch.1.033072

[160] M. J. Calderón and E. Bascones, "Interactions in the 8-orbital model for twisted bilayer graphene," *Phys. Rev. B*, vol. 102, p. 155149, Oct 2020. [Online]. Available: https://link.aps.org/doi/10.1103/PhysRevB.102.155149

[161] V.-H. Nguyen, D. Paszko, M. Lamparski, B. V. Troeye, V. Meunier, and J.-C. Charlier, "Electronic localization in small-angle twisted bilayer graphene," *2D Materials*, may 2021. [Online]. Available: https://doi.org/10.1088/2053-1583/ac044f

[162] I. Yudhistira, N. Chakraborty, G. Sharma, D. Y. H. Ho, E. Laksono, O. P. Sushkov, G. Vignale, and S. Adam, "Gauge-phonon dominated resistivity in twisted bilayer graphene near magic angle," *Phys. Rev. B*, vol. 99, p. 140302, Apr 2019. [Online]. Available: https://link.aps.org/doi/10.1103/PhysRevB.99.140302

[163] E. Khalaf, A. J. Kruchkov, G. Tarnopolsky, and A. Vishwanath, "Magic angle hierarchy in twisted graphene multilayers," *Phys. Rev. B*, vol. 100, p. 085109, Aug 2019. [Online]. Available: https://link.aps.org/doi/10.1103/PhysRevB.100.085109

[164] W. Qin and A. H. MacDonald, "In-plane critical magnetic fields in magic-angle twisted trilayer graphene," *Phys. Rev. Lett.*, vol. 127, p. 097001, Aug 2021. [Online]. Available: https://link.aps.org/doi/10.1103/PhysRevLett.127.097001

[165] A. Fischer, Z. A. Goodwin, A. A. Mostofi, J. Lischner, D. M. Kennes, and L. Klebl, "Unconventional superconductivity in magic-angle twisted trilayer graphene," *npj Quantum Materials*, vol. 7, no. 1, pp. 1–10, 2022.

[166] M. Koshino, "Band structure and topological properties of twisted double bilayer graphene," *Phys. Rev. B*, vol. 99, p. 235406, Jun 2019. [Online]. Available: https://link.aps.org/doi/10.1103/PhysRevB.99.235406

[167] N. R. Chebrolu, B. L. Chittari, and J. Jung, "Flat bands in twisted double bilayer graphene," *Phys. Rev. B*, vol. 99, p. 235417, Jun 2019. [Online]. Available: https://link.aps.org/doi/10.1103/PhysRevB.99.235417

[168] J. Liu, Z. Ma, J. Gao, and X. Dai, "Quantum valley hall effect, orbital magnetism, and anomalous hall effect in twisted multilayer graphene systems," *Phys. Rev. X*, vol. 9, p. 031021, Aug 2019. [Online]. Available: https://link.aps.org/doi/10.1103/PhysRevX.9.031021

[169] P. Rickhaus, G. Zheng, J. L. Lado, Y. Lee, A. Kurzmann, M. Eich, R. Pisoni, C. Tong, R. Garreis, C. Gold *et al.*, "Gap opening in twisted double bilayer graphene by crystal fields," *Nano letters*, vol. 19, no. 12, pp. 8821–8828, 2019.

[170] G. W. Burg, J. Zhu, T. Taniguchi, K. Watanabe, A. H. MacDonald, and E. Tutuc, "Correlated insulating states in twisted double bilayer graphene," *Phys. Rev. Lett.*, vol. 123, p. 197702, Nov 2019. [Online]. Available: https://link.aps.org/doi/10.1103/PhysRevLett.123.197702

[171] J. Y. Lee, E. Khalaf, S. Liu, X. Liu, Z. Hao, P. Kim, and A. Vishwanath, "Theory of correlated insulating behaviour and spin-triplet superconductivity in twisted double bilayer graphene," *Nature communications*, vol. 10, no. 1, pp. 1–10, 2019.

List of publication

- Paper I

Hofstadter butterfly and the quantum Hall effect in twisted double bilayer graphene

J. A. Crosse, Naoto Nakatsuji, Mikito Koshino, and Pilkyung Moon

Physical Review B **102**, 035421 (2020)

- Paper II

Moiré disorder effect in twisted bilayer graphene

Naoto Nakatsuji, and Mikito Koshino

Physical Review B **105**, 245408 (2022)

- Paper III

Multiscale Lattice Relaxation in General Twisted Trilayer Graphenes

Naoto Nakatsuji, Takuto Kawakami, and Mikito Koshino

Physical Review X **13**, 041007 (2023)

Acknowledgments